Pre-Proceedings of the 2023 Symposium on Information Theory and Signal Processing in the Benelux

Université libre de Bruxelles
Campus du Solbosch, Brussels, Belgium
May 11-12th, 2023

Previous symposia

1.	1980 Zoetermeer, The Netherlands, Delft University of Technology	
2.	1981 Zoetermeer, The Netherlands, Delft University of Technology	
3.	1982 Zoetermeer, The Netherlands, Delft University of Technology	
4.	1983 Haasrode, Belgium	ISBN 90-334-0690-X
5.	1984 Aalten, The Netherlands	ISBN 90-71048-01-2
6.	1985 Mierlo, The Netherlands	ISBN 90-71048-02-0
7.	1986 Noordwijkerhout, The Netherlands	ISBN 90-6275-272-1
8.	1987 Deventer, The Netherlands	ISBN 90-71048-03-9
9.	1988 Mierlo, The Netherlands	ISBN 90-71048-04-7
10.	1989 Houthalen, Belgium	ISBN 90-71048-05-5
11.	1990 Noordwijkerhout, The Netherlands	ISBN 90-71048-06-3
12.	1991 Veldhoven, The Netherlands	ISBN 90-71048-07-1
13.	1992 Enschede, The Netherlands	ISBN 90-71048-08-X
14.	1993 Veldhoven, The Netherlands	ISBN 90-71048-09-8
15.	1994 Louvain-la-Neuve, Belgium	ISBN 90-71048-10-1
16.	1995 Nieuwekerk a/d IJssel, The Netherlands	ISBN 90-71048-11-X
17.	1996 Enschede, The Netherlands	ISBN 90-365-0812-6
18.	1997 Veldhoven, The Netherlands	ISBN 90-71048-12-8
19.	1998 Veldhoven, The Netherlands	ISBN 90-71048-13-6
20.	1999 Haasrode, Belgium	ISBN 90-71048-14-4
21.	2000 Wassenaar, The Netherlands	ISBN 90-71048-15-2
22.	2001 Enschede, The Netherlands	ISBN 90-365-1598-X
23.	2002 Louvain-la-Neuve, Belgium	ISBN 90-71048-16-0
24.	2003 Veldhoven, The Netherlands	ISBN 90-71048-18-7
25.	2004 Kerkrade, The Netherlands	ISBN 90-71048-20-9
26.	2005 Brussels, Belgium	ISBN 90-71048-21-7
27.	2006 Noordwijk, The Netherlands	ISBN 90-71048-22-7
28.	2007 Enschede, The Netherlands	ISBN 978-90-365-2509-1
29.	2008 Leuven, Belgium	ISBN 978-90-9023135-8
30.	2009 Eindhoven, The Netherlands	ISBN 978-90-386-1852-4
31.	2010 Rotterdam, The Netherlands	ISBN 978-90-710-4823-4
32.	2011 Brussels, Belgium	ISBN 978-90-817-2190-5
33.	2012 Enschede, The Netherlands	ISBN 978-90-365-3383-6
34.	2013 Leuven, Belgium	ISBN 978-90-365-0000-5
35.	2014 Eindhoven, The Netherlands	ISBN 978-90-386-3646-7
36.	2015 Brussels, Belgium	ISBN 978-2-8052-0277-3
37.	2016 Louvain-la-Neuve, Belgium	ISBN 978-2-9601884-0-0
38.	2017 Delft, The Netherlands	ISBN 978-94-6186-811-4
39.	2018 Enschede, The Netherlands	ISBN 978-90-365-4570-9
40.	2019 Ghent, Belgium	ISBN 978-94-918-5703-4
41.	2021 Eindhoven (online), The Netherlands	ISBN
42.	2022 Louvain-la-Neuve, Belgium	ISBN

The 43rd Symposium on Information Theory in the Benelux has been organized by

Université libre de Bruxelles and Delft University of Technology

https://sitb2023.ulb.be/

on behalf of the

Werkgemeenschap voor Informatie- en Communicatietheorie (WIC),
and the IEEE Benelux Signal Processing Chapter.

Financial support from the IEEE Benelux Signal Processing Chapter, the IEEE Benelux Information Theory Chapter and the Werkgemeenschap voor Informatie- en Communicatietheorie (WIC) is gratefully acknowledged.

Organizing committee:
François Quitin (Université libre de Bruxelles)
Qing Wang (Delft University of Technology)

Proceedings

Proceedings of the 43rd Symposium on Information Theory and Signal Processing in the Benelux. Edited by François Quitin and Qing Wang
ISBN: Pending.

Table of contents

Environment Mapping with 28 GHz Beam Steering Transceivers Using the SAGE Algorithm: Preliminary Results

Nigus Yirga
Brussels School of Engineering
Université Libre de Bruxelles
Brussels, Belgium
nigus.shimuye@ulb.be

Claude Oestges
ICTEAM
Université catholique de Louvain
Louvain, Belgium
claude.oestges@uclouvain.be

François Quitin
Brussels School of Engineering
Université Libre de Bruxelles
Brussels, Belgium
francois.quitin@ulb.be

***Abstract*—This paper presents a multipath component (MPC) parameter estimator for indoor environment mapping that uses the 28 GHz radio band. It employs a commercial-off-the-shelf (COTS) radio frequency transceiver chipset capable of beam steering within an azimuth angle range of -78^o and $+78^o$ but with only a single RF chain. Existing space-alternating generalized expectation-maximization (SAGE) algorithms for MPC parameter estimation are designed specifically for multi-antenna systems, with each antenna having its own baseband representation. By exploiting the beam steering characteristics, we adapted the SAGE algorithm to make it suitable for analyzing a single-baseband based multi-antenna array system. The anechoic chamber measured array radiation pattern for each steering direction is used in our algorithm to determine the MPC contribution. In an office setting, the transmitter and receiver antenna beams are swept. All backscatter responses are collected for all possible pairs of transmitter/receiver steering angles, and an angular map that contains the power profile is produced. The performance of the proposed algorithm is validated by simulation and measurement data.**

***Index Terms*—Environment mapping, MPC, baseband, SAGE, beam steering, multi-antenna array.**

I. Introduction

The emergence of millimeter-wave (mmWave) technology has enabled a range of new applications in wireless communications, such as gigabit-per-second data rates and ultra-low-latency links. However, the potential of mmWave is not limited to just communication applications. Due to their distinctive characteristics, such as high directionality, large bandwidths, and inability to penetrate obstacles, mmWave signals also provide interesting possibilities for sensing [1]. The high attenuation of the mmWave signal can be compensated using beamforming. Beam steering, which uses a phased antenna array to focus and direct a beam in a specific direction, has recently gained popularity because it adds scanning capability to mmWave-based sensing applications [2].

This has led to increasing interest in the use of mmWave for integrated sensing and communication (ISAC) purposes. ISAC is a new research area that aims to utilize the same transmit waveforms and processing modules for both wireless communication and radar sensing within a single system [3] [4]. The primary difference between using a mmWave system and a radar system for sensing is that a radar system has multiple radio-frequency (RF) chains and analog-to-digital converters (ADCs), which enables signal processing in the digital baseband domain, and it sends predefined waveforms. The wideband and narrow beam waveforms existing in mmWave-based ISACs turned to high-resolution sensing applications [5]. However, these waveforms are not optimized for sensing purposes as they are in typical radar systems. Such system requires a robust and computationally efficient signal processing algorithm for the extraction of MPC parameters from the received data of a noisy environment.

A variety of algorithms exist for Multipatch Component (MPC) estimation in wireless channels. These algorithms can be divided into three categories: spectral estimation, subspace-based techniques and maximum likelihood techniques. Multiple signal classification (MUSIC) and estimation of signal parameters via rotational invariance technique (ESPRIT) algorithms are representatives of the first two categories, and Space Alternating Generalized Expectation-Maximization (SAGE) and RIMAX algorithms are representatives of the third [6]–[8]. Existing algorithms, on the other hand, are designed for multi-antenna systems, in which each antenna has its own RF chain and baseband representation.

In this paper, we adapt the SAGE algorithm for MPC parameter estimation by utilizing all joint beam steering directions of the receiver and the transmitter, which differs from conventional channel parameter estimation that utilizes received baseband data for each antenna. When using a 28 GHz beam steering multi-antenna array, there are

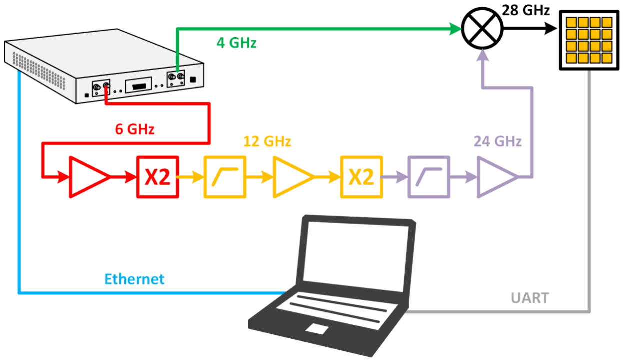

Fig. 1. Block-diagram of the 28 GHz transmitter.

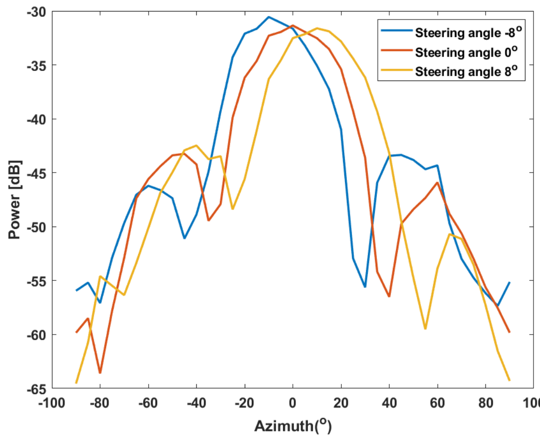

Fig. 2. Radiation patterns of the proposed antenna array at different angles

two challenges to MPC identification. The first is that the wide beamwidth of the array's radiation pattern can conceal smaller MPCs. The second is the presence of high-power side lobes, which makes it challenging to determine MPC contributions. The performance of the proposed algorithm is demonstrated by utilizing the measured power profile in a typical office environment. In particular, because the proposed approach aims to map the indoor environment using MPC parameter estimation, we show promising results in reproducing scatterer angular information.

The original contributions of this study are summarized as follows:

- This study develops a signal model for phased antenna array-based beam steering for directional scanning; in addition, the formulation and implementation of the adapted SAGE algorithm are presented;
- The channel measurement results from an indoor office environment at a mmWave band of 28 GHz are presented and the angular information of all corresponding scattering devices is extracted from MPCs.

The rest of the paper is organized as follows. Section II presents the signal model. Section III reports the description of the proposed algorithm, while Section IV discusses the performed measurement campaign, and the results are reported. Finally, Section V draws the conclusions.

Notations: in this paper, $(\cdot)^T$ denotes the transpose, $|\cdot|$ represents the amplitude, bold capital letters (e.g. $\mathbf{X}$) represent matrices, bold lower-case letters (e.g. $\mathbf{f}$) represent vectors, and non-bold letters represent scalars.

II. Signal Model

In this section, we will consider the signal model when a mmWave system is used with only a single baseband chain, and a digitally-controlled phased array that can form a beam in a direction θ_m. Such an architecture is shown for a transmitter in Figure 1 (this architecture will be detailed in Section IV).

Let us assume that the phased array, when steering in direction θ_m, has a radiation pattern $f(\theta_l, \theta_m)$ where θ_l is the direction in which the radiation pattern is measured. Figure 2 shows such a measured radiation pattern for an antenna array for different steering directions (the details of the experimental setup will be given in Section IV).

If the transmitter sends a signal $x(t)$ when the transmitter is steering in direction θ_m, the signal sent in direction θ_l is given by

$$x(\theta_l, \theta_m, t) = f(\theta_l, \theta_m) \cdot x(t) \tag{1}$$

Let us assume that the transmitter and receiver both have the same architecture (a single baseband chain with a digitally-controlled phased array) and an identical radiation pattern $f(\theta_l, \theta_m)$ when steering in direction θ_m. The channel is considered to be a multipath channel with L propagation paths that have complex amplitudes α_l, departure angles θ_l^{Tx} and arrival angles θ_l^{Rx}, with $l = 1, ..., L$. When the transmitter is steering in direction θ_m^{Tx} and the receiver is steering in direction θ_m^{Rx}, the received signal is given by:

$$y(\theta_m^{Rx}, \theta_m^{Tx}, t) = x(t) \cdot \sum_{l=1}^{L} \alpha_l f(\theta_l^{Rx}, \theta_m^{Rx}) f(\theta_l^{Tx}, \theta_m^{Tx}) + n(t) \tag{2}$$

where $n(t)$ represent the i.i.d. Gaussian noise. Note that (2) does not consider the propagation delay, but rather a narrowband channel (or a single carrier in a multicarrier system). In the previous development, we also assume that all propagation is done in the azimuth plane and ignore elevation.

Let us call $Y(\theta_m^{Rx}, \theta_m^{Tx})$ the complex amplitude of a single received packet (when the receiver steers in direction θ_m^{Rx} and the transmitter steers in direction θ_m^{Tx}). When both transmitter and receiver steer in all possible directions, the collected complex amplitudes will create a 2-D matrix $\mathbf{Y}$ that should show peaks at the angles of the MPCs $(\theta_l^{Rx}, \theta_l^{Tx})$. The size of $\mathbf{Y}$ is $K^{Rx} \times K^{Tx}$, where K^{Rx} and K^{Tx} represent the number of steering directions for the receiver and the transmitter, respectively.

Such a 2-D map is shown in the experimental result in Figure 4, where the colormap represents the power spectrum as a function of transmit and receive steering angle. In this figure, the Line-of-sight can be clearly be observed at $(\theta_l^{Rx}, \theta_l^{Tx}) = (0°, 0°)$. The contribution of the reflected paths (at $(\theta_l^{Rx}, \theta_l^{Tx}) = (30°, -30°)$ and $(\theta_l^{Rx}, \theta_l^{Tx}) = (-30°, 30°)$) can also be observed, but are more difficult to distinguish from the sidelobes of the antenna array (for example at $(\theta_l^{Rx}, \theta_l^{Tx}) = (0°, 60°)$). The SAGE algorithm presented in the next section allows us to identify the contributions of the MPCs without ambiguity by exploiting knowledge of the radiation pattern.

Based on (2), the signal model for the contribution of a single MPC to $\mathbf{Y}$ is given by:

$$\mathbf{S}_l = \alpha_l \cdot \mathbf{f}^T(\theta_l^{Rx}) \cdot \mathbf{f}(\theta_l^{Tx}) \tag{3}$$

where $\mathbf{f}(\theta_l^{Rx})$ is a $1 \times K^{Rx}$ vector containing the value of the radiation pattern of the receiver in direction θ_l^{Rx} for all receiver steering directions θ_m^{Rx}. Similarly, $\mathbf{f}(\theta_l^{Tx})$ is a $1 \times K^{Tx}$ vector containing the value of the radiation pattern of the transmitter in direction θ_l^{Tx} for all transmitter steering directions θ_m^{Tx}. By considering (2) and (3), it can be observed that

$$\mathbf{Y} = \sum_{l=1}^{L} \mathbf{S}_l + \mathbf{N} \tag{4}$$

where $\mathbf{N}$ is a $K^{Rx} \times K^{Tx}$ noise matrix containing i.i.d. Gaussian elements, representing the noise on the complex amplitude for each transmiter and receiver steering direction.

III. Algorithm

The SAGE algorithm is a popular method for multipath parameter estimation in wireless communication systems, which can take into account calibration and antenna pattern characteristics. It is a maximum-likelihood estimator that uses an iterative approach to estimate the multipath parameters from the received signal [9], [10]. It has been extensively researched in the literature in a variety of scenarios, including indoor and outdoor environments, as well as various wireless communication standards such as Wi-Fi, cellular, and satellite communication [9].

One of the main problems of using beam steering arrays for environment mapping is the presence of high sidelobes in the antenna array, as shown in Figure 4. While strong contributions (such as the Line-of-sight) can easily be identified, it is more difficult to distinguish whether smaller contributions are multipath components or contributions from the sidelobes of the antenna array.

The SAGE algorithm relies on iterative Expectation-Maximization (EM) steps. The observable data of the l^{th} MPC is computed using the first estimates of the $L-1$ MPCs in the expectation step. This step consists of removing the first $L-1$ estimated MPCs from the measured channel matrix. If the first $L-1$ MPC estimates are reliable, there will only be the l^{th} MPC's contribution left. The spatial parameters (angular and temporal) of the l^{th} MPC are then updated in the maximization step, alongside its estimated amplitude. The algorithm converges when the variance in the parameter estimates between two subsequent iterations falls below a predetermined threshold. It should be noted that the initialization step is crucial in the SAGE algorithm to guarantee that the algorithm converges to the global optimum (rather than a local one).

The main difference of the algorithm used in this paper concerns the signal model: instead of having received baseband data for each antenna (as is the case in classical MIMO channel estimation), our algorithm exploits the received baseband data for each steering direction of the Tx and Rx arrays' beam. This requires careful measurement of the array's radiation pattern (for each steering direction) but allows our algorithm to distinguish contributions of MPCs from contributions due to sidelobes of the antenna array.

A. Expectation-Maximization algorithm

The expectation and maximization step are repeated iteratively for each MPC l, for a certain number of iterations. In these two steps, the observable data for each path, along with their angular parameters, are estimated until they converge using the threshold method.

Expectation step: In this step, the estimation of the observable data of the l^{th} path is performed by removing $L-1$ path contributions (i.e. the most recent MPC estimates), as shown in the following equation:

$$\hat{\mathbf{X}}_l^{(i)} = \mathbf{Y} - \sum_{l'=1, l' \neq l}^{L} \mathbf{S}_{l'}^{(i)} \tag{5}$$

where $\mathbf{Y}$ is the 2-D matrix containing all measured complex received amplitudes (for all transmit and receive steering directions), and $\mathbf{S}_{l'}^{(i)}$ is the signal model defined in (3) for MPC l' at the i-th iteration.

Maximization step: in this stage, all the parameters of MPC l are updated (from iteration i to iteration $i+1$) as follows:

$$(\hat{\theta}_l^{Rx(i+1)}, \hat{\theta}_l^{Tx(i+1)}) = \underset{(\theta_m^{Rx}, \theta_m^{Tx})}{\operatorname{argmax}} (|\hat{\mathbf{X}}_l^{(i)}|) \tag{6}$$

where the search is performed over all elements of $\hat{\mathbf{X}}_l^{(i)}$, i.e. overall steering directions of the transmitter and receiver array. In other words, since $\hat{\mathbf{X}}_l^{(i)}$ is supposed to contain only the contribution of the l-th path (if the expectation step was effective), the indexes of the maximum in the power spectrum indicate the directions of the l-th MPC.

The complex amplitude $\alpha_l^{(i+1)}$ is updated as follows:

$$\alpha_l^{(i+1)} = \hat{\mathbf{X}}_l^{(i)}(\hat{\theta}_l^{Rx(i+1)}, \hat{\theta}_l^{Tx(i+1)}) \tag{7}$$

In other words, the complex amplitude of path l is that of $\hat{\mathbf{X}}_l^{(i)}$ at the maximum value in it's power spectrum.

B. *Initialization stage*

As mentioned previously, it is important to properly initialize the parameters $(\alpha_l^{(0)}, \theta_l^{Rx(0)}, \theta_l^{Tx(0)})$ for $l = 1, ..., L$ for the SAGE algorithm to converge to the global optimum.

During the initialization step, each individual path's parameters are initialized by successive path cancellation from the received signal strength matrix $\mathbf{Y}$. First, the residual measurement for the previously estimated paths is computed:

$$\mathbf{Y}_{res,l} = \mathbf{Y} - \sum_{l'=1}^{l-1} \mathbf{S}(l') \tag{8}$$

Then, the parameters of the l^{th} path are estimated from the residual measurement:

$$(\hat{\theta}_l^{Rx(0)}, \hat{\theta}_l^{Tx(0)}) = \underset{(\theta_m^{Rx}, \theta_m^{Tx})}{\operatorname{argmax}} (|\mathbf{Y}_{res,l}|) \tag{9}$$

Similarly, the complex amplitude is estimated as follows:

$$\alpha_l^{(0)} = \mathbf{Y}_{res,l}(\hat{\theta}_l^{Rx(0)}, \hat{\theta}_l^{Tx(0)}) \tag{10}$$

Such an initialization relies on the fact that the highest peak in the power spectrum of the (residual) measurement must indicate the presence of an MPC.

IV. Experimental Setup and Results

A. *Experimental setup*

The software defined radios (SDRs), up- and down- converter, and multi-antenna arrays are the three different components used to realize the 28 GHz SDRs-based transceiver system. The SDRs are used to process signals at sub-6 GHz (i.e. to generate the baseband and intermediate frequency signals). The up- and down-conversion components are used to convert the signal to 28 GHz and to sub-6GHz, respectively. An antenna array receives the upconverted 28 GHz RF signal for transmission, with a digital control port controlling the beam direction. Figure 1 depicts the block diagram of the proposed 28 GHz transmitter; the receiver has a very similar block diagram.

We employ a phased array antenna system to generate and steer beams towards different directions in the indoor environment. Figure 2 shows the proposed antenna array radiation patterns at given steering angles. It is demonstrated that the maximal directions of the patterns change depending on the beam steering angles. The received signal strength information at various points in the environment is collected and processed using the SAGE algorithm to estimate the angular information of the MPCs. Figure 3 depicts the environmental setup.

B. *Results*

The matrix of measured complex amplitudes $\mathbf{Y}$ measured in the environment was fed into the SAGE algorithm to obtain parameter estimates for a given number of paths. The antenna radiation pattern of the antenna array was measured in an anechoic chamber (for each steering direction) to obtain the vector $\mathbf{f}(\theta_l)$ for all values of θ_l.

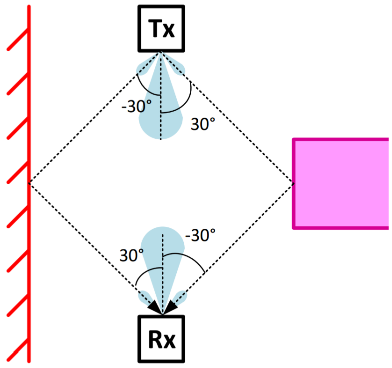

Fig. 3. Scenario of the measurements.

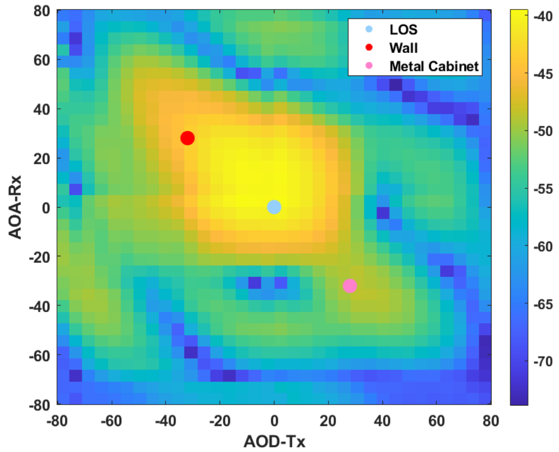

Fig. 4. Power spectrum as a function of transmitter and receiver steering angle. The MPCs estimated with SAGE are superimposed to the power spectrum, and identified as the LOS, wall reflection, and metal cabinet reflection.

The power spectrum of the measured data is shown in Figure 4. It can be seen that the power associated with MPCs and the sidelobes associated with the LoS path are in the same order of magnitude, highlighting the necessity of using an algorithm that is able to include the effect of the radiation pattern.

The proposed SAGE algorithm extracts angular information successfully, as shown in Figure 4 for the scenario depicted in Figure 3. From the figure, the estimated MPCs are pointed by colored circular circles. The LoS path has a power 5 dB higher than non-LoS (NLoS) paths and contributes significantly to 28 GHz wave propagation in an indoor environment. The second most powerful MPC is the wall reflection, The metal cabinet reflection has the lowest power. Although there are a limited number of MPCs in this experiment, the proposed algorithm produces a promising result; however, as the number of paths increases, more parameters are required to distinguish between the various paths.

V. Conclusion

In this paper, we use the SAGE algorithm to perform a preliminary identification of MPC contributions. A 28 GHz beam steering transceiver architecture based on SDRs with 4X4 antenna arrays was presented. The suggested SAGE algorithm utilizes the provided multi-antenna array radiation pattern for each steering direction to distinguish the MPC contribution. In an indoor setting, a preliminary measurement campaign was carried out. The walls and metal cabinets within the indoor environment are then located using the estimated angular information. After analyzing the experiment results, we concluded that the proposed SAGE algorithm can provide accurate estimates for nearly all MPCs if the channel contains only a few MPCs and experiences moderate power decay.

Acknowledgements

The authors acknowledge the financial support of the Belgian F.R.S.-F.N.R.S. through the MIS project F.4538.22 “SYNCH-NET” and the CDR project J.0146.23 “SCAM-28”.

References

[1] M. Passoja, “5G NR: Massive MIMO and Beamforming–What Does It Mean and How Can I Measure It in the Field,”, 2018.

[2] Carlos Baquero Barneto, Elizaveta Rastorgueva-Foi, Musa Furkan Keskin, Taneli Riihonen, Matias Turunen, Jukka Talvitie, Henk Wymeersch, Mikko Valkama, ”Millimeter-wave Mobile Sensing and Environment Mapping: Models, Algorithms and Validation”, IEEE Transactions on Vehicular Technology, 2022.

[3] Yi Zhong, Tianqi Bi, Ju Wang, Jie Zeng, Yan Huang, Ting Jiang, Qiang Wu, Siliang Wu: ”Empowering the V2X Network by Integrated Sensing and Communications: Background, Design, Advances, and Opportunities.” IEEE Netw. 36(4): 54-60 (2022).

[4] Emanuele Grossi, Marco Lops, Antonia Maria Tulino, and Luca Venturino. 2021. ”Opportunistic Sensing Using mmWave Communication Signals: A Subspace Approach.” IEEE Trans. Wirel. Commun. 20, 7 (2021), 4420–4434, (2021).

[5] M. A. Islam, G. C. Alexandropoulos and B. Smida, ”Integrated Sensing and Communication with Millimeter Wave Full Duplex Hybrid Beamforming,” ICC 2022 - IEEE International Conference on Communications, Seoul, Korea, Republic of, (2022).

[6] B. H. Fleury, M. Tschudin, R. Heddergott, D. Dahlhaus, and K. I. Pedersen, ”Channel parameter estimation in mobile radio environments using the SAGE algorithm,” IEEE J. Sel. Areas Commun., vol. 17, no. 3, pp. 434–450, Mar. (1999).

[7] Feng R, Huang J, Sun J, et al. A novel 3D frequency domain SAGE algorithm with applications to parameter estimation in mmWave massive MIMO indoor channels. Sci China Inf Sci, 2017, 60(8): 080305, doi: 10.1007/s11432-017-9139-4

[8] D.P. Gaillot, E. Tanghe, P. Stefanut, W. Joseph, M. Lienard, et al.. ”Accuracy of specular path estimates with ESPRIT and RiMAX in the presence of diffuse multipath.” 12th COST 2100 Management Committee Meeting, 2010, Bologna, Italy. ⟨hal-00574430⟩.

[9] A. Richter, “Estimation of radio channel parameters: models and algorithms”, Thesis, TU Iimenau, (2005).

[10] X. Yin, C. Ling, and M.-D. Kim, ”Experimental multipath-cluster characteristics of 28-GHz propagation channel,” IEEE Access, vol. 3, pp. 3138–3150, (2015).

Multistatic Fusion of Beamforming Feedbacks and Passive Wi-Fi Radar for AoD-based Localization

1st Martin Willame
ICTEAM-ELEN
Université catholique de Louvain
Université Libre de Bruxelles
Louvain-la-Neuve, Belgium
martin.willame@uclouvain.be

2nd Laurent Storrer
OPERA-WCG
Université Libre de Bruxelles
Brussels, Belgium
laurent.storrer@ulb.be

3rd Hasan Can Yildirim
OPERA-WCG
Université Libre de Bruxelles
Brussels, Belgium
hasan.can.yildirim@ulb.be

4th François Horlin
OPERA-WCG
Université Libre de Bruxelles
Brussels, Belgium
francois.horlin@ulb.be

5th Jérôme Louveaux
ICTEAM-ELEN
Université catholique de Louvain
Louvain-la-Neuve, Belgium
jerome.louveaux@uclouvain.be

***Abstract*—Passive Wi-Fi based Radars (PWR) are devices that can localize targets using a Wi-Fi signal-of-opportunity transmitted by an Access Point (AP). The recent development of Wi-Fi Sensing has led to a growing interest in the use of multistatic radar configurations, combining the estimated target parameters from multiple transmitters and receivers to jointly perform target localization. On the one hand, the Maximum Likelihood (ML) framework can be used to perform Angle of Departure (AoD)-based localization of multiple targets. However, it requires a high complexity multi-dimensional search. On the other hand, MUSIC reduces the complexity to a one-dimensional search but no framework is derived for the combination of multiple bistatic pairs. In this paper, the relationship between MUSIC and ML estimators is exploited to perform an ML subspace based AoD estimation. In addition to the passive radar processing based on known OFDM preambles transmitted by the APs, the proposed method also exploits the AoD information contained in the Beamforming Feedback (BFF) transmitted by the clients during the channel sounding session. This low level data combination of multistatic information, obtained from preambles and BFFs, outputs a surveillance map from which targets detection can be performed using a Constant False Alarm Rate (CFAR) detector. A numerical analysis is presented to assess the accuracy of the proposed combination method and to demonstrate its benefit compare to other fusion methods.**

***Index Terms*—Passive Wi-Fi Radar, Multistatic, Data Fusion, Maximum Likelihood, MUSIC, Beamforming Feedback.**

I. Contributions

Our contributions can be summarized as follows:

- We propose a low level data fusion methodology based on the Maximum Likelihood (ML) framework for Angle of Departure (AoD)-based localization of K human targets in a multistatic Passive Wi-Fi based Radar (PWR) configuration. The method exploits the relationship between the MUSIC and ML estimators shown in [1] to reduce the complexity of the K-dimensional search of the ML estimator into K one-dimensional problems solved by MUSIC.
- Our method combines the AoD estimations from multiple Access Point (AP)-PWR pairs (based on known preambles) with the estimation from Beamforming Feedbacks (BFFs) sniffed during the channel sounding session initiated by the APs with its clients.

II. System Model

In this work, we use a multistatic configuration with multiple transmitter APs and only one receiver PWR. The positions (x_k, y_k) of the targets are determined only from their estimated AoD ϕ_k. The baseband equivalent channel model is estimated either by the client,to build its BFF, or the PWR from the NDP transmitted by the AP. As we focus on a AoD-based localization, the full channel model knowledge is not exploited and the channel coefficients across receiving antennas and subcarriers are estimated independently. The channel model can thus be simplified as

$$\mathbf{H}_q(\mathbf{\Phi}) = \mathbf{X}_q \mathbf{A}^{\mathrm{H}}(\mathbf{\Phi}) + \mathbf{N}_q, \tag{1}$$

where $\mathbf{X}_q$ is a $(M \times K)$ matrix of channel coefficients and $\mathbf{A}(\mathbf{\Phi}) = [\mathbf{a}(\phi_1), \ldots, \mathbf{a}(\phi_K)]$ is the AoD steering matrix $(N \times K)$. M (resp. N) is the number of transmitting (resp. receiving) antennas and K is the number of targets.

III. Data Fusion from ML to MUSIC

We show that the ML function from each bistatic pairs can be approximated by

$$\mathcal{L}(\hat{\mathbf{\Phi}}) \approx \frac{QN}{2\sigma^2} \sum_{k=1}^{K} \tilde{s}_k \; \mathbf{a}^{\mathrm{H}}(\phi_k) \tilde{\mathbf{\Gamma}} \mathbf{a}(\phi_k). \tag{2}$$

where Q is the number of subcarriers and σ^2 is the noise variance. The terms $\tilde{s}_k$ and $\tilde{\mathbf{\Gamma}}$ are estimated by the proposed method with a one-dimensional search based on MUSIC outputs. The surveillance map is then obtained by adding the individual likelihood functions.

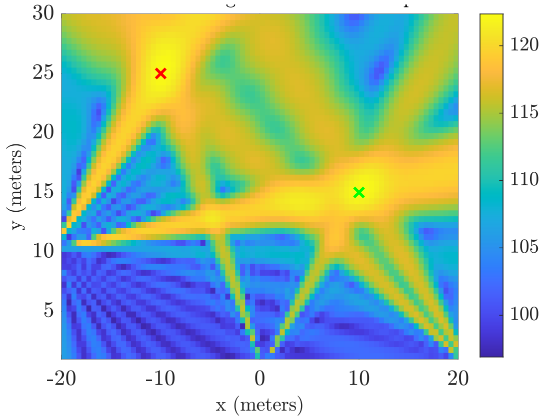

IV. Simulation Results

Monte-Carlo simulations are performed to assess the improvement brought by the proposed fusion process on the localization accuracy compared to the two other methods. For each simulation, 2 targets and 1 client device are randomly placed in an (x, y) map of size $40 \times 30[m]$. The figure displays the surveillance map obtained with the proposed combination method.

References

[1] P. Stoica and A. Nehorai, "MUSIC, maximum likelihood and Cramer-Rao bound," ICASSP-88., International Conference on Acoustics, Speech, and Signal Processing, New York, NY, USA, 1988, pp. 2296-2299 vol.4, doi: 10.1109/ICASSP.1988.197097.

Group Counting Using Micro-Doppler Signatures From a 77GHz FMCW Radar: A CNN Approach

1st Dejvi Cakoni
OPERA - WCG
Université Libre de Bruxelles
Brussels, BE
dejvi.cakoni@ulb.be

2nd Laurent Storrer
OPERA - WCG
Université Libre de Bruxelles
Brussels, BE
laurent.storrer@ulb.be

3rd Philippe De Doncker
OPERA - WCG
Université Libre de Bruxelles
Brussels, BE
philippe.dedoncker@ulb.be

4th François Horlin
OPERA - WCG
Université Libre de Bruxelles
Brussels, BE
francois.horlin@ulb.be

***Abstract*—People counting and detection technologies have shown great versatility in various scnearios and have become an important tool for event organizers and city planners to optimize their operations. This paper presents a novel approach for people counting using Micro-Doppler Signatures (MDS) extracted from a Frequency-Modulated Continuous-Wave (FMCW) radar operating at 77GHz. The system utilizes the unique gait model of each individual, which results in a distinct MDS, to classify groups of different sizes using a Convolutional Neural Network (CNN). The proposed system overcomes the limitations of existing people counting techniques such as the need for a clear line of sight and being affected by lighting conditions**

***Index Terms*—group counting, radar signal processing, 77 GHz FMCW radar, CNN, micro-Doppler signature**

I. Introduction

In recent years, with the increased concern in public safety, there has been a growth in the demand for crowd surveillance and safety management systems. The estimation of crowd dynamics can help in preventing unanticipated accidents or issues in case of mass events or be of use for city planners to improve the daily commutes of it's citizens. These systems can be implemented in various ways as, for example, image or video-based techniques. However, radar-based crowd monitoring systems are being considered due to their non-invasive properties and ability to work in low lighting conditions, things that the previous systems are lacking.

When it comes to counting people in a scene with a radar, most existing works in the literature consider an indoor, office-like environment where a few individuals (less than ten in practice) are mobile. Since people in this environment move at very low speeds, the radar mostly relies on the range information to estimate the number of individuals in the room [1]. Most of the existing radars for people counting are based on the impulse-radio ultrawideband (IR-UWB) waveform, which compared to Frequency Modulated Continuous waveform (FMCW) provides a much better range resolution but poor Doppler resolution. Low-accuracy estimates achieved with a mm-wave FMCW radar can also be improved by using information coming from other devices like cameras [2] or by finely observing the vital signs like the heartbeat or the breathing rates with the radar. [3]. Recently, it has been shown that applying Machine Learning and Deep Learning algorithms to radar data improves the system performance [1] [6]. However, these algorithms rely on just range information or Range Doppler Maps (RDMs) as inputs to the network. Distinctly, in this work we will use the Micro-Doppler Signatures (MDSs) as input to our Convolutional Neural Network (CNN). Furthermore, we will target an outdoor pedestrian street scenario where people are typically walking together in groups.

The rest of the paper is organized as follows : Section II describes the fundamental workings of the FMCW radar. Next Section III explains the human gait modelling along with the simulation scenario. Section IV presents the CNN architecture and the results achieved. Finally, we conclude this paper and discuss future directions in Section V.

II. System Architecture

A. FMCW Radar system

Frequency-Modulated Continuous-Wave (FMCW) radar is a type of radar that operates by transmitting a continuous wave signal that is modulated with a linear frequency ramp. This ramp causes the transmitted signal to continuously increase or decrease in frequency over time. This transmitted signal is called a chirp. The FMCW signal is composed of a finite series of K chirps, each of instantaneous frequency linearly increasing with the time.

When the transmitted signal encounters a target object, some of the signal is reflected back to the radar receiver. The received signal is then mixed with the transmitted signal and low-pass filtered to cancel out replicas at twice the carrier frequency. The resulting frequency is proportional to the distance between the radar and the target object. By analyzing the resulting frequency signal, FMCW radar can determine the range, speed and, in case of multiple antennas, Angle

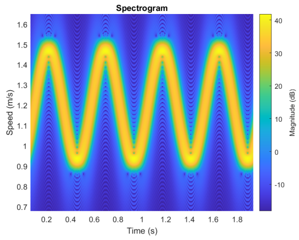

(a) Single person MDS

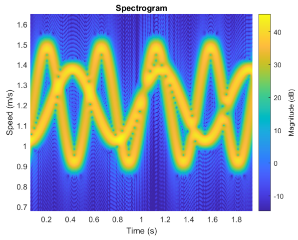

(b) Two people MDS

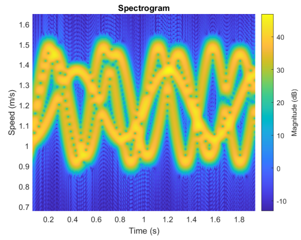

(c) Three people MDS

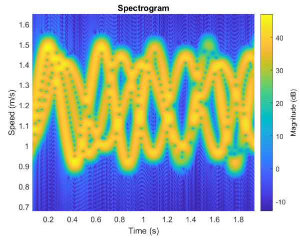

(d) Four people MDS

Fig. 1: First class label

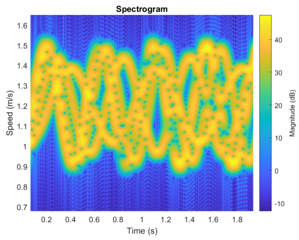

(a) Five person MDS

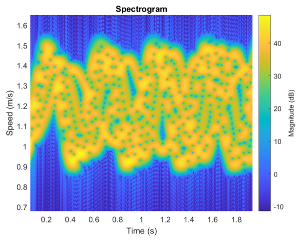

(b) Six people MDS

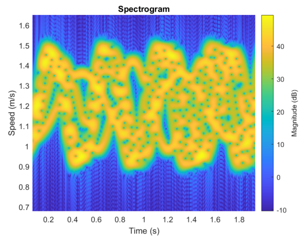

(c) Seven people MDS

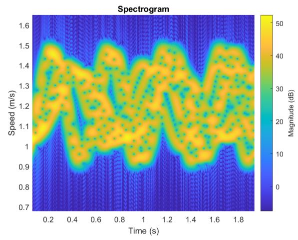

(d) Eight people MDS

Fig. 2: Second class label

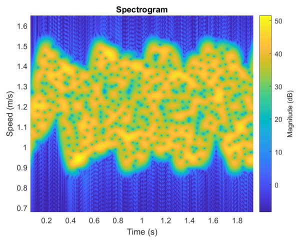

(a) Nine person MDS

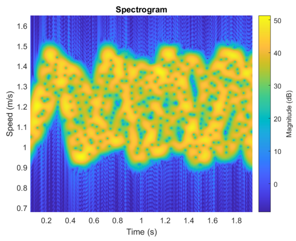

(b) Ten people MDS

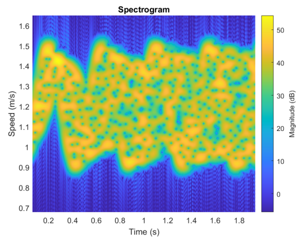

(c) Eleven people MDS

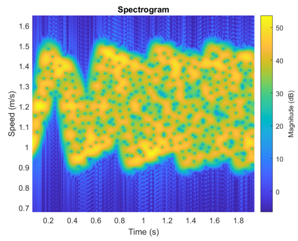

(d) Twelve people MDS

Fig. 3: Third class label

of Arrival (AoA) of target objects. This work is based on the Texas Instrument AWR1843 FMCW radar operating at 77GHz. Focusing on chirp k and denoting each chirp duration by T and the frequency bandwidth swept as B the time can be expressed as :

$$t = kT + t' \tag{1}$$

where $k = 0, \cdots, K-1$ and $t' \in [0, T]$. This enables us to write the instantaneous frequency as:

$$f_i(t) = \beta t' \tag{2}$$

where $\beta = \frac{B}{T}$ is called the frequency slope. The transmitted signal is then mathematically expressed as:

$$s(t) = \cos(2\pi f_c t + \phi_i(t)) \tag{3}$$

where f_c is the radar carrier frequency and $\phi_i(t)$ is the instantaneous phase resulting from the FMCW modulation equal to :

$$\begin{aligned} \phi_i(t) &= 2\pi \int_{u=0}^{t} f(u)\, du \\ &= \pi k \beta T^2 + \pi \beta t'^2 \end{aligned} \tag{4}$$

At the receiver, the resulting baseband signal caused by a single target reflection is

$$x(t) \approx \kappa \exp(j2\pi f_B t') \exp(j2\pi f_D kT) \tag{5}$$

where κ is a complex factor that integrates the gain and all constant phase terms. By measuring f_D and f_B the targets velocity and range can be resolved respectively since they are defined as :

$$f_D = 2\frac{v f_c}{c} \tag{6}$$

$$f_B = 2\frac{R_0 \beta}{c} \tag{7}$$

where v denotes the targets speed , R_0 the targets range and c the speed of light.

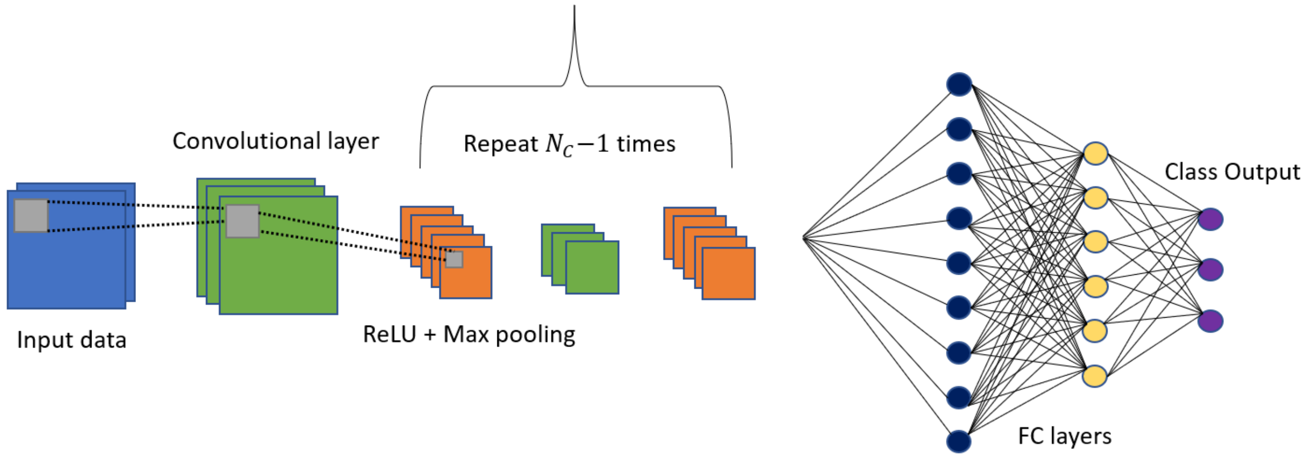

Fig. 4: CNN Architecture

B. Radar Signal Processing

A 2D matrix of size $K \times L$ is formed by acquiring and sampling the mixed signal accros consecutive chirps for a single transmit antenna, with K being the number of transmitted chirps and L the number of samples per chirp. Next the Range-Doppler Map (RDM) is computed by first taking a Fast Fourier Transform (FFT) along the fast time for all chirps to obtain the so-called Range Rrofile (RP) containing the range information of the targets, followed by another FFT along the slow time to obtain Doppler information. Before performing the respective 1D FFTs, a mean subtraction is performed along both fast time and slow time.
However, in cases of groups walking together it is not possible in the RDM to distinguish and count the number of people as they appear as a single peak in the RDM. As discussed previously the frequency components of the targets will vary over time. In such way, the standard Fourier Transform is not suitable since it projects the signal on infinite sinusoids which are totally not localized in time and thus, it provides the frequency information averaged over the whole signal time interval. In these cases, it is necessary to move from mono-dimensional solutions to bi-dimensional functions (functions depending on both time and frequency) such as the Short Time Fourier Transform (STFT). Thus, our radar processing is as follows :

- Determine the RDM using a 2-D Fourier Transform.
- In the RMD, detect the group by finding the maximum power peak.
- Extract and concatenate the resulting peak index across all chirps in the RP.
- Perform STFT on the concatenated signal to extract the spectrograms i.e, MDS.

III. Human Gait Modelling

To study how the MDS evolve with the increasing number of targets in the scene, it is inevitable to resort to simulations based on either mathematical or empirical models. A frequently used empirical model to generate micro-Doppler gait signatures is the global human walking model developed by Boulic, Magnenat-Thalman and Thalman [5]. The model generates the signatures by describing the position and orientation of 12 different human body parts. However, in this work we will consider just the torso as our point target, superimposed to the groups average speed. This is done because the torso appears as the maximum power in these signatures. Examples of simulated MDSs for different group sizes can be seen in Figs.1,2,3. Here it must be noted that the simulated MDS are of targets moving away from the radar, which we are considering as a positive frequency shift.

IV. Simulation and CNN Results

A. Dataset Simulation and Class Lables

We simulate varying group sizes (1-12 people) in a pedestrian street. For each group size 100 MDS are simulated and generated leading to a dataset of 1200 MDS samples. These MDSs are then fed to a CNN in order to perform a classification task to estimate the group sizes. Some examples of the MDSs generated can be seen in Fig. 1,2,3. The goal is to count and classify different groups of people, thus we build our classes based on intervals of number of people. Considering 3 groups classes, the class lables decided are as follows :

- Class 1 : 1-4 people - Low sized group
- Class 2 : 5-8 people - Mid sized group
- Class 3 : 9-12 people - High sized group

B. CNN Architecture

A classical CNN architecture is implemented here, and displayed in Fig. 4. It consists of a features extraction part with $N_C = 3$ convolutional blocks, and a classification part with $N_{FC} = 3$ fully connected (FC) layers followed by a softmax layer. Each MDS is scanned by the convolutional layers, followed by a rectifier linear unit (ReLU) layer and a max pooling. After each set of convolutions followed by the ReLU and the max pooling, the size of the convolutional filters is decreased and their number is increased. This is done to scan the MDS at each step with a finer resolution filter so that the CNN can extract different and finer features at each step. The ReLU activation function was chosen for its ability to handle the $vanishing\ gradient$ problem [6]. To handle the complex values of the MDS its real and imaginary parts are treated as separate channels.

C. Classification Results

As can be seen in Fig. 5 the proposed CNN architecture achives an accuracy of around 88% for the considered classes on the testing set. Especially for the low and high sized groups the model achieves a better accuracy as the MDS are quite distinct compared to the mid sized group.

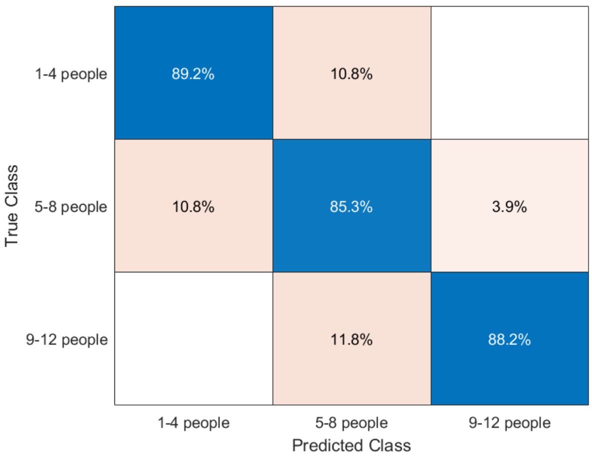

Fig. 5: Confusion Matrix for 3 classes

V. Conclusion and Future Work

In conclusion, we investigated the problem of radar based group counting using micro-Doppler signatures. We proposed a simulator based on the Boulic, Magenat-Thalman and Thalman model to generate spectrograms for varying group sizes. We tackled counting as a classification problem, and applied a CNN on the generated MDS and obtained high accuracy results for counting.

Future work includes an extensive measurement campaign and dataset collection, comparing the CNN architecture proposed to other Machine Learning methods and tackling larger group sizes.

References

[1] J. -H. Choi, J. -E. Kim, N. -H. Jeong, K. -T. Kim and S. -H. Jin, ”Accurate People Counting Based on Radar: Deep Learning Approach,” 2020 IEEE Radar Conference (RadarConf20), 2020, pp. 1-5, doi: 10.1109/RadarConf2043947.2020.9266496

[2] M. Stephan, S. Hazra, A. Santra, R. Weigel and G. Fischer, ”People Counting Solution Using an FMCW Radar with Knowledge Distillation From Camera Data,” 2021 IEEE Sensors, 2021, pp. 1-4, doi: 10.1109/SENSORS47087.2021.9639798.

[3] J. Weiß, R. Pérez and E. Biebl, ”Improved People Counting Algorithm for Indoor Environments using 60 GHz FMCW Radar,” 2020 IEEE Radar Conference (RadarConf20), 2020, pp. 1-6, doi: 10.1109/RadarConf2043947.2020.9266607.

[4] L. Servadei, H. Sun, J. Ott, M. Stephan, S. Hazra, T. Stadelmayer, D. S. Lopera, R. Wille, and A. Santra, “Label-aware ranked loss for robust people counting using automotive in-cabin radar,” 2021. [Online]. Available: https://arxiv.org/abs/2110.05876

[5] Boulic, R., Thalmann, N.M. & Thalmann, D. ”A global human walking model with real-time kinematic personification”. The Visual Computer 6, 344-358 (1990). https://doi.org/10.1007/BF01901021

[6] M. S. Seyfioğlu, A. M. Özbayoğlu and S. Z. Gürbüz, ”Deep convolutional autoencoder for radar-based classification of similar aided and unaided human activities,” in IEEE Transactions on Aerospace and Electronic Systems, vol. 54, no. 4, pp. 1709-1723, Aug. 2018, doi: 10.1109/TAES.2018.2799758.

Coded beam searching for bi-directional optical wireless communication system

Lev Azarkh
Signal Processing Systems
Eindhoven University of Technology
Eindhoven, the Netherlands
l.azarkh@tue.nl

Jean-Paul M. G. Linnartz
Signal Processing Systems
Eindhoven University of Technology, and Signify Research
Eindhoven, the Netherlands
j.p.linnartz@tue.nl, j.p.linnartz@signify.com

***Abstract*—In a communication system with steerable laser beams, the transmitter must find the direction towards the receiver. This requires a feedback loop such that the receiver can signal that the correct direction has been found. However, the receiver may not be able to instantly give high-resolution feedback if the beam hits its detector. At least during the acquisition phase, thus before transmitter and receiver are aligned in both directions, this feedback channel typically has a wider beam and a much lower bandwidth, thus a (possibly random) latency and a lower time resolution. It is often not practical to adaptively widen the optical beam during acquisition, but even if one designs for an adaptive beam width, it is not evident that this accelerates the search as we argue in this paper. The paper also describes a suitable address coding scheme based on maximum-length Linear Feedback Shift Register sequences, that accelerates the search significantly.**

I. INTRODUCTION

In optical wireless communications, it is a challenge to ensure that the laser beam covers the target client device. As it requires real-time knowledge of the direction towards the counter station, which may not always be available during the set up of a link. For LED-based communication systems, it is often solved by projecting a wide beam over a coverage area so that every possible position is covered within the light beam. This leads to a relatively weak signal, which limits the achievable bit rate. Lasers create more coherent light than LEDs and give more confined beams. Lasers also have a much broader modulation bandwidth than LED. But working within eye-safety limits for indoor optical communications means that using a relatively high power is prohibitive. Nonetheless, the use of a narrow beam is preferred for high bit rates and low power consumption.

The acquisition system may use a feedback loop such that the client device can transmit back when the beam from the central station found the correct position of the client. This feedback loop may have to use a wider beam, thus use a lower bandwidth, and may have unknown latency and timing offsets caused by creation and scheduling of data packets.

There are examples that report practical implementation of the search systems but that proves to be time-consuming [1], low precision, and power inefficient due to a large beam spot [2]. However, little literature has been devoted to quantified models for the benefits or drawbacks of a narrow beam, for instance in terms of acquisition search time. Also, the use of dedicated training and addressing sequences is yet not heavily researched. The idea of embedding identifiers or address codes was presented earlier, in [3], for the purpose of channel estimation and to identify the relative light contribution from multiple emitters, but not yet for beam steering.

This paper, to our knowledge, is one of the first in literature that models and evaluates the challenge of position acquisition. We propose a novel method of encoding the direction (or target position) of a steerable device using a linear feedback shift register (LFSR) code. This can improve the search time, compared to conventional address labeling.

For the time being, we ignore limitations caused by the mechanical time response of the steering devices. These may have a large impact on overall search time, but we believe that with the development of integrated photonic steering, mechanical effects would become less relevant, even to the point of not being the main limitation. We focus on limitations caused by the required energy per bit that the detector needs to recover an identifier embedded in the beam.

This paper is organized as follows: Section II and III formulate the model that shows that widening a beam may be counterproductive to accelerate beam searching. The choice of the beam width is described in Section IV. Section V proposes the use of an LFSR instead of discrete addresses.

II. SYSTEM MODEL

A. Considerations for a width of the search beam

Depending on its design, an OWC system with highly directional beams may have to execute a 4-dimensional search for the transmitter and receiver to align. Acceleration may be if the transmitter sends directional identifiers as it sweeps over the coverage area in search of its receiver location. If the receiver sees an identifier, it reports this via a feedback channel. However, this feedback channel is likely to have a lower bit rate and may have an unknown, variable, and possibly large delay.

In a typical communication setting, a received bit needs to have at least a certain minimum electrical energy to allow reliable detection. In an OWC receiver, a photodiode converts an arriving light intensity, that is, an optical *power* into an electrical signal *current* or voltage. The electrical power is proportional to *the square* of the optical power arriving at the detector.

This has an intriguing consequence if one has to send a message to a detector of size A_D, if the detector is located at an unknown location in a coverage area A_C that has N times the area of A_D: $A_C = NA_D$. Sending the message N times sequentially at full power sending a narrow beam $A_B = A_D$ is much faster than sending a message once, simultaneously to all possible locations, with $A_B = A_C$. The latter yields a signal-to-noise ratio (SNR) that is N^2 smaller than in the former strategy. Thus, to obtain the same received energy per bit, the latter system must run at a bit rate that is N^2 slower, but it only needs to send the message once. The former strategy (N times a narrow beam) is N times faster than the latter (one broad beam). The comparison would be different for RF. For RF, the two scenarios would be equally fast. To our knowledge, this effect has not been reported before. However, it implies that the design of an OWC needs to take the specific properties of SNRs into account.

A transmitter beams an optical power of Φ_T to a target receiver. If a detector captures the arriving photons by means of a detector with effective area A_D and the light intensity is uniform over A_B with $A_D << A_B$, the received optical light intensity, i.e., the optical power is

$$\Phi_R = \frac{A_D}{A_B}\Phi_T \tag{1}$$

A photodiode converts an incoming photon into a hole electron pair. Hence, the electron current is proportional to the photon density, thus to the electrical power is

$$P_{R,el} = h^2\eta_R^2\Phi_T^2. \tag{2}$$

The responsivity η_R expresses the efficiency of converting photons into electrons (amperes per watt). We defined the pathloss h for an optical system as h_o being the ratio of the optical received light intensity Φ_R over the transmit light intensity Φ_T. In lossless media, the law of conservation of energy implies that the entire light transmit power flows through A_B, thus $h_o = A_D/A_B$. So, the electrical received power relates to $h^2 = A_D^2/A_B^2$. This differs from h_{RF} in radio links where the power gain is inversely proportional to the beam width. For an optical system, the extra square in the received power has large consequences for an optimum system choice for A_B. For comparison, according to expression for RF free space loss, the electrical received power relates to $h_{RF}^2 = A_D/A_B$ if we take for A_D the antenna aperture and A_B the effective beam width.

Already (2) shows that increasing the radius of the beam but keeping to the total optical power constant reduces the energy per bit by the fourth power of the radius. However, for a fixed coverage area A_C, the number of positions that the beam needs to test grows with the square of the beam radius. Therefore, considering that the required energy per bit is a modulation constant, it is apparent that widening the laser beam may be counterproductive as the duration of sending each identifier will be also increased.

Most of the laser beams used in optical communications have, in good approximation, a Gaussian intensity distribution. Getting and keeping the center of the beam aligned with the detector is one of the key challenges for the system. Here, we address an approach for acquisition of the beam direction by a search.

B. Search time and effect of the beam size

The search time T_{scan} can be interpreted as the product of the number of bits per address ID, the number of different directions into which such an ID has to be sent times the bit duration. The beam width has a strong influence on the bit rate that can be used.

Considering a minimum required energy per symbol, the number of symbol levels that can be carried in M-PAM, thus with m bits per symbol can be obtained following [4] or Eq. (9) in [5]

$$M^2 = 2^{2m} = 1 + \frac{h^2\Phi_T^2}{\kappa\Gamma N_0 f_{max}} \tag{3}$$

where Γ is a modulation gap that is derived from bit error rate (BER), N_0 is a noise floor, κ is a noise enhancement that may occur of its parasitic capacitances of the PD needs to be compensated, and the bit rate is $R_b = 2m \cdot f_{max}$. We take $\kappa = 1$. If the detector die has a large size, measures to mitigate the capacitance may lead to a noise enhancement $\kappa > 1$ that grows with f_{max}. This may reduce the bit rate at which a very focused beam can be sent. Evaluation of this effect is outside the scope of this work and will be reported later in detail. To carry M-PAM with m bits per symbol, (3) reveals the need for minimum SNR, with

$$\text{SNR} = \frac{h^2\Phi_T^2}{\kappa N_0 f_{max}} \geq \Gamma(M^2 - 1). \tag{4}$$

If a certain signal power is available at the receiver and if the bandwidth f_{max} is limited beforehand, one may use the highest fitting M. If we restrict M to a power of 2 (integer m), this gives $R_b = 2f_{max}\log_2 M$, thus

$$R_b = f_{max}\left\lfloor \log_2\left(1 + \frac{h^2\eta_R^2\Phi_T^2}{\kappa\Gamma N_0 f_{max}}\right)\right\rfloor. \tag{5}$$

To simplify beam detection, $m = 1$ (OOK) or even bi-phase (Manchester) encoding may be preferred. To carry OOK, a minimum energy per bit is needed to ensure that in the above expression $\frac{1}{2}\lfloor\log_2(1 + ...)\rfloor \geq 1$ bit per symbol. We can rewrite the equations to express the highest achievable bit rate, by taking the highest possible f_{max} that gives adequate SNR:

$$R_b = 2f_{max} \leq 2h^2\frac{\eta_R^2\Phi_T^2}{\kappa\Gamma N_0}. \tag{6}$$

Via h^2, this is inversely proportional to A_B^2.

C. Address Identifiers

To encode the beam direction from the steering device with a resolution of A_R, we need $N_b = \lceil\log_2(A_C/A_R)\rceil$ bits. One may argue that for a beam spot size A_B and a uniform light level, it would be adequate to use $A_R = A_B$. However, this paper focuses on a pointing accuracy that aims the center of the beam towards the detector, thus $A_R = A_D$.

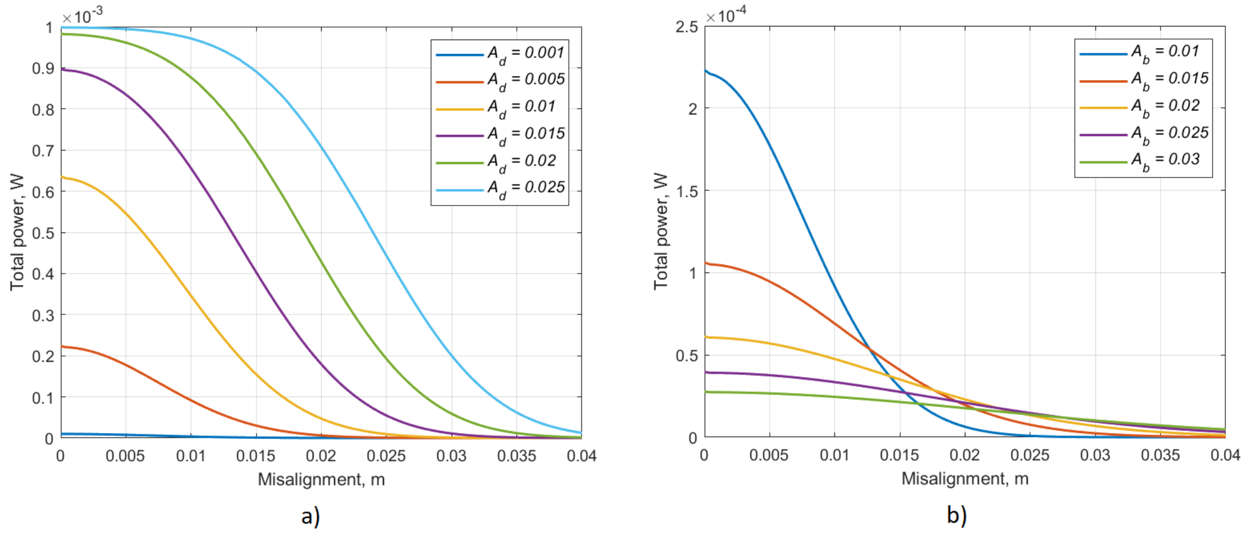

Fig. 1. The influence of the misalignment between the center of a beam with a Gaussian intensity profile and the photodetector. a) for different detector sizes A_D for $\Phi_T = 1$ mW and b) for different beam sizes A_B for $\Phi_T = 2.5$mW.

If the beam has a Gaussian distribution, this gives the highest SNR. We need $N_b = \log_2(A_C/A_D)$ bits. Taking into account N_h header bits, synchronisation bits, and other overhead, the time T_P spent per position follows from

$$T_P = \frac{N_b + N_h}{R_b}. \tag{7}$$

Typically, scanning occurs over N_Y lines, in each of which N_X positions are checked, with $N_b = N_X N_Y$. We do not consider mechanical speed limitations.

The key challenge of the steering mechanism is to align the beam optimally with the detector, therefore the desired resolution of the system is $A_R = A_D$. The number of positions for which an Address ID is needed is the size of the entire coverage area A_C divided by the required resolution A_R: we need $\lceil \log_2 A_C/A_R \rceil$ bits for the addresses. In a typical system, the coverage area may be scanned as N_Y lines of N_X positions on each line. Then $N_Y N_X \approx A_C/A_R$ where the approximation is because it ignores overlaps of A_R footprints to contiguously cover the entire area A_C.

D. Signal strength-limited systems

For any M-PAM, a minimum energy per bit E_b is needed, but OOK ($M = 2$) is the most power efficient. If excess power is available, we use that to make the symbol duration shorter (thus allowing very high f_{max}) rather than to increase M. For OOK, we find a scan time that equals the number of bits per address times the number of addresses times the duration of transmitting one bit:

$$T_{scan} = 2\left(\log_2 \frac{A_C}{A_R} + N_h\right) \frac{A_C}{A_R} \frac{\kappa \Gamma N_0}{h^2 \eta_R^2 \Phi_T^2}. \tag{8}$$

If we insert $h = A_D/A_B$, the counterproductive effect of increasing beam width becomes evident, as it reduces the received power and leads to $T_{scan} \propto A_B^2$:

$$T_{scan} = 2\left(\log_2 \frac{A_C}{A_R} + N_h\right) \frac{A_C}{A_R} \frac{A_B^2}{A_D^2} \frac{\kappa \Gamma N_0}{\eta_R^2 \Phi_T^2}. \tag{9}$$

We will compare the system performance as a function of Φ_T^2/N_0, thus for the same transmit power Φ_T and the same link budget. That implies that the SNR differs per system, depending on A_B and on the bandwidth f_{max} that the system can use. We explicitly note that comparing systems for the same SNR would be misleading. For Manchester encoded signals, a similar expression is found, considering rate 1/2 but it tolerates a lower signal power.

III. Comparison of Scan Times

The scanning strategy needs to send A_C/A_R address IDs and that a wider beam implies that a client device receives A_B/A_R such addresses and picks the one that is received at the highest strength. However, that is not the fastest strategy. Accelerated scans may need to change the beam width in successive scan steps to zoom-in after initially finding a position hit at limited A_B resolution. We leave that for further optimization.

Changing the beam size does not show linear dependencies of the scan time, as it also influences the SNR, thus the feasible bit rate. Increasing the beam size A_B also increases the time scan T_{scan} thus resulting in a slower acquisition 2. Therefore, it urges to use the smallest possible beam size A_B to minimize T_{scan}. Ideally, $A_B = A_D$. From Figs. 2 and 3 is it evident that for the proposed model, making the beam size larger does not result in a more effective scan. In later work, we will elaborate on this relation, and on appropriate

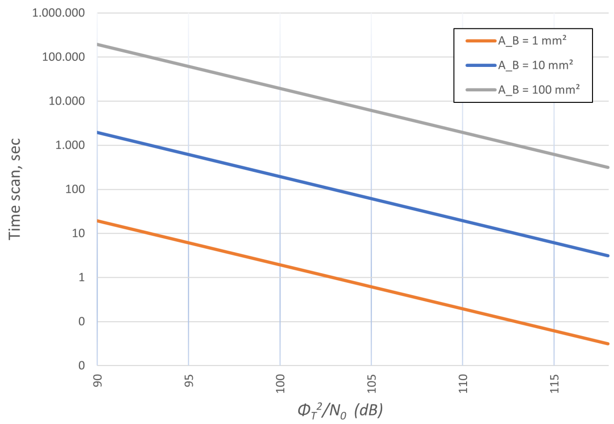

Fig. 2. The influence of Φ_T^2/N_0 over scan time for system with different widths of the beam.

choices for A_B. In fact, we see that A_B preferably is kept small.

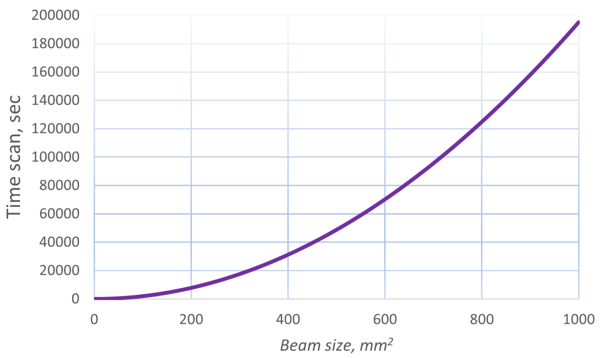

Fig. 3. Time to acquisition versus the size of the beam for the system with transmit power $\Phi_T = 1$ mW, detector size $A_D = 1$ mm^2, and a noise floor $N_0 = 10^{-14}$ W/Hz.

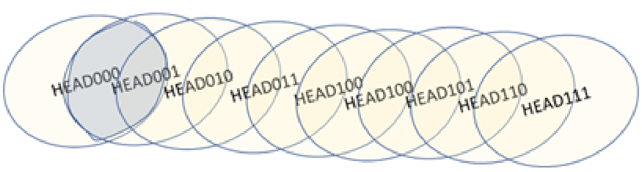

Fig. 4. Packetized address ID, similar to System 1 and 2. Yellow circles: beam are A_B. Grey: the area in which the first packet can be received fully. In this example, packets contain a header and three address bits. The resolution $A_R \approx A_B$.

IV. Beam width Choice

It is possible to use two different laser beams for communication and detector acquisition. But as we saw earlier, it is better to have a high bit rate channel for the searching part as well, as it directly affects the scan time. Therefore, it is reasonable to use one laser beam for both scanning and communication as it also simplifies the system. Then a switch is needed to go from the searching phase into communication.

During a search, there are different approaches to encode direction addresses to identify the position of the steering device as a modulation into the beam data. For the comparison of suggested systems, we keep key parameters constant. The responsivity of the photodetector $\eta = 0.7$ A/W, size of the detector is $A_D = 1$ mm^2, noise floor $N_0 = 10^{-14}$ W/Hz and coverage area $A_C = 16.8$ m^2. For BER $= 10^{-4}$, modulation gap $\Gamma = 4$. Number of the bits for the header $N_h = 64$. Transmit power Φ_T has been chosen in a way to guarantee eye-safe communication for all systems considered.

1) System 1: One, seemingly attractive option is to start with a beam that is artificially made very wide to have fewer steps for each scan line and to send a full address to each step-position which is how we modelled System 1. But this approach has several downsides. Firstly, beams usually have a Gaussian profile. If the system is not aligned perfectly, we can spot drastic losses in received power (Fig. 1). This leads a lower than ideal energy per bit, a lower signal-to-noise ratio and a higher BER.

Having a wide and uniform laser beam that is also used during communication, $A_R = A_B$ may be adequate, similar to Fig. 4 as we only need to illuminate each position once. This would mean that the number of scan steps can be lower than for the same system with a smaller laser beam. However, we benchmark for $A_R = A_D$. In Gaussian beams, the irradiance gradually decreases from the center towards the edges. If the system is not perfectly aligned, the received power drops so it becomes challenging to satisfy the minimum energy per bit requirement. Also, even for uniform beams, it is preferred to align the detector with the center of the beam to avoid potential imbalances in the system. For example, if the laser beam vibrates due to device motions, it is best to place the detector in the middle, to minimize the chance that it falls out of the beam. Secondly, for this case, for every point (thus for every step in the scanning) we need to send a full address packet including overhead such as a synchronisation header and error correction. Fig. 5 shows that to ensure adequate received energy per bit, a wide beam requires a dramatic reduction in modulation speeds that counter-productively reduces scan speed. It outweighs the number of bits per position, therefore System 1 is slower than System 2.

2) System 2: The second approach makes the beam size smaller (ideally to $A_B = A_D$), which would boost the energy per bit. For System 2, with the same resolution ($A_R = A_D$), we have the same problem as for discrete search, we have to use full addresses with a sync header. During a continuous scan, the receiver sees packet boundaries that are random with respect to the time interval during which the detector is illuminated. Every location needs at least two full packet intervals to ensure that it can always receive at least one complete packet (Eqn. 10). Therefore, the number of bits that are sent per position is greater than in System 1. We plot

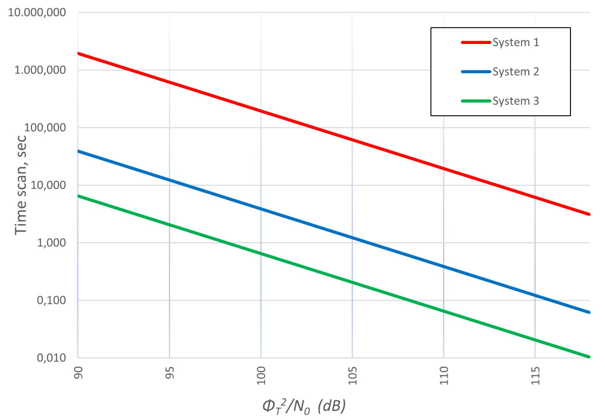

Fig. 5. Performance of 2 packetized addressing systems for beam searching versus Φ_T^2/N_0 using OOK, compared to LFSR addressing.

$$T_{scan} = 2\left(2\left(\log_2 \frac{A_C}{A_R} + N_h\right)\right) \frac{A_C}{A_R} \frac{A_B^2}{A_D^2} \frac{\kappa \Gamma N_0}{\eta_R^2 \Phi_T^2}. \tag{10}$$

Fig. 5 shows that smaller beam size has more impact because of the differences in the bit rate between the two approaches. Hence, System 2 is faster than System 1. There are also variants of System 1 and System 2 that improve search time significantly. The idea lies in the ability of the system to zoom. In fact, if only a single counter station is known to be present, further optimization of System 1 and 2 can be done by gradually zooming in on the target. For instance, in a two-step approach, the first step can be rough, i.e., a wide beam search to locate the approximate position, while the second step localizes the detector with high precision. Such a zooming system is beyond the scope of this paper but will be described in our later work.

V. Address coding by LFSR

Systems 1 and 2 use discrete addresses, as in Fig. 4, which need a sync header and some cyclic redundancy checks (CRC) or other error correction code which would further increase search time.

As an alternative System 3, we propose a coding scheme to embed direction addresses that is more efficient than creating data packets. The idea is to emit a pseudo-random sequence and to omit headers and sync words.

Linear-feedback shift registers (LFSRs) are characterized by the feature that by knowing a small portion of the sequence, namely the number of bits that equals the length L of the LFSR, uniquely identifies the position as it shown in Fig. 6. For this case, an LFSR of length L has a period of $2^L - 1$, thus it can address a little less than 2^L positions in L bits [6]. Any L bits in the sequence, e.g. bits at positions $l, l+1, ..., l+L-1$, form one address and when shifting over one position to $l+1, l+2, ..., l+L$, these L bits form the next address, while as many as $L-1$ bits overlap with the previous address. Thus, instead of having to transmit $\log_2(A_C/A_R) + N_h$ extra bits for one more address, LFSR–coded addresses only need a single bit extra for every next address. Fig. 7 shows that for such encoding scheme, the size of the beam should be L^2 bigger than the size of the detector. Then beam can move forward after sending 1 bit. The other way is that the beam can move forward to the next position after sending L bits. Thus, in (10) instead of the full address, we only need to send L bits as we can retrieve its position in the sequence.

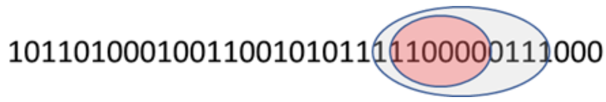

Fig. 6. Addressing by taking a snippet from an LFSR sequence, as considered in System 3. Red: minimum required number of bits for unique ID. (6 in this example) Green: example of a fault tolerant capture of an address

Evidently, the transmitter and the receiver must share the knowledge of the LFSR polynomial. Error correction comes for free: if more than L bits are received, it is possible to use the excess bits for error correction because these extra bits have to adhere to the feedback polynomial of the LFSR. This system can use a continuous scanning swipe. Fig. 7 further explains the area in which a unique address is found, while a beam is being swiped at high speed across the coverage area. System 3 uses this option and is seen to scan much faster than previously considered systems.

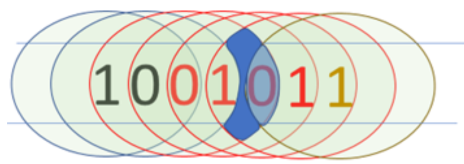

Fig. 7. Swiping beam progressing along the X-axis (position). The circles indicate the beam area at the start of the corresponding symbol. Address symbols are indicated in the center of each circle. A detector positioned in the light-blue area receives the red colored symbols 0101. Both 010 and 101 are unique addresses in the long LFSR sequence. A detector in the dark blue area receives 010, which still gives a unique position in the sequence.

Fig. 8 shows that it is possible to scan two orders of magnitude faster by using an LFSR code than with the use of discrete addresses. Of course this gain highly depends on the number of bits per discrete address and on the effectiveness of the header, and on how the resolution is handled in two dimensions. Nonetheless, it is anyhow significantly faster than System 2. This is particularly attractive if high bandwidths can be supported by the detector circuit. The LFSR addressing is also particularly effective if the desired resolution is smaller than the beam width.

As we rely on the binary properties of LFSRs, as we need synchronisation from the data itself, and as we want to avoid the need to track signal level variations, we use Manchester encoded data that has a rate 1/2.

VI. Further system considerations

After the laser beam from the transmitter hits the receiver, it reports the signal back by means of a lower–rate feedback

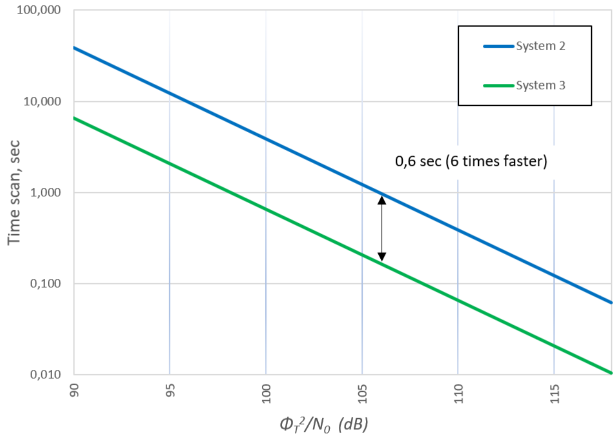

Fig. 8. Scan time for systems with a narrow beam as a function of Φ_T^2/N_0. Comparison of using a LFSR code for scan searching compared to using discrete addresses in data packets.

channel. As there is no prior information on the position of either transmitter or the receiver, it is preferable to use a wide beam for the feedback channel to cover all possible positions of the transmitter. Therefore, we can use both LEDs or lasers for this as it is not required to have a high bit rate to transmit an address back. The lack of information on the location of the transmitter means that a wide beam can come from any angle. Thus the detector on the transmitter side also needs to have a wide field of view (FoV). In photodetector designs, there are two trade-off that plays an important role in the design of the optical receiver: area versus bandwidth and gain versus FoV [7]. There are a couple of proposals in the literature to increase the FoV of the detector. In [8] it was proposed to use a two-dimensional matrix of photodetectors to increase the FoV without compensating for the bandwidth as there is an area-bandwidth trade-off. Such system proved to be capable of supporting > 1 Gb/s transmission, however, the penalty in signal strength was not reported. In [9] authors have proposed a design of a high-speed angle diversity receiver (ADR) that tackles the optimization of configuration of the receiver bandwidth and FoV. The noise versus signal-gain is evaluated in [10]. It appeared that matrix circuit layout may be advantageous for bandwidth but at the cost of sensitivity. Moreover, the size of the detector may be optimized, as in [11].

VII. Conclusions

In optical wireless communication, widening the search beam does not necessarily accelerate the scan time as it disproportionately reduces the energy per bit. The electrical energy per bit is proportional to the symbol duration and to the square of the optical power that falls on the detector. Thus, increasing beam size reduces the received signal strength to a much larger extent than radio communication. We learn from the law of conservation of energy that in free space the received optical or electromagnetic power reduces proportionally with the beam area.

We investigate this by considering systems that are also limited by Additive White Gaussian Noise in the receiver. In fact, in optical systems with a photodiode, the received signal strength declines proportionally to the square of the beam area. This paper studied the impact on the search time.

We developed a novel and efficient method for encoding the angular direction of the steering device to ensure a fast and error-free search for establishing a connection for laser-based optical wireless communication systems. For our example, the use of an LFSR speeds up scan time up by an order of magnitude compared to methods that require sending discrete addresses. As the receiver knows the polynomial of the LFSR sequence, additionally received bits outside the main address data can be used for error correction which saves even more time compared to approaches using packet-based addressing.

VIII. Acknowledgment

The performance analysis conducted in the paper was partly funded by the Netherlands NWO project ”FREE” Photonic Superhighways.

References

[1] Cho, S.-R., Lee, K., Kye, M., and Lee, C.-H., “Cost-effective auto-alignment method for indoor optical wireless communication,” in [*Asia Communications and Photonics Conference*], *Asia Communications and Photonics Conference* , M3F.6, Optica Publishing Group (2017).

[2] Wang, K., Nirmalathas, A., Lim, C., and Skafidas, E., “4 × 12.5 gb/s wdm optical wireless communication system for indoor applications,” *Journal of Lightwave Technology* **29**(13), 1988–1996 (2011).

[3] Linnartz, J.-P., Feri, L., Yang, H., Colak, S., and Schenk, T., “Communications and sensing of illumination contributions in a power led lighting system,” *IEEE International Conference on Communications* , 5396–5400 (01 2008).

[4] Mardanikorani, S., Deng, X., and Linnartz, J.-P. M. G., “Optimization and comparison of m-pam and optical ofdm modulation for optical wireless communication,” *IEEE Open Journal of the Communications Society* **1**, 1721–1737 (2020).

[5] Linnartz, J.-P. M. G., Hoelen, C., van Voorthuisen, P., Cunha, T. E. B., and Tao, H., “LED assessment based on an improved quality factor for LiFi communication,” in [*Light-Emitting Devices, Materials, and Applications XXVI*], Kim, J. K., Krames, M. R., and Strassburg, M., eds., **12022**, 120220F, International Society for Optics and Photonics, SPIE (2022).

[6] Dunn, W. L. and Shultis, J. K., “Chapter 3 - pseudorandom number generators,” in [*Exploring Monte Carlo Methods (Second Edition)*], Dunn, W. L. and Shultis, J. K., eds., 55–110, Elsevier, second edition ed. (2023).

[7] Soltani, M. D., Kazemi, H., Sarbazi, E., Haas, H., and Safari, M., “Optimal imaging receiver design for high-speed mobile optical wireless communications,” in [*2022 IEEE International Conference on Communications Workshops (ICC Workshops)*], 01–06 (2022).

[8] Koonen, T., Mekonnen, K., Huijskens, F., Cao, Z., and Tangdiongga, E., “Novel broadband owc receiver with large aperture and wide field-of-view,” in [*2020 European Conference on Optical Communications (ECOC)*], 1–4 (2020).

[9] Sarbazi, E., Kazemi, H., Crisp, M., El-Gorashi, T., Elmirghani, J., Penty, R., White, I., Safari, M., and Haas, H., “Design and optimisation of high-speed receivers for 6g optical wireless networks,” (2022).

[10] Liu, X., Linnartz, J.-P. M. G., and Arulandu, A. M. K. K., “Response of a matrix circuit of photodiodes with a common transimpedance amplifier in optical wireless communication,” (2023). IEEE Wireless Communications and Networking Conference (WCNC) ; Conference date: 26–29 March 2023, Glasgow, Scotland, UK.

[11] Azarkh, L., Liu, X., and Linnartz, J.-P., “Optimal detector size for optical wireless communication links with wide coverage,” (2022). 4th Optical Wireless Communication Conference, OWCC 2022, OWCC 2022 ; Conference date: 10-11-2022 Through 10-11-2022.

The influence of Bivariate Empirical Mode Decomposition parameters on AI-based Automatic Modulation Recognition accuracy

Alexander Gros
Electromagnetism and Telecommunications Department
Faculty of Engineering UMONS
Mons, Belgium
alexander.gros@umons.ac.be

Véronique Moeyaert
Electromagnetism and Telecommunications Department
Faculty of Engineering UMONS
Mons, Belgium
veronique.moeyaert@umons.ac.be

Patrice Mégret
Electromagnetism and Telecommunications Department
Faculty of Engineering UMONS
Mons, Belgium
patrice.megret@umons.ac.be

***Abstract*—On the one hand, the AMR (Automatic Modulation Recognition) realm has recently shown an increase of interest, particularly as an application for monitoring the physical layer of wireless transmissions. It consists in determining the employed modulation type of a sensed Radio Frequency (RF) signal at a given time, space and frequency. Moreover, it is a key component of intelligent radio systems such as Cognitive Radios (CR) that are key devices for Massive IoT (MIoT), autonomous cars, drones, 5G, 6G, etc. On the other hand, Bivariate Empirical Mode Decomposition (BEMD) is a signal decomposition method that can distill signals into a finite number of Intrinsic Mode Functions (IMFs) through a process known as sifting. BEMD is specifically designed to decompose bivariate (e.g. complex) signals, such as complex IQ samples of telecommunication data time series. The IMFs in conjunction with an AI architecture permits modulation classification.**

This paper specifically focuses on the influence of BEMD parameters on component extraction, namely the number of applied sifts and projections. The impact of linear interpolation method vs cubic spline interpolation method is also presented.

***Index Terms*—automatic modulation recognition, AMR, automatic modulation classification, AMC, cognitive radio, bivariate empirical mode decomposition, parameters BEMD, decomposition, convolutional neural networks, CNN**

I. Introduction

A. Context

The classification of modulation schemes traditionally involves two main approaches: the decision theoretic approach and the feature-based approach. However, with the advent of deep learning architectures [1], the domain of automatic modulation classification (AMC) has experienced a renaissance.

In [2], it has been proven that decomposing the signal using BEMD prior to introducing it into a convolutional neural network (CNN) type of AI architecture helps to extract interesting features and increases classification accuracy. In this paper, the impact of the BEMD decomposition parameters are analysed, namely the number of siftings, the number of projections and the type of interpolation used.

B. Data set

In order to classify modulations, an IQ database is required. The adopted dataset in this work is O'Shea's [3] RadioML2016a dataset. This dataset is a publicly available dataset consisting of complex-valued IQ samples, each being 128 samples long, and covering a wide range of radio signal modulations. The RadioML2016a dataset has been widely used in research on automatic modulation classification and machine learning for signal processing which enables thus performance comparison [4] [5]. It provides a valuable resource for researchers and developers working on the development of new algorithms for the classification of radio signals. The database contains single carrier modulations such as GFSK (Gaussian Frequency Shift Keying), 64QAM (Quadrature Amplitude Modulation), WBFM (WideBand Frequency Modulation) or QPSK (Quadrature Phase Shift Keying). There are a total 11 modulation schemes in the dataset and the signal to noise ratio in the dataset ranges from from -20dB to 18dB by steps of 2 dB, thus offering 20 different SNR values. This leads to a total of 220000 waveforms containing 128 samples each. Half of the dataset has been used for training, the other half for evaluation. It has to be noted that the dataset is not perfect [6] but that despite its flaws, it continues to be heavily used.

II. Decomposition method

A. BEMD (Rilling [7])

Bivariate empirical mode decomposition (BEMD) is a widely used method that extends the univariate EMD method to bivariate data, which is common in many contemporary data sets, including complex data. With the aim of extracting finer information to recover the modulation, such as amplitude and angular frequency, researchers have focused on developing approaches for decomposing bivariate or even multivariate data. In the context of telecommunications and software-defined radio, the main data series of interest are complex IQ samples, which makes BEMD a suitable approach.

The decomposition mechanism [8], also called sifting, consists in decomposing the input signal $s(t)$ into a finite number N of IMFs (Intrinsic Mode Functions) such that the signal can be expressed as:

$$s(t) = \sum_{i=1}^{N} \mathrm{IMF}_i(t) + r(t)$$

where $r(t)$ is the residue which may or may not have a linear trend.

Two important facts need to be highlighted in the BEMD method. Firstly, as presented in Fig. 1 displaying the decomposition steps, the mean is recurrently subtracted from the signal. Each of these subtractions are called sifts or siftings. The number of siftings can either be defined using a stopping criterion which is time expensive or simply predefined. Secondly, the method works by extracting rotating components using the mean of the envelope, which is like an enclosing tube around the signal. To create the lines that materialize the envelope, the signal is projected onto different directions or planes, resulting in a 2D signal on which the standard EMD methodology is applied. Four projections, for instance, could include extreme points in the top, bottom, left, and right directions. The rotating components can then be used to extract finer information, such as amplitude and angular frequency.

Algorithm 1 is the pseudocode representing one sifting process in the BEMD method.

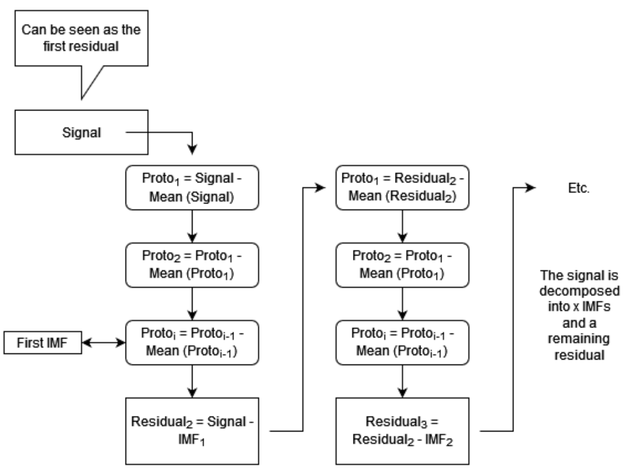

Fig. 1: Decomposition flow graph

Algorithm 1 The used BEMD algorithm from [7]

for $1 \leq k \leq N$ **do**

`Project the complex valued signal` $x(t)$ `on direction` φ_k `(Plane P)`

$\rightarrow p_{\varphi_k}(t) = \mathrm{Re}(e^{-i\varphi_k} x(t))$

`Extract the locations` $[t_j^k]$ `of the maxima of` $p_{\varphi_k}(t)$

`Interpolate the set` $(t_j^k, x(t_j^k))$ `to obtain the envelope curve in direction` $\varphi_k : e_{\varphi_k}(t)$

end for

`Compute the mean of all envelope curves` $m(t) = \frac{1}{N}\sum_k e_{\varphi_k}(t)$

`Subtract the mean`

B. Linear interpolation

In order to improve the overall computational speed, specifically regarding the envelope calculation, modifications have been made to the interpolation method. The interpolation step was found to be the most computationally intensive part of Algorithm 1 based on the results obtained from CPU profilers. Therefore, the cubic spline interpolation, which was previously used, has been replaced by a linear interpolation technique. Linear interpolation is a simple yet effective method for interpolation.

Fig. 2 shows how the signal's projections are used to recreate the envelope. The signal is depicted in blue and is a complex sinusoid $s(t) = sin(t) + jcos(t)$ The red line represents the mean of the envelope, it is calculated using the average of the projections. The other colors display the maxima and minima points of the signal that has been projected onto four planes at the angles 0, 45, 90 and 135 degrees.

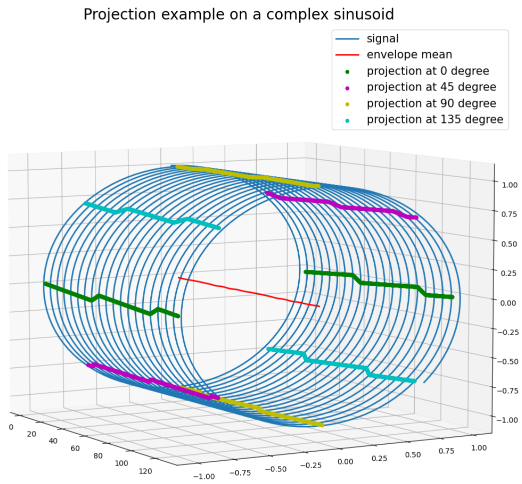

Fig. 2: Projection example for a complex sinusoid of amplitude 1V

Fig. 3, displays the real part of the first four intrinsic mode functions (IMFs) extracted from a Quadrature Phase-Shift

Keying (QPSK) modulation. These IMFs have been obtained through the BEMD method, utilizing four projections and three sifts. The difference between the plotted curves lies in the applied interpolation. Specifically, the blue curves were generated using cubic spline interpolation, whereas the orange curves were produced using linear interpolation. One can see that when using the cubic splines method, the number of remaining oscillations decreases faster with increasing IMF order.

III. Methodology

A. Artificial Intelligence architecture

Automated modulation classification (AMC) is the task of identifying the modulation type of a received signal at the receiver, which is typically a complex and challenging multi-class classification problem. To tackle this problem, deep-learning models are often employed. But designing such models involves consideration of various architectural parameters.

In this work, Convolutional Neural Networks (CNNs) were utilized for AMC. CNNs are a type of feed-forward neural network that has shown great success in processing and analyzing image and signal data. The main components of CNNs are its convolutional layers, which are responsible for convolving feature maps from previous layers with trainable kernels or filters. Additionally, the architecture includes fully connected or dense layers, which are Multilayer Perceptrons (MLPs) connected to the previous layer.

To improve the performance of the model, various techniques were used in this work, including ReLU activation maps (Rectified Linear Unit), padding and dropout layers. A flatten layer is used between the CNN and the dense layers. However, no pooling was employed, as the height of the data is small, and pooling could result in information loss due to averaging.

The corresponding convolutional layers (named conv1 and conv2) for this model have filter sizes of 1x3 for conv1 and 2x3 for conv2. The final dense layer has a size of 11, corresponding to the number of possible modulations, and includes a softmax activation layer for classification. The used CNN configuration is depicted in Fig. 5. The CNN architecture image have been created using PlotNeuralNet [9]. In Fig. 4 the best working input shape extracted from [2] is showed. The input shape has a height of two, containing the real (I) and the imaginary (Q) parts. The length is the number of samples (128) and the channels or depth is created with the extracted IMFs.

B. Information flow

The methodology's overall structure is illustrated in Fig. 6. The incoming Complex IQ data received by the receiver is subjected to a decomposition process using the Bidimensional Empirical Mode Decomposition (BEMD) method, with various parameters as mentioned in the beginning of the text. The extracted IMFs are then introduced to the CNN architecture which is trained to classify the used modulation type.

IV. Results

A. Parameters

The investigated parameters are the number of siftings for IMF extraction, the number of projections as well as the type of applied interpolation. The main characteristics are the overall accuracy taking into account all modulations and for all signal to noise ratios. The needed decomposition time is also added. Table I shows the time needed for the decomposition and is given for 100000 time series of length 128 and in minutes unit. It has been extracted from the mean of two measurements.
Table I also shows the accuracy results extracted from the mean of three full trainings. The accuracy results need to be compared to the overall accuracy using the signals IQ values along, thus involving no decomposition. In this original case, the accuracy is of 51.8 %. The calculations have been performed on an Intel SkyLake 2.60 GHz CPU on a high performance computing (HPC) cluster.

TABLE I: Overall accuracy depending on decomposition parameters

interpolation	siftings	projections	accuracy %	approx time (min)
cubic	3	4	53,86	84
		16	54,05	310
		64	53,67	1012
	10	4	53,96	269
		16	53,94	907
		64	53,76	3917
linear	3	4	51,92	39
		16	52,93	138
		64	53,71	676
	10	4	50,73	134
		16	50,61	530
		64	50,86	2302

B. Discussion

The assumption made to begin this work was that increasing the number of siftings and projections would give more refined intrinsic mode functions, increasing therefore the quality of the AI architectures input, and thus the classification accuracy.

This work shows that this is not the case and that these parameters have very little effects on the overall accuracy of the classifier.
This might be an unfavorable result in the sense that we can not improve the results considerably by refining the decomposition. However, it also means that it is not necessary to use high numbers of projections and siftings that increase the decomposition times drastically in order to get good results.

Regarding the complexity of the BEMD decomposition, it has been analysed in [10], [11] and [2]. Those references indicate that complexity can be simplified into into

$$P\, S\, n \log_2 n = \mathcal{O}(n \log n)$$

in which P represents the number of projections, S the number of siftings and n the length of the data.

Table I confirms this trend as the decomposition times are proportional to the number of applied projections and siftings.

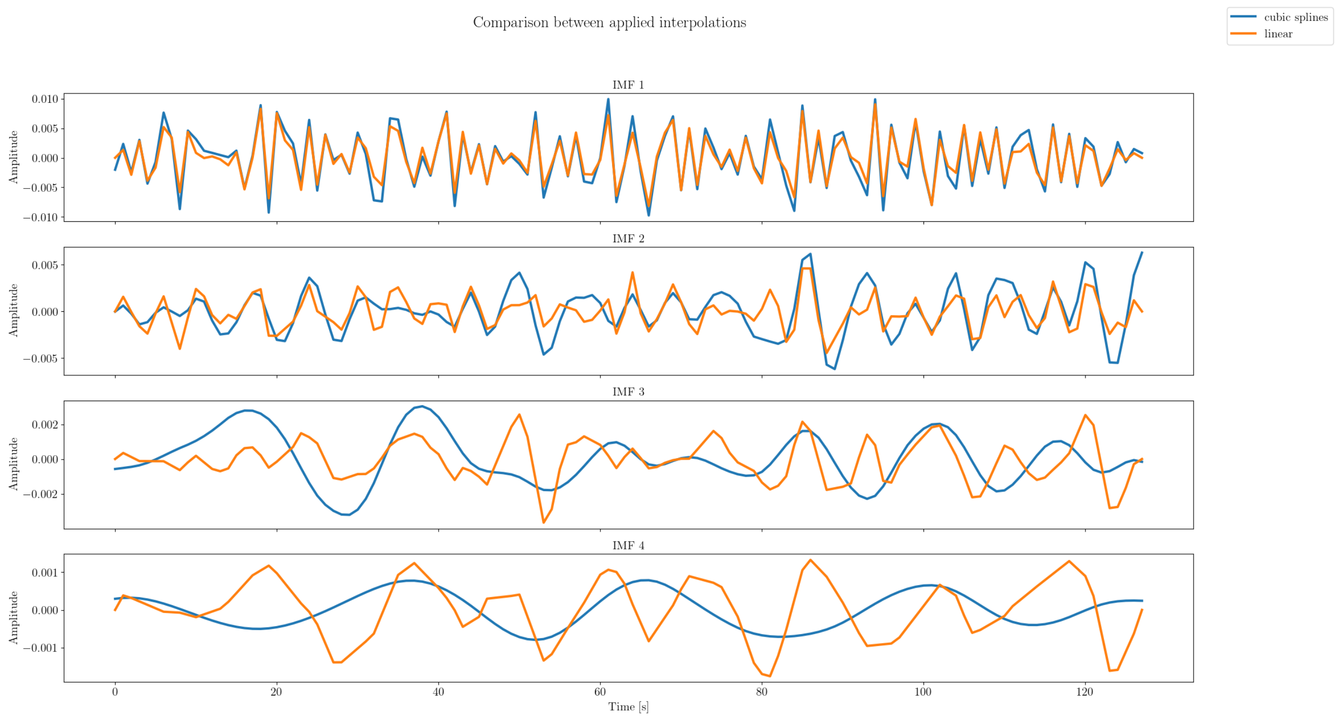

Fig. 3: Real part of the first four IMFs extracted from a QPSK modulation. In blue using a cubic spline and in orange using linear interpolation

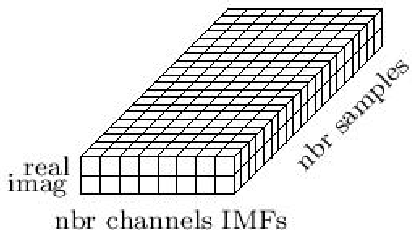

Fig. 4: 3D data shape, IMFs are stored in channels

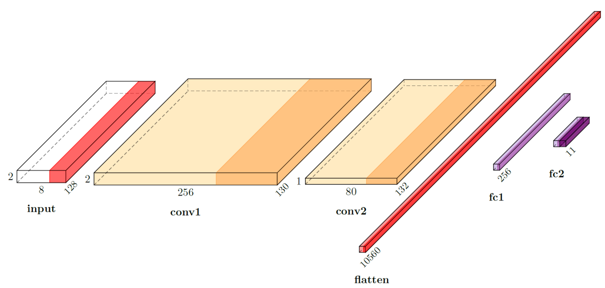

Fig. 5: CNN architecture applied in the case of a 3D data shape input

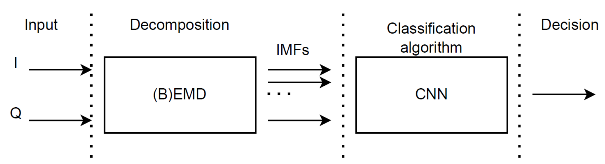

Fig. 6: Information flow

Also, for the same parameters, using a linear interpolation divides by two the required computation time.

Despite its potential benefits, linear interpolation does not result in a noticeable improvement in processing time compared to cubic spline interpolation, for a given threshold of classification accuracy. In practice, to achieve the same level of accuracy as cubic spline interpolation, it is necessary to increase the number of projections when using linear interpolation, which ultimately eliminates any potential time advantage.

Moreover, it has been found out that using linear interpolation increases the number of extracted IMFs.

V. Conclusion

Our results, as shown in Table 1, indicate that increasing the number of sifts and projections does not significantly affect the output accuracy of the classifier. This is an encouraging conclusion as it suggests that additional computation time is not needed to improve classification accuracy.

Upon analyzing the trade-off between decomposition time and classification accuracy, it is not recommended to utilize linear interpolation for envelope estimation in this specific use case. The reason for this is that linear interpolation does not provide sufficient accuracy compared to other methods of interpolation. Therefore, the accuracy of the classification results may be compromised if linear interpolation is employed for envelope estimation.

VI. Acknowledgement

This work is supported by the Wallonia Region research project CyberExcellence, n° 2110186.

Computational resources have been provided by the Consortium des Équipements de Calcul Intensif (CÉCI), funded by the Fonds de la Recherche Scientifique de Belgique (F.R.S.-FNRS) under Grant No. 2.5020.11 and by the Walloon Region.

References

[1] Yann LeCun, Y. Bengio, and Geoffrey Hinton. Deep learning. *Nature*, 521:436–44, 05 2015.

[2] Alexander Gros, Veronique Moeyaert, and Patrice Megret. Joint use of bivariate empirical mode decomposition and convolutional neural networks for automatic modulation recognition. In *2022 IEEE 33rd Annual International Symposium on Personal, Indoor and Mobile Radio Communications (PIMRC)*, pages 957–962, 2022.

[3] Timothy O'Shea and Nathan West. Radio machine learning dataset generation with gnu radio. *Proceedings of the GNU Radio Conference*, 1(1), 2016.

[4] Timothy James O'Shea, Tamoghna Roy, and T. Charles Clancy. Over-the-air deep learning based radio signal classification. *IEEE Journal of Selected Topics in Signal Processing*, 12(1):168–179, 2018.

[5] Sreeraj Rajendran, Wannes Meert, Domenico Giustiniano, Vincent Lenders, and Sofie Pollin. Deep learning models for wireless signal classification with distributed low-cost spectrum sensors. *IEEE Transactions on Cognitive Communications and Networking*, 4(3):433–445, 2018.

[6] Chad Spooner. An analysis of deepsig's 2016.10a data set. https://cyclostationary.blog/2020/04/29/all-bpsk-signals/. Accessed: 14.04.2022.

[7] Gabriel Rilling, Patrick Flandrin, Paulo Goncalves, and Jonathan M. Lilly. Bivariate empirical mode decomposition. *IEEE Signal Processing Letters*, 14(12):936–939, 2007.

[8] Norden Huang, Zheng Shen, Steven Long, M.L.C. Wu, Hsing Shih, Quanan Zheng, Nai-Chyuan Yen, Chi-Chao Tung, and Henry Liu. The empirical mode decomposition and the hilbert spectrum for nonlinear and non-stationary time series analysis. *Proceedings of the Royal Society of London. Series A: Mathematical, Physical and Engineering Sciences*, 454:903–995, 03 1998.

[9] Haris Iqbal. Harisiqbal88/plotneuralnet v1.0.0, December 2018.

[10] Yung-Hung Wang, Chien-Hung Yeh, Hsu-Wen Vincent Young, Kun Hu, and Men-Tzung Lo. On the computational complexity of the empirical mode decomposition algorithm. *Physica A: Statistical Mechanics and its Applications*, 400:159–167, 2014.

[11] Julien Fleureau, Amar Kachenoura, Jean-Claude Nunes, Laurent Albera, and Lotfi Senhadji. 3A-EMD: A Generalized Approach for Monovariate and Multivariate EMD. In *Information Sciences, Signal Processing and their Applications*, pages 300 – 303, Kuala Lumpur, Malaysia, May 2010.

RF Energy Harvester Circuits Supplied with Multi-sine Signals

Jarne Van Mulders, Chesney Buyle, Lieven De Strycker, Liesbet Van der Perre

KU Leuven, ESAT-WaveCore, Ghent Technology Campus
B-9000 Ghent, Belgium
jarne.vanmulders@kuleuven.be

***Abstract*—Radio frequency (RF) harvesting is showed to be a feasible technique to power energy neutral devices, providing a flexible solution to exchange small amounts of energy. The rectifier, used to convert RF to direct current (DC), introduces non-linearities, degrading the efficiency of the RF harvester. Different techniques are studied in literature to address this challenge, e.g., by using high peak-to-average power ratio (PAPR) signals. This research presents several *PySpice* rectifier models to evaluate the efficiency of different signal waveforms and RF harvester architectures. In this work, these models are utilized to assess the energy-efficiency gain of high PAPR signals with respect to single tone signals. As resulted from this work, we concluded that the gains of high PAPR signals depend strongly on the rectifier circuit, even having an adverse effect in case of a voltage doubler.**

Originally, a lot of attention has been spent on the improvement of the power conversion efficiency of rectifier circuits in order to increase the overall harvesting efficiency. However, recently, it has been shown that waveform design also affects the energy harvester efficiency [1]–[3]. The RF-to-DC efficiency of the harvester can be improved by waveform types with high peak-to-average power ratio (PAPR) signals. As the term explains, the signal power level will fluctuate and peaks of higher radiated power will occur periodically. At non-peak times, the transmitted power is significantly lower than the average radiated power. The reason why this method is being studied, is due to the restrictions in radiated power. Searching for techniques where the average radiated power of the transmitted signals remains the same, yet causes higher efficiency gains in the harvester, is therefore worth considering. In this study, the harvester performance supplied with a single tone signal is compared with multi-sine signals. To make a fair comparison, the generated waveforms should have the same average power than a single tone signal. While many research papers have shown that the RF-to-DC efficiency can be increased by applying high PAPR signals, it turns out that these signals are not always beneficial for the harvester performance. [4] has described this phenomenon more in detail specifically for a voltage doubler rectifier.

In this comparative study, the full harvester efficiency is considered, including matching losses and consequently reflections. Due to the nonlinear model of a diode, it is challenging to match a rectifier circuit. Usually, the input impedance is determined by simulations or measured with a vector network analyzer (VNA). Based on the obtained complex input impedance and using the Smith chart, an appropriate matching network is proposed. The nonlinear model of the diode causes an additional input power dependency, in addition to the frequency dependency. This additional dependency means that the matching circuit cannot ensure a perfect match over the entire input power range. A matching circuit between the antenna impedance of typically $50\,\Omega$ and the rectifier circuit is proposed for each considered harvester. Unfortunately, this matching circuit provides only one optimal situation with small losses and reflections for a well-defined frequency and input power level. In practise, reflections will cause additional losses due to a fluctuating input power. This study considers two rectifier circuits constructed with a single diode rectifier and a voltage doubler rectifier.

The results show that for a single diode rectifier, the power conversion efficiency increases with an increasing number of frequency components. However, with a voltage doubler, the opposite effect is stated. It appears that the voltage doubler performance decreases with increasing frequency components in the multi-sine signal. This latter rectifier circuit no longer works as a true doubler. Furthermore, the simulations show that efficiency gains can be validated with low complex PySpice scripts. Implementation and design effort can be improved by first modelling and simulating the desired rectifier circuit with corresponding matching circuits, and then supply them with the desired waveform input signals. Sweeps over the entire input power range (e.g. $-20\,\mathrm{dBm}$ up to $10\,\mathrm{dBm}$) for multiple input signals provides a good estimate of the potential efficiency gains.

The REINDEER project has received funding from the European Union's Horizon 2020 research and innovation programme under grant agreement No. 101013425.

References

[1] M. S. Trotter, J. D. Griffin, and G. D. Durgin, "Power-optimized waveforms for improving the range and reliability of rfid systems," in *2009 IEEE International Conference on RFID*, 2009, pp. 80–87.

[2] F. Bolos, J. Blanco, A. Collado, and A. Georgiadis, "Rf energy harvesting from multi-tone and digitally modulated signals," *IEEE Transactions on Microwave Theory and Techniques*, vol. 64, no. 6, pp. 1918–1927, 2016.

[3] M. Rajabi, N. Pan, S. Pollin, and D. Schreurs, "Impact of multisine excitation design on rectifier performance," in *2016 46th European Microwave Conference (EuMC)*, 2016, pp. 1151–1154.

[4] N. Shariati, J. R. Scott, D. Schreurs, and K. Ghorbani, "Multitone excitation analysis in rf energy harvesters—considerations and limitations," *IEEE Internet of Things Journal*, vol. 5, no. 4, pp. 2804–2816, 2018.

Gilbert-Varshamov inspired lower bound on the maximal cardinality of indel and substitution correcting codes

Ward J. P. Spee
Delft University of Technology
Delft, The Netherlands
W.J.P.Spee@student.tudelft.nl

Jos H. Weber
Delft University of Technology
Delft, The Netherlands
J.H.Weber@tudelft.nl

***Abstract*—Recent advances in DNA data storage and racetrack memory have attracted renewed attention towards deletion, insertion and substitution correcting codes. Compared to codes aimed at correcting either substitution errors or deletion and insertion (indel) errors, the understanding of codes that correct combinations of substitution and indel errors lags behind. In this paper, we focus on the maximal size of q-ary t-indel s-substitution correcting codes. In particular, our main contribution is a Gilbert-Varshamov inspired lower bound on this size. Moreover, we study the asymptotic behaviour of this bound.**

***Index Terms*—Error correcting codes, Gilbert-Varshamov bound, indels, substitutions.**

I. Introduction

CODING techniques for correcting deletion, insertion and substitution errors have attracted increasing attention recently due to their applications in DNA data storage [1], [2] and racetrack memory [3], [4]. Codes that correct either substitution errors or deletion and insertion errors have been extensively studied in literature. In contrast, the simultaneous correction of combinations of these three error types is less understood. A central problem is to determine the maximal size of codes that correct combinations of deletion, insertion, and substitution errors.

Classical error correcting codes aimed at correcting substitution errors have been well-studied for over 75 years [5]. A fundamental result in this area is the well-known Gilbert-Varshamov bound [6], [7] which asserts the existence of a q-ary s-substitution correcting code with codewords of length n and with a code size of at least

$$\frac{q^n}{\sum_{i=0}^{2s}\binom{n}{i}(q-1)^i}.$$

This statement was initially proven by Gilbert [6] for binary codes, and later independently by Varshamov [7]. Subsequently, the bound has been improved and generalized in various settings. An overview of these improvements in the context of substitution correcting codes is given in [8].

In a seminal paper [9], Levenshtein initiated the study of deletion and insertion (indel) correcting codes. He showed that a code that is able to correct t deletions (or insertions) is able to correct any t' deletions and t'' insertions, whenever $t'+t'' \leq t$. In other words, a t-deletion (insertion) correcting code is also a t-indel correcting code. This property shows the indifference between correcting deletions and insertions, which warrants the terminology of t-indel correcting codes. Inspired by the Gilbert-Varshamov bound and the work of Tolhuizen [10], a lower bound on the maximal size of t-indel correcting codes was given in [11]. Multiple bounds that improve upon this result were presented in [12] and [13].

In comparison with either substitution correcting codes or indel correcting codes, non-asymptotic lower bounds on the maximal cardinality of t-indel s-substitution correcting codes have been studied to a lesser degree in literature. Several t-indel s-substitution correcting codes have been constructed, e.g. in [14], [15], which naturally imply non-asymptotic lower bounds on the maximal size of these codes. In [9], Levenshtein also showed two asymptotic bounds which imply that a binary t-indel s-substitution correcting code of maximal size has an asymptotic redundancy between $(t+s)\log_2(n)$ and $2(t+s)\log_2(n)+o(\log_2(n))$. Moreover, note that each $(t+2s)$-indel correcting codes is also a t-indel s-substitution correcting code, because a substitution can be seen as a deletion followed by an insertion. Hence, lower bounds on the maximum size of $(t+2s)$-indel correcting codes imply lower bounds for t-indel s-substitution correcting codes as well.

The last observation that a $(t+2s)$-indel correcting code is also a t-indel s-substitution correcting code might raise the preliminary question whether it is superfluous to consider the correction of substitutions separately. However, there are two arguments in favor of separating indel correction from substitution correcting. First, it was recognized by Song *et al.* [14] that $(t+2s)$-indel correcting codes are not necessarily optimal within the set of t-indel s-substitution correcting codes in terms of redundancy[1]. Secondly, in applications such as DNA data storage, the error rates of indels and substitutions differ [2]. Therefore, it is sensible to bound the number indels and substitutions by different parameters.

[1]For instance, the single-substitution correcting binary Hamming code with words of length 7 has size 16 [16]. In contrast, in [17, Thrm. 1] it was shown that a binary two-indel correcting code has a maximal size of at most 11.

In this paper, we study the maximal size of t-indel s-substitution correcting codes on a q-ary alphabet. In particular, our contribution is a Gilbert-Varshamov inspired lower bound on this size. Moreover, we will prove that this bound implies that a q-ary t-indel s-substitution correcting code of maximal size has an asymptotic redundancy of at most $2(t+s)\log_q(n)+o(\log(n))$. This extends Levenshtein's upper bound on the asymptotic redundancy to q-ary codes.

The organisation of this paper is as follows. In Section II, notation, terminology and several prior results are discussed. Next, a non-asymptotic lower bound inspired by the Gilbert-Varshamov bound is derived in Section III. Lastly, the asymptotic behaviour of this bound is studied in Section IV.

II. Definitions and preliminaries

For a finite set S, denote the cardinality of S by $|S|$. Consider the alphabet with $q \geq 2$ symbols given by $\mathcal{B}_q := \{0,1,...,q-1\}$. The set of q-ary words (i.e., vectors) of length n with symbols from $\mathcal{B}_q$ is denoted by $\mathcal{B}_q(n) := \{0,1,...,q-1\}^n$. A non-empty subset $\mathcal{C} \subseteq \mathcal{B}_q(n)$ is called a code and the elements of a code are called codewords. A code can be capable of correcting errors by ensuring that the codewords of $\mathcal{C}$ are 'sufficiently different', so that after several errors have occurred the resulting word still 'resembles' the original codeword, but not any of the other codewords. This idea forms the basis for the following definition of an indel and substitution correcting code.

For integers $0 \leq t \leq n$ and $0 \leq s \leq n$, a code $\mathcal{C} \subseteq \mathcal{B}_q(n)$ is said to be a *t-indel s-substitution correcting code* if any q-ary word (not necessarily of length n) can be obtained from no more than one codeword by exactly t' deletions, t'' insertions and s or fewer substitutions, whenever $t'+t'' \leq t$. A 0-indel s-substitution correcting code is simply called an *s-substitution correcting code* and analogously a t-indel 0-substitution correcting code is called a *t-indel correcting code*.

By only using codewords for communicating information, the code gains error-correcting capabilities at the cost of introducing redundancy. In order to maximize the amount of information that can be transmitted using a code, we are interested in the maximal size of a q-ary t-indel s-substitution correcting code with codewords of length n, which we denote by $M_q(n,t,s)$. The (information) rate of a code $\mathcal{C}$ is defined by $\frac{1}{n}\log_q(|\mathcal{C}|)$ and the redundancy by $n - \log(|\mathcal{C}|)$.

Denote by $\mathcal{V}_{t',t'',s}(\mathbf{x})$ the set of words that can be reached from $\mathbf{x} \in \mathcal{B}_q(n)$ by means of exactly t' deletions, t'' insertions and at most s substitutions. Clearly, the q-ary words in the set $\mathcal{V}_{t',t'',s}(\mathbf{x})$ have length $n - t' + t''$. Moreover, we define $\mathcal{D}_t(\mathbf{x}) = \mathcal{V}_{t,0,0}(\mathbf{x})$, $\mathcal{I}_t(\mathbf{x}) = \mathcal{V}_{0,t,0}(\mathbf{x})$ and $\mathcal{S}_s(\mathbf{x}) = \mathcal{V}_{0,0,s}(\mathbf{x})$. These sets are highly related to t-indel s-substitution correcting codes, and allow for equivalent characterizations of these codes in terms of the set $\mathcal{V}_{t',t'',s}(\mathbf{x})$. The following lemma collects various equivalent characterizations from e.g., [14, Sec. II], [18, Lem. 2] and [19, Lem. 2].

Lemma 1. *Let $n \geq 1$, $q \geq 2$, $0 \leq t \leq n$ and $0 \leq s \leq n$ be integers, and let $\mathcal{C} \subseteq \mathcal{B}_q(n)$ be a code. Then, the following five statements are equivalent:*

1) *$\mathcal{C}$ is a t-indel s-substitution correcting code.*
2) *$\mathcal{V}_{t',t'',s}(\mathbf{c}_1) \cap \mathcal{V}_{t',t'',s}(\mathbf{c}_2) = \emptyset$ for all distinct codewords $\mathbf{c}_1, \mathbf{c}_2 \in \mathcal{C}$, and for all integers $t', t'' \geq 0$ such that $t'+t'' \leq t$.*
3) *$\mathcal{V}_{t,0,s}(\mathbf{c}_1) \cap \mathcal{V}_{t,0,s}(\mathbf{c}_2) = \emptyset$ for all distinct codewords $\mathbf{c}_1, \mathbf{c}_2 \in \mathcal{C}$.*
4) *$\mathcal{V}_{0,t,s}(\mathbf{c}_1) \cap \mathcal{V}_{0,t,s}(\mathbf{c}_2) = \emptyset$ for all distinct codewords $\mathbf{c}_1, \mathbf{c}_2 \in \mathcal{C}$.*
5) *$\mathbf{c}_2 \notin \mathcal{V}_{t,t,2s}(\mathbf{c}_1)$ for all distinct $\mathbf{c}_1, \mathbf{c}_2 \in \mathcal{C}$.*

For general parameters t', t'' and s, and words $\mathbf{x} \in \mathcal{B}_q(n)$ determining the cardinality of $\mathcal{V}_{t',t'',s}(\mathbf{x})$ is a non-trivial task [20]. In the highly specific case that $t' = t'' = 0$ it holds for each $\mathbf{x} \in \mathcal{B}_q(n)$ [5] that

$$|\mathcal{S}_s(\mathbf{x})| = \sum_{i=0}^{s} \binom{n}{i}(q-1)^i. \tag{1}$$

The quantity $S^s_{n,q} := \sum_{i=0}^{s}\binom{n}{i}(q-1)^i$ will be referred to as the size of the q-ary Hamming sphere of radius s. Moreover, it has been established [21] that

$$|\mathcal{I}_t(\mathbf{x})| = S^t_{n+t,q} = \sum_{i=0}^{t}\binom{n+t}{i}(q-1)^i. \tag{2}$$

Interestingly, the cardinalities of $\mathcal{S}_s(\mathbf{x})$ and $\mathcal{I}_t(\mathbf{x})$ depend on $\mathbf{x}$ only via the parameters n and q. In contrast, $|\mathcal{D}_t(\mathbf{x})|$ depends on the structure of the word $\mathbf{x}$ as well as the parameters n and q. To the best of authors' knowledge, an analytic formula of $|\mathcal{D}_t(\mathbf{x})|$ is not known for general t and therefore we must rely on bounds (see e.g., [9], [22], [23]). For $t \leq 5$, an analytic formula of $|\mathcal{D}_t(\mathbf{x})|$ has been provided in [24], but these expressions are rather involved for $t \geq 2$. Lastly, we mention that using the observation that $\mathbf{x} \in \mathcal{I}_t(\mathbf{y})$ if and only if $\mathbf{y} \in \mathcal{D}_t(\mathbf{x})$, it was shown in [11] that the average cardinality of $\mathcal{D}_t(\mathbf{x})$ is given by

$$\begin{aligned}\frac{1}{q^n}\sum_{\mathbf{x}\in\mathcal{B}_q(n)}|\mathcal{D}_t(\mathbf{x})| &= \frac{1}{q^n}\sum_{\mathbf{y}\in\mathcal{B}_q(n-t)}|\mathcal{I}_t(\mathbf{y})| \\ &\overset{(2)}{=} \frac{1}{q^t}\sum_{i=0}^{t}\binom{n}{i}(q-1)^i. \end{aligned}\tag{3}$$

III. Gilbert-Varshamov inspired lower bound

The well-known Gilbert-Varshamov lower bound for s-substitution correcting codes [6], [7] is given by

$$M_q(n,0,s) \geq \frac{q^n}{\sum_{i=0}^{2s}\binom{n}{i}(q-1)^i}. \tag{4}$$

This bound is commonly proven using a sphere-covering argument where the spheres are given by $\mathcal{S}_{2s}(\mathbf{c})$ centered around the codewords $\mathbf{c} \in \mathcal{C}$ (see e.g., [5, Thrm. 4.3]). In the case of substitutions, this proof is facilitated by the fact that these spheres are of equal size.

Tolhuizen [10] recognized that the Gilbert-Varshamov bound is also implied by Turán's theorem [25] from extremal graph theory. A particular consequence of the latter approach is that it easily generalizes to the case in which the spheres are not of equal size. For instance, this is the case for t-indel correcting codes when dealing with the spheres $\mathcal{V}_{t,t,0}(\mathbf{c})$. The approach from Tolhuizen was used by Levenshtein [11] to bound the maximal size of a t-indel correcting code from below. In particular, it was shown that

$$M_q(n,t,0) \geq \frac{q^{n+t}}{\left(\sum_{i=0}^{t}\binom{n}{i}(q-1)^i\right)^2}. \qquad (5)$$

For completeness, we mention that other Gilbert-Varshamov related lower bounds on $M_q(n,t,0)$ are given in [12], [13].

Next, it is a natural step to generalize the argument from Tolhuizen to t-indel s-substitution correcting codes.

Lemma 2. *Let $n \geq 1$, $q \geq 2$, $0 \leq t \leq n$ and $0 \leq s \leq n$ be integers. The following gives a lower bound on $M_q(n,t,s)$,*

$$M_q(n,t,s) \geq \frac{q^n}{\mathcal{V}^{avr}_{t,t,2s}}, \qquad (6)$$

where $\mathcal{V}^{avr}_{t,t,2s} := q^{-n}\sum_{\mathbf{x}\in\mathcal{B}_q(n)}|\mathcal{V}_{t,t,2s}(\mathbf{x})|$.

Proof. The idea of this proof is to translate the problem of finding a large code to the problem of finding a large clique[2]. This allows us to apply the argument from [10, Sec. II] to derive the desired lower bound on $M_q(n,t,s)$.

Define the undirected graph $G=(V,E)$ without loops or double edges as follows. Let $V=\mathcal{B}_q(n)$ be the set of nodes of G. Two distinct nodes $\mathbf{x}$ and $\mathbf{y}$ from V are joined by an edge in E if $\mathbf{x}\notin\mathcal{V}_{t,t,2s}(\mathbf{y})$. This is well-defined because it holds that $\mathbf{x}\notin\mathcal{V}_{t,t,2s}(\mathbf{y})$ if and only if $\mathbf{y}\notin\mathcal{V}_{t,t,2s}(\mathbf{x})$. Intuitively, the pairs of nodes that are connected by an edge can both be codewords in a t-indel s-substitution correcting code. The number of nodes equals $|V|=q^n$ and the number of edges is given by

$$\begin{aligned}
|E| &= \frac{1}{2}\sum_{\mathbf{x}\in V}(|V\setminus\mathcal{V}_{t,t,2s}(\mathbf{x})|)\\
&= \frac{1}{2}\sum_{\mathbf{x}\in V}(|V|-|\mathcal{V}_{t,t,2s}(\mathbf{x})|)\\
&= \frac{1}{2}q^{2n}-\frac{1}{2}\sum_{\mathbf{x}\in\mathcal{B}_q(n)}|\mathcal{V}_{t,t,2s}(\mathbf{x})|\\
&= \frac{1}{2}q^n(q^n-\mathcal{V}^{avr}_{t,t,2s}),
\end{aligned}$$

where the first equality follows from the fact that each $\mathbf{x}\in V$ has $|V\setminus\mathcal{V}_{t,t,2s}(\mathbf{x})|$ incident edges. Therefore, summing $|V\setminus\mathcal{V}_{t,t,2s}(\mathbf{x})|$ over all nodes in $\mathbf{x}\in V$ equals $2|E|$ since each edge is counted twice. Observe that from the definition of the edges in G and Lemma 1 it follows that a clique of size k in G corresponds to a t-indel s-substitution correcting code $\mathcal{C}$ of size k.

Using the cardinalities of V and E it follows from the argument in [10, Sec. II] that there exists a clique in G of size $\lceil\frac{q^n}{\mathcal{V}^{avr}_{t,t,2s}}\rceil$. For brevity, we do not repeat this argument here. In turn, this implies that there exists an equally large t-indel s-substitution correcting code, which concludes the proof. □

[2]A clique of a graph G is an induced subgraph that is complete, i.e., all pairs of vertices are connected by an edge.

In order to evaluate the lower bound in Lemma 2 the size of $\mathcal{V}_{t,t,2s}(\mathbf{x})$ averaged over all $\mathbf{x}\in\mathcal{B}_q(n)$ needs to be determined. To the best of the authors' knowledge, an analytic formula for $|\mathcal{V}_{t,t,2s}(\mathbf{x})|$ or $\mathcal{V}^{avr}_{t,t,2s}$ is not known for general parameters n,q,t and s. For this reason, we employ an upper bound on $\mathcal{V}^{avr}_{t,t,2s}$ to obtain an explicit result.

Theorem 3. *For integers $n\geq 1$, $q\geq 2$, $0\leq t\leq n$ and $0\leq s\leq n$, the following gives a lower bound on $M_q(n,t,s)$,*

$$M_q(n,t,s) \geq \frac{q^{n+t}}{\left(\sum\limits_{i=0}^{t}\binom{n}{i}(q-1)^i\right)^2\sum\limits_{i=0}^{2s}\binom{n-t}{i}(q-1)^i}. \qquad (7)$$

Proof. We claim that $\mathcal{V}^{avg}_{t,t,2s}$ can be upper bounded by

$$\frac{1}{q^t}\left(\sum_{i=0}^{t}\binom{n}{i}(q-1)^i\right)^2\sum_{i=0}^{2s}\binom{n-t}{i}(q-1)^i. \qquad (8)$$

In this case, the result of the theorem follows immediately from applying the upper bound to Lemma 2. Therefore, this proof is limited to proving this claim. In what follows, a superscript $^-$ will be used to denote a word in $\mathcal{B}_q(n-t)$, whereas an omission thereof is meant for words in $\mathcal{B}_q(n)$.

To this end, observe that each element in $\mathcal{V}_{t,t,2s}(\mathbf{x})$ can be reached from $\mathbf{x}\in\mathcal{B}_q(n)$ by first deleting precisely t symbols, followed by substituting at most $2s$ symbols and lastly inserting exactly t symbols. Hence, it follows that

$$|\mathcal{V}_{t,t,2s}(\mathbf{x})| \leq \sum_{\mathbf{y}^-\in\mathcal{D}_t(\mathbf{x})}\sum_{\mathbf{z}^-\in\mathcal{S}_{2s}(\mathbf{y}^-)}|\mathcal{I}_t(\mathbf{z}^-)|. \qquad (9)$$

In order to evaluate the right-hand side of this expression, recall from (1) and (2) that the cardinalities of the sets $\mathcal{I}_t(\mathbf{x}^-)$ and $\mathcal{S}_{2s}(\mathbf{x}^-)$ do not depend on the choice of $\mathbf{x}^-\in\mathcal{B}_q(n-t)$. Moreover, the cardinality of $\mathcal{D}_t(\mathbf{x})$ averaged over all $\mathbf{x}\in\mathcal{B}_q(n)$ was given in (3). By combining these results and carefully taking into account the lengths of the words, it follows that

$$\begin{aligned}
\mathcal{V}^{avg}_{t,t,2s} &= q^{-n}\sum_{\mathbf{x}\in\mathcal{B}_q(n)}|\mathcal{V}_{t,t,2s}(\mathbf{x})|\\
&\overset{(9)}{\leq} \frac{1}{q^n}\sum_{\mathbf{x}\in\mathcal{B}_q(n)}\sum_{\mathbf{y}^-\in\mathcal{D}_t(\mathbf{x})}\sum_{\mathbf{z}^-\in\mathcal{S}_{2s}(\mathbf{y}^-)}|\mathcal{I}_t(\mathbf{z}^-)|\\
&\overset{(2)}{=} \frac{1}{q^n}\sum_{\mathbf{x}\in\mathcal{B}_q(n)}\sum_{\mathbf{y}^-\in\mathcal{D}_t(\mathbf{x})}\sum_{\mathbf{z}^-\in\mathcal{S}_{2s}(\mathbf{y}^-)}S^t_{n,q}\\
&\overset{(1)}{=} \frac{1}{q^n}\sum_{\mathbf{x}\in\mathcal{B}_q(n)}\sum_{\mathbf{y}^-\in\mathcal{D}_t(\mathbf{x})}S^{2s}_{n-t,q}\cdot S^t_{n,q}\\
&= \frac{1}{q^n}\cdot S^t_{n,q}\cdot S^{2s}_{n-t,q}\cdot\sum_{\mathbf{x}\in\mathcal{B}_q(n)}|\mathcal{D}_t(\mathbf{x})|\\
&\overset{(3)}{=} \frac{1}{q^t}\cdot(S^t_{n,q})^2\cdot S^{2s}_{n-t,q}.
\end{aligned}$$

Note that the last expression is equivalent to (8), which proves the claim. □

Observe that the lower bounds (4) and (5) are special cases of the latter theorem, since they are recovered by setting $t = 0$ and $s = 0$, respectively. Obviously, the bound from Theorem 3 can be improved with the availability of exact expressions, or tighter bounds on $\mathcal{V}^{avg}_{t,t,2s}$.

IV. Asymptotic behaviour

In this section we discuss the asymptotic behaviour of Theorem 3 in two settings based on the dependency of t and s with respect to n.

First, consider the setting in which the parameters q, t and s are fixed, and we let n tend to infinity. In this setting, Levenshtein [9] showed two asymptotic bounds on $M_2(n,t,s)$ which imply that the asymptotic redundancy of a binary t-indel s-substitution correcting code of maximal size lies between $(t+s)\log_2(n)$ and $(2t+2s)\log_2(n)+o(\log_2(n))$. Here, we provide an alternative proof for the asymptotic upper bound and extend the result from binary to q-ary codes, by showing that it is implied by the non-asymptotic lower bound on $M_q(n,t,s)$ of Theorem 3.

Lemma 4. *Let $q \geq 2$ be an integer. For non-negative integers s and t such that $s+t \geq 1$, the following holds*

$$\limsup_{n\to\infty} \frac{n-\log_q(M_q(n,t,s))}{(2t+2s)\log_q(n)} \leq 1.$$

Proof. Theorem 3 states that

$$M_q(n,t,s) \geq \frac{q^{n+t}}{(S^t_{n,q})^2 \cdot S^{2s}_{n-t,q}}.$$

This implies that the redundancy of an optimal t-indel s-substitution correcting code is bounded by

$$n-\log_q(M_q(n,t,s)) \leq -t + 2\log_q(S^t_{n,q}) + \log_q(S^{2s}_{n-t,q}).$$

Note that for a fixed integer $k \geq 1$ it holds that $\binom{n}{k} = \frac{1}{k!}n^k + o(n^k)$. In turn, it follows that $S^s_{n,q} = \frac{(q-1)^s}{s!}n^s + o(n^s)$, and $\log_q(S^s_{n,q}) = s\log_q(n) + o(\log_q(n))$. By combining these observations we obtain

$$\limsup_{n\to\infty}\frac{n-\log_q(M_q(n,t,s))}{(2t+2s)\log_q(n)} \leq \limsup_{n\to\infty} \frac{-t+2\log_q(S^t_{n,q})+\log_q(S^{2s}_{n-t,q})}{(2t+2s)\log_q(n)} = 1,$$

as desired. □

The following statement is immediate from the previous lemma.

Corollary 5. *A maximal size t-indel s-substitution correcting code has an asymptotic redundancy of at most $(2t+2s)\log_q(n)+o(\log_q(n))$.*

Secondly, we consider the asymptotic regime in which $q \geq 2$ and $\tau,\sigma \in [0,1]$ are fixed and n tends to infinity. We set[3] $t = \tau n$, $s = \sigma n$. Define the asymptotic rate by

$$R_q(\tau,\sigma) := \liminf_{n\to\infty} \frac{1}{n}\log_q(M_q(n,\tau n,\sigma n)). \tag{10}$$

For $\sigma = 0$ and $\tau > 0$, bounds on $M_q(n,t,0)$ have been used to derive results on $R_q(\tau,0)$ in e.g., [11], [17], [26]. On the other hand, for $\tau = 0$ and $\sigma > 0$ a summary of several results on $R_q(0,\sigma)$ can be found in [5]. Here, we use Theorem 3 to derive a lower bound on $R_q(\tau,\sigma)$.

To this end, let $H_q(x) = x\log_q(q-1) - x\log_q(x) - (1-x)\log_q(1-x)$ on $[0, 1-\frac{1}{q}]$ with $H_q(0) = 0$ denote the q-ary entropy function. The extended q-ary entropy function is given by $H^*_q(x) = H_q(\min\{x, 1-\frac{1}{q}\})$ on $[0,\infty)$. Recall the following useful property of the extended q-ary entropy function [17], for each $\lambda \in (0,1)$ it holds that

$$\lim_{n\to\infty}\frac{1}{n}\log_q\left(\sum_{i=0}^{\lambda n}\binom{n}{i}(q-1)^i\right) = H^*_q(\lambda). \tag{11}$$

This property enables us to derive the following lower bound on $R_q(\tau,\sigma)$.

Lemma 6. *Let $q \geq 2$ be an integer and $\tau,\sigma \in (0,1)$. Then, it holds that*

$$R_q(\tau,\sigma) \geq 1+\tau-2H^*_q(\tau)-(1-\tau)H^*_q(\frac{2\sigma}{1-\tau}).$$

Proof. Theorem 3 states for $n \geq 1$ that

$$M_q(n,\tau n,\sigma n) \geq \frac{q^{n+\tau n}}{(S^{\tau n}_{n,q})^2\cdot S^{2\sigma n}_{n-\tau n,q}}.$$

By applying this bound to the rate function $R_q(\tau,\sigma)$, it readily follows that

$$\begin{aligned}
R_q(\tau,\sigma) \geq& \liminf_{n\to\infty}\frac{1}{n}\log_q\left(\frac{q^{n+\tau n}}{(S^{\tau n}_{n,q})^2\cdot S^{2\sigma n}_{n-\tau n,q}}\right)\\
=&1+\tau-2\liminf_{n\to\infty}\frac{1}{n}\log_q(S^{\tau n}_{n,q})\\
&-\liminf_{n\to\infty}\frac{1}{n}\log_q(S^{2\sigma n}_{n-\tau n,q})\\
=&1+\tau-2H^*_q(\tau)\\
&-\liminf_{n'\to\infty}\frac{1-\tau}{n'}\log_q(S^{\frac{2\sigma}{1-\tau}n'}_{n',q}) \qquad (12)\\
=&1+\tau-2H^*_q(\tau)\\
&-(1-\tau)H^*_q(\frac{2\sigma}{1-\tau}),
\end{aligned}$$

where we applied the change of variables $n' = n - \tau n$ in (12), and used (11) to evaluate the limit inferiori. □

[3]In what follows, we will be slightly imprecise by setting $t = \tau n$, $s = \sigma n$ which may not be integer-valued. However, in the asymptotic regime this does not change the over-all results.

V. Concluding remarks

In this paper, we have presented a non-asymptotic lower bound on the maximal cardinality of a t-indel s-substitution correcting code. In order to improve this lower bound, an interesting research challenge is to find an expression or tighter upper bound for the size of the set $\mathcal{V}_{t',t'',s}(\mathbf{x})$.

More generally, it could also be investigated whether the numerous existing lower and upper bounds on the maximum cardinality of either t-indel correcting codes or s-substitution correcting codes can be generalized to bounds on $M_q(n,t,s)$.

VI. Acknowledgments

We would like to thank Khaled Abdel-Ghaffar and Ludo Tolhuizen for their helpful comments which have greatly improved the quality of this paper.

References

[1] G. Church, Y. Gao, and S. Kosuri, "Next-generation digital information storage in DNA," *Science (New York, N.Y.)*, vol. 337, p. 1628, Sep. 2012.

[2] R. Heckel, G. Mikutis, and R. N. Grass, "A characterization of the DNA data storage channel," *Scientific Reports*, vol. 9, Jul. 2019.

[3] S. S. Parkin, M. Hayashi, and L. Thomas, "Magnetic domain-wall racetrack memory," *Science*, vol. 320, no. 5873, pp. 190–194, Apr. 2008.

[4] Y. M. Chee, H. M. Kiah, A. Vardy, V. K. Vu, and E. Yaakobi, "Coding for racetrack memories," *IEEE Transactions on Information Theory*, vol. 64, no. 11, pp. 7094–7112, 2018.

[5] R. Roth, *Introduction to Coding Theory*. Cambridge: Cambridge University Press, 2006.

[6] E. N. Gilbert, "A comparison of signalling alphabets," *The Bell System Technical Journal*, vol. 31, no. 3, pp. 504–522, May 1952.

[7] R. R. Varshamov, "Estimate of the number of signals in error correcting codes," *Doklady Akademii Nauk SSSR*, vol. 117, no. 5, pp. 739–741, Jun. 1957.

[8] J. Tao and A. Vardy, "Asymptotic improvement of the gilbert-varshamov bound on the size of binary codes," *IEEE Transactions on Information Theory*, vol. 50, no. 8, pp. 1655–1664, 2004.

[9] V. I. Levenshtein, "Binary codes capable of correcting deletions, insertions and reversals," *Soviet Physics Doklady*, vol. 10, no. 8, pp. 707–710, Feb. 1966, doklady Akademii Nauk SSSR, vol. 163, no. 4, pp. 845-848, Aug. 1965.

[10] L. Tolhuizen, "The generalized Gilbert-Varshamov bound is implied by Turan's theorem," *IEEE Transactions on Information Theory*, vol. 43, no. 5, pp. 1605–1606, Sep. 1997.

[11] V. I. Levenshtein, "Bounds for deletion/insertion correcting codes," *Proceedings IEEE International Symposium on Information Theory*, Jul. 2002.

[12] F. Sala, R. Gabrys, and L. Dolecek, "Gilbert-varshamov-like lower bounds for deletion-correcting codes," *2014 IEEE Information Theory Workshop (ITW 2014)*, pp. 147–151, Nov. 2014.

[13] F. Sala, R. Gabrys, C. Schoeny, and L. Dolecek, "Three novel combinatorial theorems for the insertion/deletion channel," *2015 IEEE International Symposium on Information Theory (ISIT)*, pp. 2702–2706, Jun. 2015.

[14] W. Song, N. Polyanskii, K. Cai, and X. He, "On multiple-deletion multiple-substitution correcting codes," *2021 IEEE International Symposium on Information Theory (ISIT)*, pp. 2655–2660, Sep. 2021.

[15] W. Song, N. Polyanskii, K. Cai, and X. He, "Systematic codes correcting multiple-deletion and multiple-substitution errors," *IEEE Transactions on Information Theory*, vol. 68, no. 10, pp. 6402–6416, 2022.

[16] R. W. Hamming, "Error detecting and error correcting codes," *Bell System Technical Journal*, vol. 29, no. 2, pp. 147–160, Apr. 1950.

[17] L. Tolhuizen, "Upper bounds on the size of insertion/deletion correcting codes," *Proceedings 8-th International Workshop on Algebraic and Combinatorial Coding Theory, Russia*, pp. 242–246, Sept. 2002.

[18] D. Cullina and N. Kiyavash, "An improvement to Levenshtein's upper bound on the cardinality of deletion correcting codes," *IEEE Transactions on Information Theory*, vol. 60, no. 7, pp. 3862–3870, 2014.

[19] I. Smagloy, L. Welter, A. Wachter-Zeh, and E. Yaakobi, "Single-deletion single-substitution correcting codes," *2020 IEEE International Symposium on Information Theory (ISIT)*, pp. 775–780, Aug. 2020.

[20] M. Abu-Sini and E. Yaakobi, "On Levenshtein's reconstruction problem under insertions, deletions, and substitutions," *IEEE Transactions on Information Theory*, vol. 67, no. 11, pp. 7132–7158, Sep. 2021.

[21] V. I. Levenshtein, "Elements of the coding theory (in Russian)," *Discrete mathematics and mathematics problems of cybernetics Nauka, Moscow*, pp. 207–235, 1974.

[22] D. S. Hirschberg and M. Regnier, "Tight bounds on the number of string subsequences," *Journal of Discrete Algorithms*, vol. 1, Jun. 2001.

[23] Y. Liron and M. Langberg, "A characterization of the number of subsequences obtained via the deletion channel," *IEEE Transactions on Information Theory*, vol. 61, no. 5, pp. 2300–2312, Mar. 2015.

[24] H. Mercier, M. Khabbazian, and V. K. Bhargava, "On the number of subsequences when deleting symbols from a string," *IEEE Transactions on Information Theory*, vol. 54, no. 7, pp. 3279–3285, Jun. 2008.

[25] J. H. van Lint and R. M. Wilson, *A course in combinatorics*, 2nd ed. Cambridge university press, 2001.

[26] A. A. Kulkarni and N. Kiyavash, "Non-asymptotic upper bounds for deletion correcting codes," *IEEE Transactions on Information Theory*, vol. 59, no. 8, pp. 5115–5130, Apr. 2013.

QoS Satisfaction Game for Random Access Resource Management

Guillaume Thiran
ICTEAM UCLouvain
Louvain-la-Neuve, Belgium
guillaume.thiran@uclouvain.be

Ivan Stupia
ICTEAM UCLouvain
Louvain-la-Neuve, Belgium
ivan.stupia@uclouvain.be

Luc Vandendorpe
ICTEAM UCLouvain
Louvain-la-Neuve, Belgium
luc.vandendorpe@uclouvain.be

I. Research Goal and Context

One of the critical aspects of emerging networks is their sustainability. In that context, the challenge of resource management schemes moves from the traditional maximisation of the nodes' performance, to the minimisation of the network resources' utilisation while fulfilling the devices' Quality of Service (QoS) demands. Although centralised schemes could be envisioned as a solution, they require gathering all local information in the nodes performing the resource allocation. This side-information exchange is in contradiction with the desired resource efficiency, and therefore autonomous schemes must be considered. In such protocols, the nodes compete for the shared resources, mainly based on local information. The challenge is then to provide conditions on the environment ensuring the nodes' interaction settles to an equilibrium at which their QoS requirements are satisfied.

II. State-of-the-art

Studying the interactions between wireless nodes has traditionally been tackled with the competitive Game Theory (GT) framework. Among others, such tool enables to obtain conditions guaranteeing the nodes' interaction settles to a unique equilibrium, named the Nash Equilibrium (NE) [1]. The caveat with this perspective is that the coupling between the nodes is assumed to lie in their objective functions, while their strategy set is fixed. When considering QoS constraints, the modelling of the q-th node instead looks as follows:

$$\begin{array}{ll} \text{minimise}_{\mathbf{x}_q} & 1, \\ \text{s.t.} & \mathbf{x}_q \in \mathcal{X}_q\left(\mathbf{x}_{-q}\right), \end{array}$$

with $\mathbf{x}_q$ the strategy of the q-th player and $\mathbf{x}_{-q}$ the strategy of all the other nodes except the q-th one. Given $\mathbf{x}_{-q}$, the constant unit objective represents the fact the player is indifferent between all resource profiles $\mathbf{x}_q$ fulfilling its QoS requirements, i.e., lying in the player-dependent strategy set $\mathcal{X}_q\left(\mathbf{x}_{-q}\right)$. Due to the constraint coupling, the interactions can be modelled as a Generalised Nash Equilibrium Problem (GNEP) with constant objective functions. In this context, the goal is to reach in an autonomous manner a Generalised Nash Equilibrium (GNE), which is a point at which all users have their QoS demands satisfied. However, except in some peculiar cases, totally autonomous schemes converging towards the equilibrium are lacking.

Guillaume Thiran is a Research Fellow of the Fonds de la Recherche Scientifique – FNRS.

III. Contributions

To tackle this problem, we design an algorithm compatible with autonomous nodes, and obtain the associated convergence conditions.

This algorithm, which is an instance of the totally asynchronous Best Response Dynamics (BRD), works by letting each player specify its utopia strategy $\mathbf{x}_q^{(u)}$, i.e., the strategy which would be chosen if there were no QoS requirements. Then, the algorithm amounts for each player at projecting $\mathbf{x}_q^{(u)}$ on the strategy set $\mathcal{X}_q\left(\mathbf{x}_{-q}\right)$, considering $\mathbf{x}_{-q}$ as fixed. The asynchronous character of the algorithm follows from the fact updates can happen at any time and possibly with outdated information about the other player strategies.

Conditions guaranteeing the convergence of this algorithm towards a GNE are obtained, under convexity, non-emptiness and differentiability assumptions. Moreover, it is assumed the strategy set can be represented by linear constraints with a variable Right-Hand Side (RHS), i.e., with constraints of the following form:

$$\mathbf{p}_q \mathbf{x}_q \leq \gamma_q\left(\mathbf{x}_{-q}\right),$$

where $\mathbf{p}_q$ is a fixed vector and $\gamma_q\left(\mathbf{x}_{-q}\right)$ a possibly non-linear function of the other players' strategies. The obtained conditions only depend on the vectors $\mathbf{p}_q$ and RHS functions $\gamma_q\left(\mathbf{x}_{-q}\right)$, ensuring convergence whatever the selected utopia point.

IV. Random Access Resource Management

Highlighting the impact of the proposed QoS satisfaction game methodology, a random access resource management problem is tackled. In an ALOHA-like random access scheme, devices tune their transmission probability under minimum rate and maximum power specifications. The rate requirement is coupled with the other devices, since communications are considered successful only when a single device is active, i.e., when there are no collisions. Formulating these interactions into the GNEP framework, the convergence conditions of the developed algorithm are shown to be fulfilled for low to moderate rate demands, analytically and numerically. Finally, a generalisation of the above is considered, in which nodes can assign probabilities not only to the binary states idle and active, but to a multi-power level scheme.

References

[1] G. Scutari, F. Facchinei, J.-S. Pang, and D. P. Palomar, "Real and complex monotone communication games," *IEEE Transactions on Information Theory*, vol. 60, no. 7, pp. 4197–4231, 2014.

MmWave Array Configuration Impact on Head-Mounted Display Performance

Alexander Marinšek*, Xuesong Cai†, Lieven De Strycker*, Fredrik Tufvesson†, Liesbet Van der Perre*
*ESAT-WaveCore, KU Leuven, Ghent, Belgium
†Department of Electrical and Information Technology, Lund University, Lund, Sweden
{alexander.marinsek, liesbet.vanderperre}@kuleuven.be

Keywords—Extended reality, wireless, millimeter-wave, antenna configuration, channel measurements

I. Introduction

In order to provide users with an immersive extended reality (XR) experience using a head-mounted display (HMD) that is both small and simple, remote rendering on a nearby edge server or computer is necessary [1]. To transmit the wireless XR content, millimeter-wave (mmWave) communication technology can be used due to its sufficient data rate [2]. However, mmWave channels have a sparsity problem in the angular domain, which means that distributed antenna arrays are needed to cover a larger angular area and to prevent outages when the HMD is rotated [3]. Despite this, a system with fewer antenna elements/arrays would be preferred due to lower complexity. Therefore, it is important to assess the trade-off between the number of antenna arrays and system performance to determine the best practical solution. This study presents indoor 28 GHz mmWave channel measurement data collected during HMD mobility, focusing on the dominant eigenmode (DE) gain. The DE gain is a critical factor in understanding system performance, as the sparsity of the mmWave channel and eigenmode imbalance often result in most of the available power being allocated to the DE. The DE gain also gives the upper bounds of achievable analog beamforming gain. **Please note that this introduction is elaborated in [4].**

Acknowledgement

Thanks to Meifang Zhu, Gilles Callebaut, and the volunteers at Lund Uni.

This work has received funding from the EU's Horizon 2020 and Horizon Europe programmes under grant agreements No. 861222 (MINTS) and 101096302 (6G Tandem).

The work is also partially supported by the Horizon Europe Framework Programme under the Marie Skłodowska-Curie grant agreement No.,101059091, the Swedish Research Council (Grant No. 2022-04691), the strategic research area ELLIIT, Excellence Center at Linköping — Lund in Information Technology, and Ericsson.

References

[1] F. Firouzi *et al.*, "The Convergence and Interplay of Edge, Fog, and Cloud in the AI-Driven Internet of Things (IoT)," *Information Systems*, vol. 107, p. 101840, 2022.

[2] A. Marinšek *et al.*, "Physical layer latency management mechanisms: A study for millimeter-wave wi-fi," *Electronics*, vol. 10, no. 13, 2021.

[3] X. Cai *et al.*, "Dynamic Channel Modeling for Indoor Millimeter-Wave Propagation Channels Based on Measurements," *IEEE Trans. Commun.*, vol. 68, pp. 5878–5891, Sept. 2020.

[4] A. Marinšek *et al.*, "Impact of Array Configuration on Head-Mounted Display Performance at mmWave Bands," in *2023 EUCNC*, (Gothenburg, Sweden), IEEE, to appear, 2023.

Prediction of Postinduction Hypotension by Machine Learning

1[st] Shuoyan Zhao
Department of Microelectronics
Delft University of Technology
Delft, The Netherlands
S.Zhao-4@student.tudelft.nl

2[nd] Alan Hamo
Department of Microelectronics
Delft University of Technology
Delft, The Netherlands
A.Hamo@student.tudelft.nl

3[rd] Niki Ottenhof
Department of Anaesthesia
Erasmus University Medical Center
Rotterdam, The Netherlands
n.ottenhof@erasmusmc.nl

4[th] Jan-Wiebe H Korstanje
Department of Anaesthesia
Erasmus University Medical Center
Rotterdam, The Netherlands
j.korstanje@erasmusmc.nl

5[th] Justin Dauwels
Department of Microelectronics
Delft University of Technology
Delft, The Netherlands
J.H.G.Dauwels@tudelft.nl

***Abstract*—Anesthesia-related hypotension is an adverse event during surgery that may occur within 15 minutes after induction and may lead to serious complications. Since the anesthetic drug is believed as an important role in the occurrence of post-induction hypotension (PIH) [1], anesthesiologists now advocate for the appropriate selection of anesthetics dosage to avoid PIH. To facilitate the selection, an accurate prediction of PIH associated with certain dosage of anesthetics is necessary. Electronic health records (EHRs) and machine learning (ML) technology have the potential in improving the accuracy of prediction, thereby aiding in the decision-making of anesthesia.**

The existing machine learning studies on PIH prediction face three main limitations. First, current methods rely on pre-existing data regarding anesthetics as inputs. This means that predictions can only be made after the induction process and thus can not offer decision support. Furthermore, many studies in hypotension prediction lack generality. For example, the use of continuous blood pressure measurement for general anesthesia is not common, yet the features collected by that are often of high importance in models [2]. Some features are also not available outside of the research context. Finally, the binary classification outputs, typically the occurrence of PIH some minutes later, are often useless for anesthesiologists to decide on anesthetic plans.

In this paper, we present a prediction model of PIH that supports anesthesia decision-making. The model is trained on EHRs of 913 patients undergoing general anesthesia in VitalDB [3], with 182 of them randomly separated for testing. Multiple injections are given in each case, resulting in approximately 3300 and 830 records for the training and test datasets, respectively. Fig 1.(a) shows three records. Besides features extracted from demographic data and vital signs, we also include the dosage of propofol (an anesthetic drug) as features before injections, mimicking an anesthetic plan in clinic.

We plan to evaluate the performance of different models under various settings, including different outputs (PIH defined as mean arterial pressure (MAP) <60, or as $\triangle$MAP$>20\%$), as shown in Fig 1.(b), and different algorithms (random forest [RF] [4] and extreme gradient boosting [XGBoost] [5]). On the testing dataset, RF classifier and XGBoost classifier achieve an average area under the receiver operating characteristic curve of 0.75 (precision = 0.74, recall = 0.70) and 0.82 (precision = 0.76, recall = 0.78), respectively, on the prediction of hypotension defined as $\triangle$MAP $>20\%$. We believe utilizing EHRs data to predict HIP can be useful for anesthesiologists in determining the appropriate anesthetic plan.

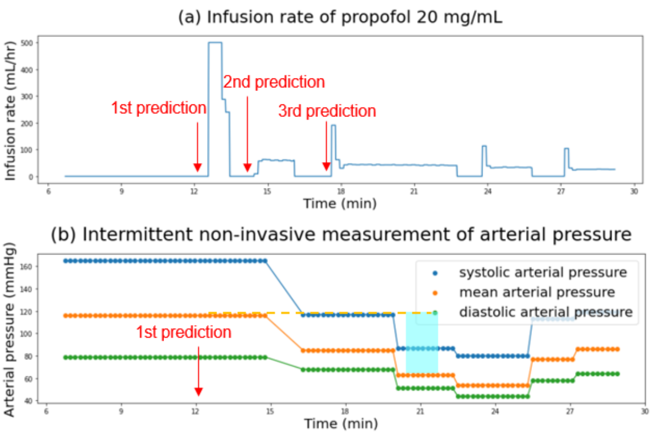

Fig. 1. Signal segments of anesthetic (propofol) injection rate and arterial pressure. (a) The prediction of HIP is performed before every injection. In each prediction, new vital signs and data about the upcoming dose to be injected are included. (b) The simultaneous drop in arterial pressure, highlighted by the rectangle, represents an occurrence of hypotension. It meets both of the two definitions of hypotension - MAP <60 and $\triangle$MAP $>20\%$.

References

[1] D. L. Reich, S. Hossain, M. Krol, B. Baez, P. Patel, A. Bernstein, and C. A. Bodian, "Predictors of hypotension after induction of general anesthesia," *Anesthesia & Analgesia*, vol. 101, no. 3, pp. 622–628, 2005.

[2] S. Kendale, P. Kulkarni, A. D. Rosenberg, and J. Wang, "Supervised machine-learning predictive analytics for prediction of postinduction hypotension," *Anesthesiology*, vol. 129, no. 4, pp. 675–688, 2018.

[3] H.-C. Lee, Y. Park, S. B. Yoon, S. M. Yang, D. Park, and C.-W. Jung, "Vitaldb, a high-fidelity multi-parameter vital signs database in surgical patients," *Scientific Data*, vol. 9, no. 1, p. 279, 2022.

[4] L. Breiman, "Random forests," *Machine learning*, vol. 45, pp. 5–32, 2001.

[5] T. Chen and C. Guestrin, "Xgboost: A scalable tree boosting system," in *Proceedings of the 22nd acm sigkdd international conference on knowledge discovery and data mining*, pp. 785–794, 2016.

Trajectory Smoothing for Distributed Formation Control of Multiagent Systems

Zhonggang Li and Raj Thilak Rajan
Faculty of EEMCS, Delft University of Technology, Delft, The Netherlands
{z.li-22, r.t.rajan}@tudelft.nl

***Abstract*—Multiagent systems have gained significant attention in recent years due to their potential to address complex problems. In applications such as autonomous sensing networks [1] and satellite interferometry [2], agents must maintain geometric patterns known as formations. Therefore, the distributed control of these agents is extensively studied in relevant fields. Currently, a substantial amount of literature focuses on using relative positions for formation control and maneuvering, as they can be acquired without access to global positioning [3]. In particular, [4] proposed a suite of distributed linear controllers for affine maneuver control where agents can track a prescribed trajectory that is a time-varying affine transformation of a desired configuration. However, since noisy measurements that construct the relative positions cannot be avoided, the convergence and tracking trajectories are subject to variations. In high-cost cases such as space applications, the noisy trajectory leads to excessive energy and time costs. Conventional filtering usually takes multiple independent snapshots of the relative positions for one control step and proposes estimators such as Maximum Likelihood Estimator (MLE) or Bayesian estimators to reduce the variance [5]. However, this is a strong assumption as the sampling rate cannot always be guaranteed. In such situations, filtering must take advantage of past information.**

In this work, we aim to smooth the trajectory of agents in a distributed formation control framework. As the local control law of the agents takes relative positions from the neighborhood, we develop algorithms to estimate them from the noisy observations without increasing the sampling rate. Note that this is different from the conventional conception of smoothing, as the processing is embedded in the real-time control loop, and the data is only available up to the current time step. One of our proposed filters adopts the philosophy of quadratic smoothing [6], where the squared norm of the pairwise difference of two successive noisy measurements is accounted for as a regularization in the regression. A proper time window is applied to the past observations to reduce the problem size and computation time. As this formulation has analytical solutions, it is numerically efficient and thus suitable for real-time control systems. We also study the relative kinematics of the systems and propose a relative state-space model for a Kalman filtering solution. As the proposed filters process the local variables, they can be implemented distributedly. Fig. 1 shows an example of a smoothed trajectory compared to an unfiltered one. The smoothness improvement using the proposed solutions is evident. Quantitative evaluation can also be performed in terms of, for example, the variance from multiple Monte Carlo runs. Note that our smoothing techniques are also compatible with [7] where observations losses are compensated by Kalman filtering with geometry constraints.

***Index Terms*—formation control, trajectory smoothing, distributed filtering**

This work is partially funded by the Sensor AI Lab, under the AI Labs program of Delft University of Technology.

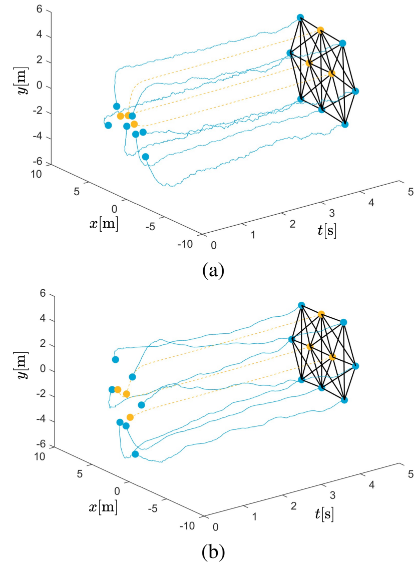

Fig. 1. Trajectories of a 2D formation across time. The formation involves 10 agents with the orange ones, the leaders, being GPS informed. The rest majority observe relative positions in the neighborhood for the local controller. (a) The trajectory of an unfiltered system using noisy observations of relative positions. (b) The trajectory of the system using the quadratic smoothing technique. Kalman filtering shows similar performances.

References

[1] Z. Wang, Z. Zhu, Z. Wei, X. Huang and B. Yin, "Research on Formation Control of Multiple Autonomous Underwater Vehicle Systems with Limited Communication," in *2017 International Conference Computer Systems, Electronics and Control (ICCSEC)*, pp. 343-346, 2017.

[2] D. Becker, M. D. Lachmann, S. T. Seidel, et al, "Space-borne Bose–Einstein condensation for precision interferometry," in *Nature*, vol. 562, pp. 391–395, 2018.

[3] S. Chen, D. Yin, and Y. Niu, "A Survey of Robot Swarms' Relative Localization Method," *Sensors*, vol. 22, no. 12, p. 4424, Jun. 2022, doi: 10.3390/s22124424.

[4] S. Zhao, "Affine Formation Maneuver Control of Multiagent Systems," in *IEEE Transactions on Automatic Control*, vol. 63, no. 12, pp. 4140-4155, Dec. 2018.

[5] M. Van Der Marel and R. T. Rajan, "Distributed Kalman Filters for Relative Formation Control of Multi-Agent Systems," in *2022 30th European Signal Processing Conference (EUSIPCO), Belgrade, Serbia*, pp. 1422-1426, 2022.

[6] S. Boyd and L. Vandenberghe, Convex Optimization. Cambridge University Press, 2004.

[7] Z. Li and R. T. Rajan, "Geometry Aware Distributed Kalman Filtering for Affine Formation Control under Observation Losses," Accepted in *2023 26th International Conference on Information Fusion (FUSION)*, 2023.

Demonstrating CSMA-NDA for Control Area Networks with Off-the-Shelf components

François Quitin and Michel Osée

Brussels School of Engineering, Université libre de Bruxelles (ULB)

I. Introduction

The Control Area Network (CAN) standard is a communication standard for cabled bus networks that is widely used in industrial environments. The CAN protocol implements the Carrier Sense Multiple Access/Non Destructive Arbitration (CSMA/NDA) protocol for medium access control. Since CSMA/NDA requires full-duplex transceivers, it was widely believed that CAN communications could not be implemented with wireless transceivers. In this paper, we demonstrate that it is possible to implement the CSMA/NDA protocol using On-Off Keying (OOK) modulation. We realize a proof-of-concept implementation using off-the-shelf wireless OOK transceivers, and show that our wireless transceivers are fully compatible with CAN controllers available on most micro-controller systems.

II. Wireless CAN protocol and proof-of-concept implementation

In this work, we propose to use the On-Off Keying (OOK) modulation format to implement wireless CSMA/NDA. This idea was first proposed theoretically in [1], and tested experimentally with software-defined radios in [2]. The block-diagram of a wireless CAN system is shown in Figure 1. The full paper will present a more detailed analysis of the wireless CAN system, as well as it's limitations.

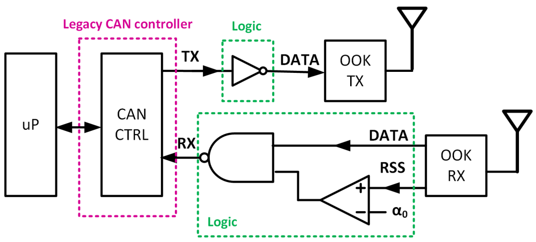

Fig. 1. Block diagram of a wireless CAN transceiver. The CAN controller is identical to one that can be used for cabled CAN buses, whereas the OOK Tx/Rx are conventional, off-the-shelf OOK transceivers.

The proposed system was implemented with off-the-shelf elements. To test our design, three nodes were realized and operated simultaneously. Node A transmits a message continuously with CAN ID `0x036` (low priority). Node B transmits a message every 100 ms with CAN ID `0x030` (higher priority). Node C just listens and acknowledges messages from the first two nodes (thus acting as the bus listener). An oscilloscope was used to measure three channels simultaneously: Channel 1 measures the `DATA` signal of the OOK transmitter of node A, Channel 2 measures the `DATA` signal of the OOK transmitter of node B, Channel 3 measures the `DATA` of the OOK receiver of node C (and is therefore just listening to the shared channel).

Figure 2 shows a result when operating the WiCAN nodes. The result show that nodes A and B are successfully able to implement the CSMA/NDA protocol over-the-air. The full paper will provide a detailed investigation of the experimental results.

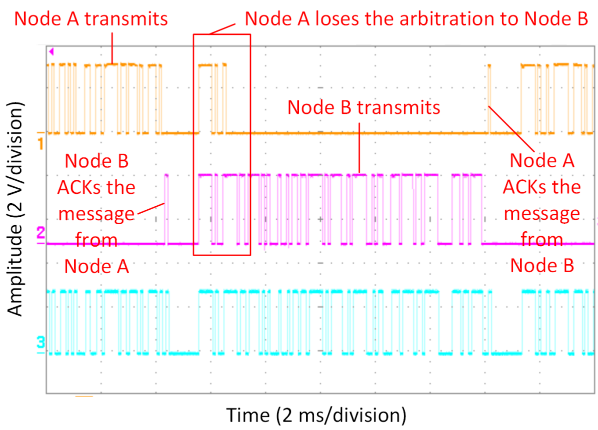

Fig. 2. Result of three Wireless CAN nodes operating simultaneously over a single data frame.

References

[1] Moshe Laifenfeld and Tal Philosof, "Wireless controller area network for in-vehicle communication," in *2014 IEEE 28th Convention of Electrical and Electronics Engineers in Israel (IEEEI)*, 2014, pp. 1–5.

[2] M. F. Ayten and F. Quitin, "Feasibility of csma/nda protocol for wirelesssystems using on-off keying," in *Symposium on Information Theory and Signal Processing in the Benelux (SITB)*, 2022.

Variance of Likelihood of Data

Fetze Pijlman
Research, Signify
Eindhoven, The Netherlands
fetze.pijlman@signify.com

Jean-Paul M. G. Linnartz
EE, T.U. Eindhoven and Research, Signify
Eindhoven, The Netherlands
j.p.linnartz@tue.nl, j.p.linnartz@signify.com

***Abstract*—Likelihood is a quantity that is used in various statistical approaches. For Bayesian models in combination with data sets an expression for the variance of the likelihood is derived in this paper. In this context, the paper introduces and studies the notion of a "self-likelihood" that quantifies to what extent a particular sample fits the model, inferred from all available samples, including the sample of interest itself. The variance turns out to be proportional to the difference of the self-likelihood and the ordinary likelihood. As the self-likelihood depends on the sample of interest, so will the variance depend on the sample of interest.**

I. INTRODUCTION

In statistical approaches, the likelihood quantifies how likely an observation is from a model perspective. The model is usually obtained by fitting parameters of a model on a data set. The fitted model is then used to compute likelihoods of (new) samples. Likelihoods of samples are used in various applications such as outlier detection. In order to draw reliable conclusions one should not only consider the likelihood value but also its uncertainty. In fact, the likelihood of a sample is a random variable, that can be seen as a function of the value of the current and earlier samples. Therefore, it is the object of this paper to find a relation between the likelihood value and its variance. In the next section, we will introduce the problem via a specific example. In the second and third section, we will define and derive the variance of the likelihood. We formulate a definition of the variance, and we interpret an intermediate results as a "self-likelihood". We further express how the likelihood and its variance can be obtained iteratively, as new data samples become available.

II. EXAMPLE: DAY-TIME WINTER TEMPERATURES IN NL

In this example we would like to learn about the population being the day-time temperature in the winter in the Netherlands. Somehow we know that it is normally distributed with a standard deviation of $\sigma = 5$ degrees but we do not know the mean of the population. If we would know the mean θ, then the probability density (pdf) of the temperatures would be

$$p(x|\theta) = \frac{1}{\sqrt{2\pi}\ \sigma}\ e^{-(x-\theta)^2/(2\sigma^2)}. \tag{1}$$

Thus, we simplify the notation $p_X(x)$ into $p(x)$ as it is clear for which random variable we express the pdf. A priori, we may have a belief about the mean of the population. In this example, we belief the mean is 4, thus $\theta_0 = 4$ degrees Celsius with a standard deviation of $\sigma_\theta = 3$ degrees (again normally distributed)

$$p(\theta) = \frac{1}{\sqrt{2\pi}\ 3}\ e^{-(\theta_0-\theta)^2/(2\sigma_0^2)}. \tag{2}$$

Combining the prior with our model, our belief on the day-time winter temperature distribution becomes

$$p(x) = \int \mathrm{d}\theta\ p(x|\theta)\ p(\theta). \tag{3}$$

where we introduced the notation $p(x)$ for the probability on x averaged over all model parameters θ.

Now suppose we are given data $X_{1:2}$ containing 2 independently drawn day-time winter temperatures X_1 and X_2 of the Netherlands being $x_1 = 8$ and $x_2 = 11$ degrees Celsius. This enables us to compute the posterior using Bayes rule

$$\begin{aligned} p(\theta|x_{1:2}) &= \frac{p(x_{1:2}|\theta)\ p(\theta)}{p(x_{1:2})} && (4)\\ &= \frac{1}{p(x_{1:2})}\frac{1}{2\pi\sigma^2} \\ &\quad \times e^{\left(-\frac{(x_1-\theta)^2}{2\sigma^2}-\frac{(x_2-\theta)^2}{2\sigma^2}\right)} p(\theta), && (5)\end{aligned}$$

where $x_1 = 8$, $x_2 = 11$, and $p(x_{1:2})$ is

$$p(x_{1:2}) = \frac{1}{2\pi\sigma^2}\int \mathrm{d}\theta\ e^{\left(-\frac{(x_1-\theta)^2}{2\sigma^2}-\frac{(x_2-\theta)^2}{2\sigma^2}\right)} p(\theta) \tag{6}$$

θ	$p(\theta\|x_{1:2} = \{8, 11\})$	$p(x = -9\|\theta)$
-2	.00024	.030
-1	.0011	.022
0	.0039	.016
1	.012	.011
2	.030	.0071
3	.061	.0045
4	.11	.0027
5	.15	.0016
6	.17	.00089
7	.17	.00048
8	.13	.00025
9	.087	.00012
10	.047	.000058

TABLE I: For various parameter values θ, the center column gives the posterior after observing 8 and 11 degrees Celsius and the last column gives the likelihood of for seeing -9 degrees Celsius.

After having seen the data our new belief on seeing a day-time temperature of $x_3 = -9$ degrees Celsius becomes

$$p_{\mathcal{M}}(x_3|x_{1:2}) = \int \mathrm{d}\theta\; p(x_3|\theta)\; p(\theta|x_{1:2}) \tag{7}$$

$$= \int \mathrm{d}\theta \frac{1}{\sqrt{2\pi}\sigma} e^{\left(-\frac{(x_3-\theta)^2}{2\sigma^2}\right)} p(\theta|x_{1:2}) \tag{8}$$

$$= 0.0015 \tag{9}$$

Intentionally, we use the symbol $p_{\mathcal{M}}()$ rather than $p()$, eventhough in this case it is also a pdf. Later we will rediscuss the role of $p_{\mathcal{M}}$, in particular to refine the pseudo dependency of x_3 of $x_{1:2}$ via θ.

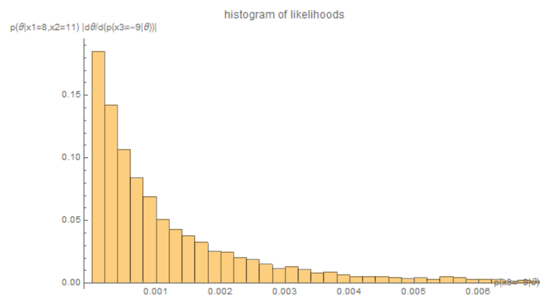

Fig. 1: Approximate histogram of the occurrence of likelihoods $p(x_3 = -9|\theta)$ in Eq. 7. Upon integration over θ some likelihood values $p(x_3|\theta)$ contribute to the integral more than others due to the posterior and the integration domain.

In this paper, we will show that the likelihood as computed above deserve careful interpretation. Table I shows for various parameter values the posterior (weight) and the likelihood of seeing -9 degrees Celsius. Some likelihoods appear "more often" in the integral than others. How much a certain likelihood contributes to the mean is shown in Figure 1. The computed likelihood of .0015 is basically a weighted mean and the importance of the mean depends on the spread of the underlying likelihoods. In this paper, we will show that the standard deviation being the root mean square deviation on those likelihoods can be computed analytically for any type of distribution. For the sample of -9 degrees Celsius, the standard deviation turns out to be 0.0022 which is quite large compared to the mean likelihood of 0.0015. For the sample of 4 degrees Celsius the likelihood is 0.066 and the standard deviation turns out to be 0.014 which is relatively much smaller.

III. Mathematical Formulation

The data is assumed to be multi-dimensional and a data set consisting of N samples will be denoted by $x_{1:N}$. Throughout this paper, it is assumed that all samples are independently drawn from a population. For instance, if $x_{1:N}$ would be a time series, there is no memory. In particular, samples are conditionally independent $p(x_{N+1}|x_{1:N};\theta) = p(x_{N+1}|\theta)$, thus for a given model with parameters θ, samples $1 : N$ give no extra information about x_{N+1}. Note that this does not imply that $P(x_{N+1}|x_{1:N}) = P(x_{N+1})$. In fact, $x_{1:N}$ reveal information about θ thus also about x_{N+1}: after seeing $X_{1:N-1}$, one can refine the posterior parameter distribution $p(\theta|x_{1:N})$ being

$$p(\theta|x_{1:N}) = \frac{p(x_{1:N}|\theta)\; p(\theta)}{\int \mathrm{d}\theta'\; p(x_{1:N}|\theta')\; p(\theta')}. \tag{10}$$

The posterior can be interpreted as measure of how likely the parameter θ is in the ensemble of all possible models. The denominator normalizes the posterior probability to unity.

When being confronted with a new sample x_{N+1} one can compute the average likelihood

$$E_{\theta|x_{1:N}}\left[P(x_{N+1}|\theta; x_{1:N})\right]$$

$$= \int \mathrm{d}\theta\; p(x_{N+1}|\theta; x_{1:N})\; p(\theta|x_{1:N}) \tag{11}$$

$$= \int \mathrm{d}\theta\; p(x_{N+1}|\theta)\; p(\theta|x_{1:N}). \tag{12}$$

Here, we used that samples are conditionally independent, thus $(P(y|X_{1:N};\theta) = P(y|\theta))$, and that all information from the previous samples can be collapsed into θ. Following the example discussed earlier, we introduce the following shorthand notation

$$p_{\mathcal{M}}(x_{N+1}|x_{1:N}) = \int \mathrm{d}\theta\; p(x_{N+1}|\theta)\; p(\theta|x_{1:N}). \tag{13}$$

The distribution of a new sample x_3 has a pseudo dependence on previous observed samples $X_{1:N}$ as previous samples affect the parameter distribution

θ of the model $\mathcal{M}$. Later on, in (21), we extend the above definition of $p_\mathcal{M}$.

IV. Variance of likelihood of a new sample

The likelihood of seeing a new sample x_{N+1} was computed by averaging the likelihood $p(x_{N+1}|\theta)$ over the posterior $p(\theta|x_{1:N})$. When judging whether this likelihood is low, such that we would need to qualify it as an outlier, we have to acknowledge that the likelihood depends on θ while earlier samples constrain θ. The resulting distribution of θ gives rise to a standard deviation of the likelihood which is defined as the root mean square of the deviations with regards to the mean.

$$\sigma^2_{p_\mathcal{M}(x_{N+1}|x_{1:N})} \tag{14}$$
$$= E_{\theta|x_{1:N}}\left[p(x_{N+1}|\theta, x_{1:N}) - p_\mathcal{M}(x_{N+1}|x_{1:N})\right)^2$$

Here, all terms are conditioned on $x_{1:N}$ The conditioning of the first term is not relevant, because we assumed conditional independent $P(x_{N+1}|\theta, x_{1:N}) = P(x_{N+1}|\theta)$. This gives

$$\sigma^2_{p_\mathcal{M}(x_{N+1}|x_{1:N})} \tag{15}$$
$$= E_{\theta|x_{1:N}}\left[\left(p(x_{N+1}|\theta) - p_\mathcal{M}(x_{N+1}|x_{1:N})\right)^2\right]$$
$$= \int d\theta \left(p(x_{N+1}|\theta) - p_\mathcal{M}(x_{N+1}|x_{1:N})\right)^2 p(\theta|x_{1:N})$$

Before the variance is derived, it will turn out to be useful to estimate the posterior for a data set $x_{1:N+1}$ which is the original data set $x_{1:N}$ that is extended with x_{N+1}. Using Bayes rule $p(x_{1:N}|\theta)p(\theta) = p(\theta|x_{1:N})p(x_{1:N})$ and conditional independence of x_{N+1} and $x_{1:N}$ gives

$$p(\theta|x_{1:N+1}) = \frac{p(x_{N+1}|\theta)\ p(x_{1:N}|\theta)\ p(\theta)}{\int d\theta' p(x_{N+1}|\theta') p(x_{1:N}|\theta') p(\theta')} \tag{16}$$

Dividing enumerator and denominator by $P(x_{1:N})$, gives

$$p(\theta|x_{1:N+1}) = \frac{p(x_{N+1}|\theta)\ p(\theta|x_{1:N})}{\int d\theta'\ p(x_{N+1}|\theta')\ p(\theta'|x_{1:N})} \tag{17}$$

Using the definition $p_\mathcal{M}$ this gives

$$p(\theta|x_{1:N+1}) = \frac{p(x_{N+1}|\theta)\ p(\theta|x_{1:N})}{p_\mathcal{M}(x_{N+1}|x_{1:N})}, \tag{18}$$

The variance (Eq. 15) can now be computed using Eq. 16:

$$\sigma^2_{p_\mathcal{M}(x_{N+1}|x_{1:N})} \tag{19}$$
$$= \int d\theta \left(p(x_{N+1}|\theta) - p_\mathcal{M}(x_{N+1}|x_{1:N})\right)^2 p(\theta|X_{1:N})$$
$$= p_\mathcal{M}(x_{N+1}|x_{1:N})^2$$
$$+ p_\mathcal{M}(x_{N+1}|x_{1:N}) \int d\theta\ p(x_{N+1}|\theta) p(\theta|x_{1:N+1})$$

This result can be interpreted as

$$\sigma^2_{p_\mathcal{M}(x_{N+1}|x_{1:N})} = p_\mathcal{M}(x_{N+1}|x_{1:N})$$
$$\times \left[p_\mathcal{M}(x_{N+1}|x_{1:N+1}) - p_\mathcal{M}(x_{N+1}|x_{1:N})\right], \tag{20}$$

where we introduced the self-likelihood $p_\mathcal{M}(x_{N+1}|x_{1:N+1})$. That is, we generalized the conditioning to cover a "self-likelihood", defined as

$$p_\mathcal{M}(x_{N+1}|x_{1:N+1}) = \int d\theta\ p(x_{N+1}|\theta) p(\theta|x_{1:N+1}). \tag{21}$$

Thus, we use not only $X_{1:N}$ but also the newest data X_{N+1} to refine the distribution of model θ and then obtain the likelihood of X_{N+1} from that model distribution. In fact, we define self-likelihood strictly as in the form of the integral (21), thus without the conditioning of the probability X_{N+1} on X_{N+1} itself, but only indirectly via a conditioning on θ. The self-likelihood allows us the identify likelihood of the latest sample where the latest sample is also used to establish an estimate of the model.

Note that the variance as defined in the Eq. **??** is non-negative, so the right hand side of Eq. (20) must also always be positive. In other words, the above equations prove that the self-likelihood of new data is always larger than the likelihood based on previous data only. That is, $P_\mathcal{M}(x_{N+1}|X_{1:N+1}) \geq P_\mathcal{M}(x_{N+1}|X_{1:N})$, which is intuitively appealing.

Discussion and Conclusion

Likelihood is a well-known quantity that is extensively used in statistical approaches. For a Bayesian model fitted on a data set, this paper defines the variance of the likelihood and derived an expression for it. The variance of likelihood for a new sample turns out to include additional posterior estimations that include that new sample. To derive an expression for the variance, we introduced the notion of "self-likelihood" to quantify a likelihood of a a new data sample, where we include that data sample itself to refine the inferred model parameters under which the likelihood (variance) is calculated. If the new posteriors substantially deviate from the old posterior then the variance will be large.

The variance estimation can be an alternative to the use of heavy-tailed distributions [1]. Such distributions are used to generate the largest tails possible given the data. This has the benefit that computed likelihoods can be seen as an upper limit so if it falls below a certain value it can be confidently considered to be an outlier. In this paper we showed that a variance calculation for a new sample involves a self-likelihood distribution that is especially high at the sample of interest. Therefore, it could be seen as generating a tail only in the direction of the new sample which would further increase the confidence.

We showed that the variance can be derived via additional posterior estimations, but such posterior estimations may be numerically expensive. In some cases such as novelty detection [2], one continuously updates the posteriors on incoming new data for improving the model description. An estimation of the variance may be of increasing interest in such applications.

REFERENCES

[1] Wikipedia contributors, "Heavy-tailed distribution — Wikipedia, the free encyclopedia," 2004, [Online; accessed 27-March-2023]. [Online]. Available: https://en.wikipedia.org/wiki/Heavy-tailed_distribution

[2] ——, "Novelty detection — Wikipedia, the free encyclopedia," 2004, [Online; accessed 27-March-2023]. [Online]. Available: https://en.wikipedia.org/wiki/Novelty_detection

A Semi-supervised Interactive Algorithm for Change Point Detection

1st Zhenxiang Cao
Department of Electrical Engineering (ESAT)
KU Leuven
Leuven, Belgium
zhenxiang.cao@esat.kuleuven.be

2nd Nick Seeuws
Department of Electrical Engineering (ESAT)
KU Leuven
Leuven, Belgium
nick.seeuws@esat.kuleuven.be

3rd Maarten De Vos
Department of Electrical Engineering (ESAT)
KU Leuven
Leuven, Belgium
maarten.devos@kuleuven.be

4th Alexander Bertrand
Department of Electrical Engineering (ESAT)
KU Leuven
Leuven, Belgium
alexander.bertrand@esat.kuleuven.be

Change point detection (CPD) aims to identify abrupt changes in the statistics of signals or time series, which reflect transitions in the underlying system. Most existing CPD methods are either built in fully supervised or unsupervised settings. Supervised methods treat the task as a multi-class [1] or binary [2] classification problem. Although they present acceptable performance in specific application fields, fully-labeled datasets are required during the training process, which can be difficult or impossible to obtain. Additionally, supervised methods may not generalize well to new application domains. Unsupervised methods [3]–[5] can address these limitations, but they cannot determine which type of change points the user is interested in, resulting in numerous undesired candidates and the possible omission of crucial, yet subtle changes..

To bridge the gap between supervised and unsupervised approaches, we introduce an active learning strategy for CPD. Specifically, we use the one-class classification model OCSVM [6], which is designed for novelty detection. This model can handle imbalanced data and detect outlier samples with change-relevant information. Our interactive CPD algorithm (ICPD) incorporates an active-learning strategy that leverages user feedback to improve the OCSVM model's learning process.

Our work has the following contributions:

(1) We introduce OCSVM as a core classifier for CPD within a novelty detection framework, which can overcome the issue of imbalanced training data.

(2) We develop an ICPD model that allows users to provide feedback and only report change points of interest.

(3) We demonstrate the effectiveness of the ICPD algorithm in detecting change points in both single- and multi-channel time series data, using both simulated and real-life datasets.

***Index Terms*—Active learning, Change point detection, One-class support vector machine**

I. Acknowledgments

This research received funding from the Flemish Government (AI Research Program) and from the European Research Council (ERC) under the European Union's Horizon 2020 research and innovation programme (grant agreement No.802895). All authors are affiliated to Leuven.AI - KU Leuven institute for AI, B-3000, Leuven, Belgium.

References

[1] Sasank Reddy, Min Mun, Jeff Burke, Deborah Estrin, Mark Hansen, and Mani Srivastava. Using mobile phones to determine transportation modes. *ACM Transactions on Sensor Networks (TOSN)*, 6(2):1–27, 2010.

[2] Frédéric Desobry, Manuel Davy, and Christian Doncarli. An online kernel change detection algorithm. *IEEE Transactions on Signal Processing*, 53(8):2961–2974, 2005.

[3] Michèle Basseville and Igor Nikiforov. *Detection of Abrupt Change Theory and Application*, volume 15. 04 1993.

[4] Song Liu, Makoto Yamada, Nigel Collier, and Masashi Sugiyama. Change-point detection in time-series data by relative density-ratio estimation. *Neural Networks*, 43:72–83, 2013.

[5] Tim Deryck, Maarten De Vos, and Alexander Bertrand. Change point detection in time series data using autoencoders with a time-invariant representation. *IEEE Transactions on Signal Processing*, 2021.

[6] Bernhard Schölkopf, Robert C Williamson, Alex Smola, John Shawe-Taylor, and John Platt. Support vector method for novelty detection. *Advances in neural information processing systems*, 12, 1999.

Detect-and-Avoid for multi-agent systems

Ellen Riemens, Raj Thilak Rajan
Signal Processing Systems (SPS) Group, Delft University of Technology, The Netherlands
{e.h.j.riemens, r.t.rajan}@tudelft.nl

***Abstract*—Multi-agent systems (MAS) are commonly used in various applications such as robotics, transportation, and communication systems [1] [2] [3] [4]. Ensuring collision-free navigation among these agents is critical to guarantee their safe operation, which often requires precise knowledge of the locations of the agents and/or a known formation of the network [2]- [4]. In this paper, a framework is proposed to find the required actuator inputs directly from relative position measurements between network agents, which combines Maximum Likelihood Estimator (MLE) [5] and Model Predictive Control (MPC) techniques [6].**

A set of agents denoted by $\mathcal{K}$ are tasked with reaching individual target positions without colliding with each other. To facilitate coordination, a communication graph $\mathcal{G}_s(\mathcal{K}, \mathcal{E}_c)$ and a sensing graph $\mathcal{G}_s(\mathcal{K}, \mathcal{E}_s)$ are constructed with communication and sensing radii of $r_c = r_s$, respectively. A single connected directed graph $\mathcal{G}(\mathcal{K}, \mathcal{E})$ is assumed to exist, and the initial positions of all agents $\mathbf{p}_k^0$ in D dimensions are known with high accuracy, either in the absolute or relative reference frame. All agents operate under single discrete integrator dynamics, where each agent's velocity is given by $\dot{\mathbf{p}}_k(n) = \mathbf{u}_k(n)$. The agents' positions at each time step are updated by a noisy discrete state transition function, given by $\mathbf{p}_k^n = \mathbf{p}_k^{n-1} + \mathbf{u}_k^{n-1}\Delta t + \boldsymbol{\eta}_k$, where $\boldsymbol{\eta}_k \sim \mathcal{N}(0, \boldsymbol{\Sigma}_1)$ is the state transition noise. The tracking posterior for each agent is defined as $p(\mathbf{p}_k^n | \mathbf{p}_k^{n-1}, \mathbf{u}_k^{n-1})$. The relative position measurement between agents k and j is given by $\mathbf{e}_{k,j} = \mathbf{p}_j - \mathbf{p}_k$, and the noisy measurements are defined as $\mathbf{w}_{k,j}^n = \mathbf{e}_{k,j}^n + \boldsymbol{\xi}_{k,j}$, where $\boldsymbol{\xi}_{k,j} \sim \mathcal{N}(0, \boldsymbol{\Sigma_2})$. The probability distribution of relative position is denoted by $p(\mathbf{e}(\mathbf{p}_k^n, \mathbf{p}_j^n) | \mathbf{w}_{i,j}^n)$.

A cost function is formulated for all agents in a global context in 1a. The cost function has two components: the first minimizes the negative likelihood of state transitions and relative position measurements [5], while the second minimizes the distance between agents' current positions and their goals over a time horizon T. A weighting parameter α balances these two objectives. Constraints include the dynamic model in (1b), the relationship between positions and relative measurements in (1c), a maximum velocity constraint in (1d), and a collision constraint in (1e), where $\boldsymbol{\eta}_{k,j} = \frac{\bar{\mathbf{p}}_k^{n+\tau} - \bar{\mathbf{p}}_j^{n+\tau}}{||\bar{\mathbf{p}}_k^{n+\tau} - \bar{\mathbf{p}}_j^{n+\tau}||}$ [6].

$$
\begin{aligned}
\min_{\mathbf{P}^n, \mathbf{U}^n} \; & -\alpha\{\sum_{k\in\mathcal{K}} \ln p(\mathbf{p}_k^n | \mathbf{p}_k^{n-1}, \mathbf{u}_k^{n-1}) + \sum_{k,j\in\mathcal{E}} \ln p(\mathbf{e}_{k,j}^n | \mathbf{w}_{k,j}^n)\} \\
& + (1-\alpha) \sum_{k\in\mathcal{K}} \sum_{\tau=0}^{T-1} \frac{||\mathbf{p}_k^{n+1+\tau} - \mathbf{p}_{\text{goal},k}||^2}{||\mathbf{p}_k^n - \mathbf{p}_{\text{goal},k}||^2} && \text{(1a)} \\
\text{s.t.} \quad & \mathbf{p}_k^{n+\tau+1} = \mathbf{p}_k^{n+\tau} + \mathbf{u}_k^{n+\tau}\Delta t && \text{(1b)} \\
& \mathbf{e}_{k,j}^n = \mathbf{p}_j^n - \mathbf{p}_k^n \quad \forall (k,j) \in \mathcal{E} && \text{(1c)} \\
& ||\mathbf{u}_k^{n+\tau}|| \leq u_{\max} \quad \forall k \in \mathcal{K}^{\mathbf{C}} && \text{(1d)} \\
& ||\bar{\mathbf{p}}_k^{n+\tau} - \bar{\mathbf{p}}_j^{n+\tau}|| + \boldsymbol{\eta}_{k,j}^{(n+\tau)T}[(\mathbf{p}_k^{n+\tau} - \mathbf{p}_j^{n+\tau}) \\
& \quad - (\bar{\mathbf{p}}_k^{n+\tau} - \bar{\mathbf{p}}_j^{n+\tau})] \geq r_{\text{collision}} && \text{(1e)}
\end{aligned}
$$

The optimization problem is solved using `Convex.jl`. The proposed joint framework can achieve collision-free navigation towards individual targets for all agents, assuming the existence of a suitable path. In figure 1, we show an example of a system of four agents. At $t = 1$, The agents' position is visualized with the path resulting from the above optimization problem in a dashed line. The respective goals are shown separately. At $t = 15$, it can be seen that the agents in blue and green risk a potential collision and react accordingly. At $t = 33$, further progression towards the goals is made.

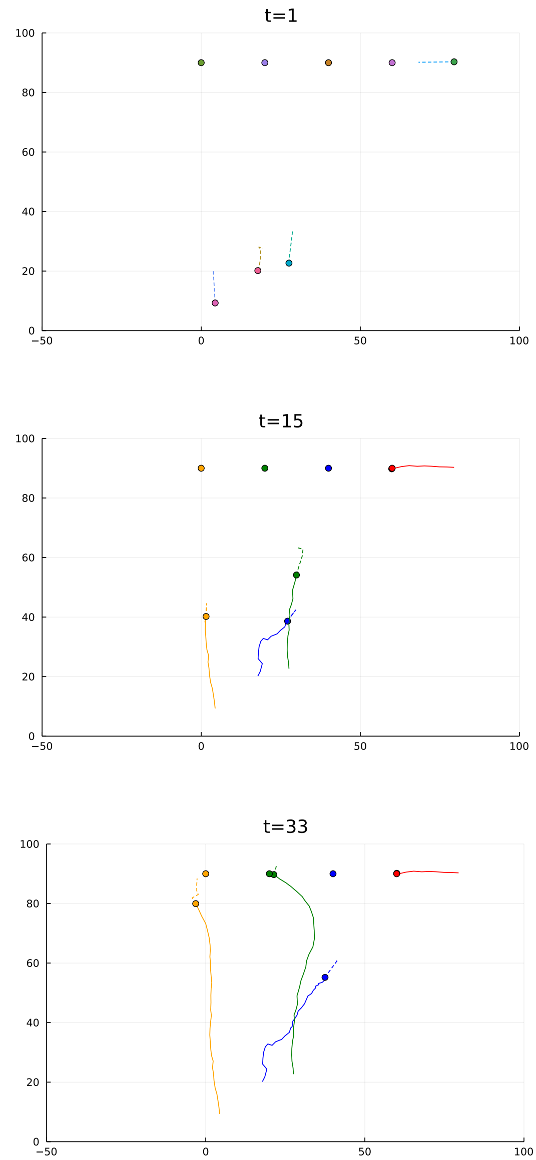

Fig. 1. Example trajectory for four agents at different time-steps. Dashed is the predicted trajectory over horizon T.

References

[1] R. T. Rajan, G. J. T. Leus, and A. J. van der Veen, "Relative kinematics of an anchorless network," *Signal Processing*, vol. 157, 2019.

[2] L. Ferranti, L. Lyons, R. R. Negenborn, T. Keviczky, and J. Alonso-Mora, "Distributed Nonlinear Trajectory Optimization for Multi-Robot Motion Planning," *IEEE Transactions on Control Systems Technology*, pp. 1–16, 2022.

[3] X. He, Q. Wang, and Y. Hao, "Finite-time adaptive formation control for multi-agent systems with uncertainties under collision avoidance and connectivity maintenance," *Science China Technological Sciences*, vol. 63, no. 11, pp. 2305–2314, Nov. 2020.

[4] B. Yan, P. Shi, C.-C. Lim, and Z. Shi, "Optimal robust formation control for heterogeneous multi-agent systems based on reinforcement learning," *International Journal of Robust and Nonlinear Control*, vol. 32, no. 5, pp. 2683–2704, 2022.

[5] A. Simonetto and G. Leus, "Distributed maximum likelihood sensor network localization," *IEEE Transactions on Signal Processing*, vol. 62, no. 6, pp. 1424–1437, 2014.

[6] F. Rey, Z. Pan, A. Hauswirth, and J. Lygeros, "Fully Decentralized ADMM for Coordination and Collision Avoidance," in *2018 European Control Conference (ECC)*, Jun. 2018, pp. 825–830.

Identifying Temporal Correlations Between Natural One-Shot Videos and EEG Signals

1st Yuanyuan Yao
Dept. of Electrical Engineering, STADIUS
KU Leuven
Leuven, Belgium
yuanyuan.yao@esat.kuleuven.be

2nd Axel Stebner
Dept. of Electrical Engineering, PSI
KU Leuven
Leuven, Belgium
axel.stebner@esat.kuleuven.be

3rd Tinne Tuytelaars
Dept. of Electrical Engineering, PSI
KU Leuven
Leuven, Belgium
tinne.tuytelaars@esat.kuleuven.be

4th Simon Geirnaert
Dept. of Electrical Engineering, STADIUS
Dept. of Neurosciences, ExpORL
KU Leuven
Leuven, Belgium
simon.geirnaert@esat.kuleuven.be

5th Alexander Bertrand
Dept. of Electrical Engineering, STADIUS
KU Leuven
Leuven, Belgium
alexander.bertrand@esat.kuleuven.be

***Abstract*—Understanding how naturalistic stimuli such as audio and video are encoded in the brain is a fundamental challenge in brain-computer interfaces (BCIs). A popular technology to record neural responses is electroencephalography (EEG), which records electrical activity of the brain through electrodes attached to the scalp. While neural responses to natural speech have been successfully decoded from EEG [1], [2], the decoding of natural video footage from EEG has not received much attention. It is a challenging problem due to the high-dimensional nature of video signals and the notoriously low signal-to-noise ratio (SNR) of EEG signals. Findings in this area will bring new experimental paradigms in BCIs and lay foundations for applications such as visual attention decoding.**

A few studies found significant inter-subject correlations in the EEG signals of subjects watching the same video clips using Correlated Component Analysis (CorrCA) [3]–[5], indicating the existence of EEG components that are time-locked to the visual stimuli. However, it is not clear by what characteristics of the video these responses were driven. In [5], the authors extracted the derivative of pixel intensity (temporal contrast) as a feature and found that it was correlated with the first shared EEG component obtained by CorrCA. Apart from temporal contrast, the average velocity of pixels calculated from the optical flow was also shown to be correlated with individual EEG signals using Canonical Correlation Analysis (CCA) in [6]. These results suggest that the temporal contrast and optical flow may elicit strong time-locked EEG responses.

In this work, we argue that the correlations found in [5] and [6] are mainly driven by scene cuts in the videos, i.e., sudden changes from one scene to another, instead of changes in pixel intensity or average velocity of pixels. To avoid introducing confounds related to scene cuts and to reduce the complexity of stimuli, we select a set of one-shot videos containing a single moving object (a person) and record the EEG signals of subjects watching them. We show that no significant correlations between the features mentioned above and recorded EEG signals can be found by CCA in the absence of scene cuts, and propose a new video feature based on motion that does correlate with the EEG. Moreover, we also demonstrate that the EEG components found with the new feature are not driven by eye movements. Finally, we jointly analyze the EEG signals of all subjects with the proposed feature as side information using Stimulus-Informed Generalized Canonical Correlation Analysis (SI-GCCA) [7] (Figure 1), and show that it leads to higher inter-subject correlations than solely considering the EEG signals.

This research is funded by the Research Foundation - Flanders (FWO) project No G081722N, the European Research Council (ERC) under the European Union's Horizon 2020 research and innovation program (grant agreement No 802895), the Flemish Government (AI Research Program), and the PDM mandate from KU Leuven (for S. Geirnaert, No PDMT1/22/009). The scientific responsibility is assumed by its authors. All authors are also affiliated with Leuven.AI - KU Leuven institute for AI, Belgium.

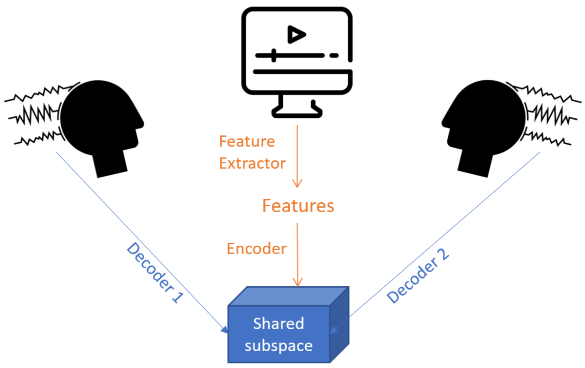

Fig. 1: An illustration of SI-GCCA when there are two subjects. The goal is to find EEG decoders and a shared subspace which is closest to the transformed EEG signals. The distance between the shared subspace and the transformed visual stimuli is added as a regularization term.

References

[1] A. de Cheveigné, D. D. Wong, G. M. Di Liberto, J. Hjortkjær, M. Slaney, and E. Lalor, "Decoding the auditory brain with canonical component analysis," *NeuroImage*, vol. 172, pp. 206–216, 2018.

[2] S. Geirnaert, S. Vandecappelle, E. Alickovic, A. de Cheveigne, E. Lalor, B. T. Meyer, S. Miran, T. Francart, and A. Bertrand, "Electroencephalography-based auditory attention decoding: Toward neurosteered hearing devices," *IEEE Signal Processing Magazine*, vol. 38, no. 4, pp. 89–102, 2021.

[3] J. P. Dmochowski, P. Sajda, J. Dias, and L. C. Parra, "Correlated components of ongoing eeg point to emotionally laden attention–a possible marker of engagement?," *Frontiers in human neuroscience*, vol. 6, p. 112, 2012.

[4] J. R. Zhang, J. Sherwin, J. Dmochowski, P. Sajda, and J. R. Kender, "Correlating speaker gestures in political debates with audience engagement measured via eeg," in *Proceedings of the 22nd ACM international conference on multimedia*, pp. 387–396, 2014.

[5] A. T. Poulsen, S. Kamronn, J. Dmochowski, L. C. Parra, and L. K. Hansen, "Eeg in the classroom: Synchronised neural recordings during video presentation," *Scientific reports*, vol. 7, no. 1, pp. 1–9, 2017.

[6] J. P. Dmochowski, J. J. Ki, P. DeGuzman, P. Sajda, and L. C. Parra, "Extracting multidimensional stimulus-response correlations using hybrid encoding-decoding of neural activity," *NeuroImage*, vol. 180, pp. 134–146, 2018.

[7] S. Geirnaert, T. Francart, and A. Bertrand, "Stimulus-informed generalized canonical correlation analysis of stimulus-following brain responses," *arXiv preprint arXiv:2210.13297*, 2022.

Deep learning-based Image Retrieval from Videos

Sinian Li
Department of Microelectronics
Delft University of Technology
Delft, Netherlands
S.Li-47@student.tudelft.nl

Doruk Barokas Profeta
Department of Microelectronics
Delft University of Technology
Delft, Netherlands
D.BarokasProfeta@student.tudelft.nl

Justin Dauwels
Department of Microelectronics
Delft University of Technology
Delft, Netherlands
J.H.G.Dauwels@tudelft.nl

Abstract

The advent of streaming and video has revolutionized the way materials are presented in various fields, including history and art. Scholars seek a more efficient solution to retrieving digital materials from videos without spending excessive time and energy filtering out irrelevant information. The integration of deep learning methodologies has proven to empower the search process. Motivated by promising applications in various fields, we propose and validate a deep-learning-based image retrieval from video system.

In this paper, we propose decomposing the task into two stages: detecting keyframes and conducting content-based image retrieval (CBIR), shown in Fig. 1.

In the first stage, the input query video is down-sampled, denoted as the first box (Keyframe Extraction, KFE). This step uses a color histogram-based clustering algorithm [1]. Each frame is processed and modeled into blocks. The histogram features of all blocks are concatenated into a feature vector. All frame features are then combined to form a feature-frame matrix. Subsequently, it reduces the dimension of the feature matrix by SVD, as processing large matrices is time-consuming and limited to improving accuracy. The clustering algorithm uses cosine similarity check to compare adjacent frames' similarity and cluster the feature space, detect boundaries, and extract keyframes. Similarly, another model VSUMM [3] uses the HSV color model and K-means clustering to obtain keyframes.

In the second stage, CBIR (see the orange box in Figure 1) involves Feature Extraction (FE) and Search and Match (SaM). With regard to efficiency and accuracy, feature extraction is the most crucial part. We currently use a fine-tuned ResNet101-based feature extractor in cooperation with GeM Pooling [2]. To better improve efficiency, shallower networks with re-ranking techniques are also competent in tackling this task. Re-ranking is a module that uses global features to refine the retrieval results.

The contribution of this paper is providing an efficient and accurate image retrieval from video system that could be applied in historical or multi-media research to expedite their search process. Table I shows that the current KFE module outshines state-of-the-art methods when keeping the redundancy relatively low. This represents a significant improvement in accuracy and efficiency. The Mean Efficiency Ratio (MER) is defined as the average computation time-to-video duration ratio, reflecting the computational cost. A smaller MER indicates better efficiency. The proposed method achieved a 5-fold increase in efficiency compared to VSUMM and a 10-fold increase compared to the up-to-date color histogram-based method.

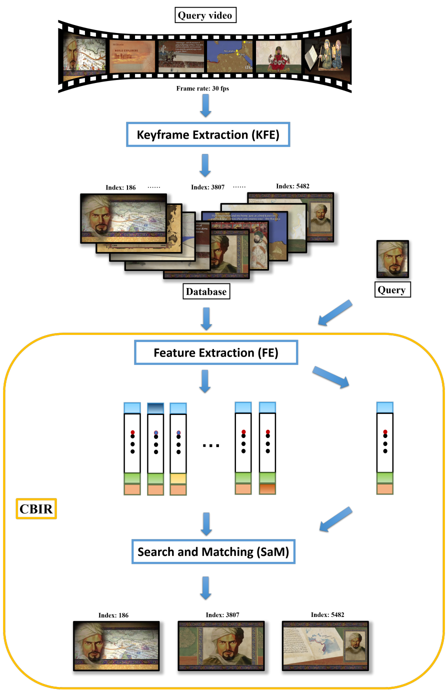

Fig. 1. The pipeline of the Image Retrieval from Video Engine

We would like to acknowledge SPS group, Department of Microelectronics, Delft University of Technology and FAST funding for providing financial support for this research.

TABLE I
PROCESSING TIME OF DIFFERENT METHODS COMPARISON

Methods	Mean efficiency ratio	Mean accuracy	Mean redundancy
VSUMM [2]	0.18	0.87	0.42
Gong [1]	0.35	0.76	**0.38**
Proposed	**0.03**	**0.95**	0.39

References

[1] Yihong Gong and Xin Liu, "Video summarization using singular value decomposition," Proceedings IEEE Conference on Computer Vision and Pattern Recognition. CVPR 2000 (Cat. No.PR00662), Hilton Head Island, SC, 2000, pp. 174-180 vol.2, doi: 10.1109/CVPR.2000.854772.

[2] F. Radenović, G. Tolias and O. Chum, "Fine-Tuning CNN Image Retrieval with No Human Annotation," in IEEE Transactions on Pattern Analysis and Machine Intelligence, vol. 41, no. 7, pp. 1655-1668, 1 July 2019, doi: 10.1109/TPAMI.2018.2846566.

[3] S.E.F. de Avila, A.P.B. Lopes, A. da Luz, and A. de Albuquerque Araújo, "VSUMM: A mechanism designed to produce static video summaries and a novel evaluation method," Pattern Recognition Letters, vol. 32, no. 1, pp. 56-68, 2011. doi: 10.1016/j.patrec.2010.08.004.

Barrett's Neoplasia Detection using a minimal Integer-based Neural Network for Embedded Systems Integration

1st Tim G.W. Boers
dept. of electical engineering
Eindhoven University of Technology
Eindhoven, the Netherlands
t.boers@tue.nl

2nd Carolus H.J. Kusters
Eindhoven University of Technology
Eindhoven, the Netherlands

3rd Kiki N. Fockens
Amsterdam University Medical Center
Amsterdam, the Netherlands

4th Jelmer B. Jukema
Amsterdam University Medical Center
Amsterdam, the Netherlands

5th Martijn B . Jong
Amsterdam University Medical Center
Amsterdam, the Netherlands

6th Jeroen de Groof
Amsterdam University Medical Center
Amsterdam, the Netherlands

7th Jacques J. Bergman
Amsterdam University Medical Center
Amsterdam, the Netherlands

8nd Fons van der Sommen
Eindhoven University of Technology
Eindhoven, the Netherlands

9nd Peter H.N de With
Eindhoven University of Technology
Eindhoven, the Netherlands

***Abstract*—Despite the popularity of neural networks in medical studies, such systems are found in peripheral settings and integrated solutions have not yet been reported for Barrett's neoplasia detection. In order to integrate neural networks in medical equipment, specialized optimizations for preparing their integration in a high-efficiency and power-constrained environment are required. In this paper, the feasibility of quantized networks with limited memory for the detection of Barrett's neoplasia is researched. An Efficientnet-lite0+Deeplabv3 architecture is proposed, which is trained using a quantization-aware training scheme to achieve an 8-bit integer-based model. The proposed quantized model with only 4-MB memory is capable of reaching the similar performance scores of 93.3% Area Under the Curve (AUC), compared to a full-precision Resnet18+U-Net architecture, but with a dramatic 92% reduction of the model size. We have also optimized the segmentation head for efficiency and reduced the output to a resolution of 32×32 pixels. These results show that this reduced segmentation head also achieves a similar level of expression as the U-net model, and reaches a DICE score of 73%. The proposed lightweight approach makes the model highly energy-efficient, since it can be real-time executed on a 2-Watt Coral Edge TPU. The obtained low-power consumption of the lightweight Barrett's esophagus neoplasia detection and segmentation system enables the direct integration into standard endoscopic equipment.**

***Index Terms*—Embedded systems, full-integer quantization, Barrett's neoplasia detection**

I. Introduction

Neural networks (NNs) have become common ground for the detection and segmentation of neoplastic lesions in Barrett's esophagus patients. The potential benefits of CADe and CADx studies have broadly shown that computer-assisted diagnosis can successfully facilitate the physician [2]. However, despite this popularity in research environments, such systems have not been found in peripheral settings and integrated solutions have not yet been reported. This gap between the practical usage in a clinical setting and the broad research of NNs is still significant. The optimal solution of applying NNs in practice in the medical domain is integration into embedded equipment, in this case an endoscopic system. Integration offers a great advantage for the physicians and avoids expensive add-on equipment and platforms. Therefore, this paper aims at exploring the integration of NNs into such systems. In our case, we have cooperated with an existing equipment manufacturer[1].

However, the execution of NNs in real-time embedded systems require optimizations for efficiency and training strategies due to constraints on computational power. Yet, simple embedded hardware only has limited computational precision (integer-based) and limited memory capacity, while modern state-of-the-art NNs require high computational resources beyond the capabilities of many embedded processor units. Therefore, to facilitate the implementation of NNs on commercially available medical systems, it is necessary to reduce the computational footprint, memory usage, and lower the complexity and adapt the NN to embedded hardware capabilities, such as integer-based operations.

Optimizations of the NN design can be categorized into micro-architecture and macro-oriented optimizations. The micro-architecture optimization focuses on improving the operations in the network layers. For example, a widely adopted

[1]The cooperation with Olympus Corp., Tokyo, Japan, is acknowledged.

optimization introduced by Howard *et al.* [4] is the integration of depth-wise separable convolutions [8]–[10]. In order to improve quantization compatibility, Sandler *et al.* [7] introduced ReLU6. Jacob *et al.* [6] presented a method to remove the batch-normalization operations by integrating the normalization into the adjacent convolutional layers. The macro-oriented search is used to optimize the topological structure of a neural network. These optimizations introduce new modules into the architecture, which can help to improve accuracy, such as squeeze-and-excitation [5] and residual modules [3]. Tan *et al.* [11] introduced EfficientNet, which optimizes the scaling of neural networks for depth, width, and input resolution.

Further optimization by quantization can be achieved to reduce the memory footprint and simplify the operations of NNs via special training and architectural optimizations. This technique involves transforming floating-point operations, typically operated at 32 bits, into low-precision floating-point or integer values. Recent research has shown consistent success in the translation to 8-bit integer-precision calculations [6], [12]. Quantization offers several performance benefits, (1) the ability to adapt NNs to processors that can only perform integer-based operations, (2) improved throughput on processors optimized for low-precision data formats, and (3) reduced bandwidth requirements for loading data into memory. There are two main methods for quantizing NNs: post-training quantization (PTQ) and quantization aware-training (QAT). PTQ measures the activation ranges of an already trained NN using (unlabeled) data, and quantizes the weights and activations accordingly. Alternatively, QAT involves introducing quantization noise resulting from rounding errors into the NN during training, in order to optimize the quantized weights and activations to achieve a nearly lossless accuracy.

In this paper, we evaluate the feasibility of quantized neural networks (NNs) for medical applications. In particular, this work concentrates on the use case of Barrett's neoplasia detection in white-light endoscopy (WLE). The proposed system involves the development of an embedded framework, which combines the EfficientNet-lite [8] encoder plus DeeplabV3 decoder [9] and then transforms the network into a quantized version, based on QAT to achieve a full-integer-based network. Finally, the full-integer model is tested on a Coral edge Tensor Processing Unit (TPU), which is broadly accepted for computing platforms and is optimized for executing NNs.

In summary, our contributions are threefold. (1) We demonstrate that full-integer-based NNs achieve comparable performances to single-precision floating-point models for Barrett's neoplasia detection. (2) An efficient decoder design is proposed that is optimized for the detection of neoplasia to further decrease the computing footprint of the NN, while maintaining good segmentation details. (3) we present an optimized architecture with a reduced model size of 23% without performance loss of previously published work. The authors conjecture that this developed model can be applied to other endoscopic tasks as well. To our knowledge, we are the first to study and evaluate an embedded version for endoscopic Barrett's surveillance.

II. Materials and Methods

A. Data

Collection: A dedicated data set for Barrett's neoplasia detection in WLE is collected for training, validating and testing. The classification labels for the images are based on a histologically proven ground truth. Clinical research fellows have manually selected each image and assigned each of them to a set, based on a patient split, while assuring that each set is representative for the various tumor characteristics, described by the Paris classification. De-identification is performed in line with the General Data Protection Regulation (EU) 2016/679. The training set consists of 6,237 neoplastic images (1304 patients) and 7,595 Non-Dysplastic Barrett's Esophagus (NDBE) images (1,103 patients), the validation set contains 100 neoplastic images (54 patients) and 100 NDBE images (36 patients). Finally, the test set contains 100 neoplastic images (50 patients) and 300 NDBE images (125 patients). **Annotation:** A subset of 2,651 neoplastic images is delineated twice by two experts on Barrett's neoplasia. One delineated area is the Higher-Likelihood (HL), which contains the area that is definitely considered neoplasia by the expert. The second area is the Lower-Likelihood (LL), which is atypical from normal NDBE tissue, which could be neoplasia. In total, 14 international experts have contributed to the delineations. For the HL neoplasia delineation, a minimal consensus of 30% DICE is implemented between experts in order to ensure that both delineate the same area. If the DICE score is less than 30%, then a third expert is invited to annotate the image as well. The two most overlapping delineations are then used to generate the ground truth. Finally, a consensus ground truth to train the model is defined as the union of the two HL areas unified with the intersection of the LL areas.

B. Network Architecture

The proposed network architecture is constructed using an ImageNet-pretrained EfficientNet-Lite0 feature encoder and a MobileNetV2 DeepLabV3+ segmentation decoder, which are both optimized for fast and efficient processing of real-time imagery and compatible for quantization. This architecture is an optimized design of the model proposed by Boers *et al.* [1], where we replace the Efficientnet-lite1 encoder with an Efficientnet-lite0 encoder.

1) Optimizations at the macro level: The network provides two output heads for classification and segmentation. This allows for joint training, and mutual information exchange to the feature extractor, in order to improve feature learning for both tasks. In contrast to similar segmentation models, as in MobileNetV2 [9], the feature maps are downscaled 4 times to 8×8-pixel resolution in the encoder instead of only 2 times, since this is more resource-efficient. These feature maps are then up-scaled in the decoder, which outputs a 32×32-pixel resolution segmentation map. The segmentation mask is then subsequently up-scaled to the original input resolution. Given that tumors are blob-like shapes, this resolution preserves sufficient detail to clearly segment a neoplastic area.

2) Optimizations at the micro level: The presented encoder and decoder architectures are optimized for efficient processing and compatibility with quantization techniques. To achieve this, only operations are considered that can efficiently execute computational tasks in parallel. To this end, depth-wise separable convolutions have been utilized as a key implementation, enabling faster processing times on compute-restricted devices by requiring fewer operations during execution. The architecture features ReLU6 activation functions that limit the range of the activation output, significantly improving its suitability for quantization. These proposed optimizations enables suitability of quantization of the model, therefore allowing the integration into resource-constrained and low-power medical devices for real-time applications.

3) Experimental Setup:

- *Software:* For Coral EdgeTPU optimizations, the following software packages are employed: Cuda 11.6, CuDNN 7.6.2, Tensorflow 2.9.1, Tensorflow Model Optimization Toolkit 0.7.2 and PyCoral 2.0.0.
- *Hardware:* All our training experiments are performed on a desktop with an i9-9820X CPU, 32 GB of RAM and an RTX 2080 Ti GPU. The final testing of the quantized model is performed on a Coral Edge TPU, which is integrated into an MSI GS65 laptop. The Edge TPU platform is an ASIC accelerator, which makes it possible to efficiently execute the model on a 2-Watt TPU and achieves real-time performance using quantized 8-bit integer operations.

The proposed network architecture is compared to a Resnet-18+U-net model, which is employed by de Groof *et al.* [2] in a clinical setting. The architecture is also compared to the original Efficientnet-lite1 variant proposed by Boers *et al.* [1].

C. Training

The training is split into two stages. In the first stage, all the models are trained in full-float32 precision. The second stage is used to further fine-tune the 8-bit compatible models using QAT, by introducing 8-bit integer rounding errors in the training. This two-stage approach generally leads to better results for QAT, since the pre-quantized weights start already at a good minimum in the loss landscape.

The models are trained with a batch size of 32 for 75 epochs in the first stage, and 25 epochs in the second stage. The applied optimizer is Adam with AMS-grad with a weight decay of 10^{-4}, and a learning rate of 10^{-3} and 10^{-5} for the first and second stage, respectively. A step-wise learning-rate scheduler is used to control the learning rate. For the encoder head, we employ a binary cross-entropy (BCE) loss function and for the decoder head of the network, we use a compound DICE+BCE loss function. Images and segmentation masks are randomly rotated with $\theta \in \{0°, 90°, 180°, 270°\}$ and randomly flipped along the $x-$axis and $y-$axis with probability p=0.5. Additionally, random permutations are made to the contrast, brightness and saturation of the images. The training images are randomly sampled such that each class is represented 50%, to compensate for class-imbalance in the training set.

1) Quantization aware-training (QAT) Scheme: QAT involves introducing rounding errors via a consecutive quantization and dequantization step into the training of the NN weights. These steps are formally expressed in Equations (1) and (3) for 8-bit signed-integer quantization. These quantization functions are applied to the NN weights and activations. The quantization function is specified by:

$$x_q = \text{Quant}(x, S, Z) = \text{Clip}(\text{Round}(\frac{x}{S} + Z)), \qquad (1)$$

where parameter x_q is the quantized form of the input x, based on the scale factor S (Real) and the zero-point control value Z (integer). The Round($\cdot$) operation rounds the input to the nearest integer. The clip function is specified by:

$$\text{Clip}(x) = \begin{cases} -128, & x < -128; \\ x, & -128 \leq x \leq +127; \\ +127, & x > +127. \end{cases} \qquad (2)$$

The dequantization function is defined by:

$$\hat{x} = \text{Dequant}(x_q, S, Z) = (x_q - Z) \cdot S, \qquad (3)$$

where $\hat{x}$ is the dequantized float32 value of x with quantization noise applied. The scaling factor S and the zero-point control value Z are calculated based the moving-average filtering to obtain the maximum value α and minimum value β. The scaling and zero-point control values are computed as follows:

$$S = \frac{\alpha - \beta}{255}, \qquad (4)$$

$$Z = -\text{round}(\beta \cdot s) - 128. \qquad (5)$$

D. Full-integer inference scheme

After QAT, the model can be converted, in order to execute in integer-precision mode using the Tensorflow-lite library. In this process, the model weights are converted to int8 precision, batch-normalization folding is applied and all dropout layers are removed in order to save computation power. After the conversion, the model requires new computational graphs, which are provided by Algorithm 1, Algorithm 2 and Equation (6), which represent the Tensorflow-lite reference implementation.

The following function returns two output values, i.e. $\text{multiplier}_\text{q}$ and a shiftvalue, which are computed by combining all scaling factors of the input, filter and output stage, using the "frexp" function, resulting in:

$$\text{multiplier}_\text{q}, \text{shiftvalue} = \text{frexp}\left(\frac{S_\text{input} \cdot S_\text{filter}}{S_\text{output}}\right). \qquad (6)$$

Here, the first and second output values are together fitting in the expression "$\text{multiplier}_\text{q}$ * 2**shiftvalue", which describes their role as mantissa and exponent value, respectively.

TABLE I: Performance comparison of the proposed EfficientNet-lite0+DeeplabV3 architecture in 8-bit integer precision, compared with the EfficientNet-lite1+DeeplabV3 architecture and the float32-precision version baseline U-Net. The presented results are the average values of 5 full training cycles. The values between the brackets denote the standard deviation.

Design	Exec.	Size (MB)	Size Red. (↓%)	AUC (%)	Accuracy (%)	Sens. (%)	Spec. (%)	DICE (%)
ResNet18+U-Net	Fp32	56.1	-92.30	94.10 (0.80)	83.88 (1.76)	91.66 (2.19)	81.40 (1.84)	72.87 (1.65)
Boers *et al.*	Int8	5.2	-23.21	93.30 (0.12)	80.13 (2.30)	91.50 (0.72)	76.33 (2.83)	69.44 (2.14)
Proposed NN	Int8	4.3	baseline	93.77 (0.41)	82.87 (2.66)	90.25 (4.35)	80.42 (4.72)	72.55 (3.40)

Algorithm 1 Full-integer execution of a 2D convolution

Input: Four arrays: input, filter, output, bias. Each array carries its own quantization parameters S and Z.
Output: An 8-bit feature map as a product of the quantized convolution of the input and the filter.
function INTEGERCONVOLUTION2D(input, filter, output, bias)
  for $x_i, y_i, c_i = 1$ to X_i, Y_i, C_i **do** // iterate over the width, height and channels
    acc = 0 // initialize an accumulator with int32 precision
    for $x_f, y_f = 1$ to X_f, Y_f **do** // iterate over the filter width and height
      $acc = acc + (input[x_i,y_i,c_i] + zeropoint_i) * filter[x_f,y_f]$
    end for
    $acc = acc + bias[c_i]$
    acc = MULTIPLYBYQUANTIZEDMULTIPLIER(acc, $multiplier_q$, $shiftvalue$)
    $acc = acc + zeropoint_o$ // acc is shifted by the zeropoint value of the output
    acc = CLIP((acc), QUANTIZE(0), QUANTIZE(6)) // ReLU6 in quant. dom.
    output[x_i, y_i, c_i] ← CAST(acc) // cast array to int8 precision
  end for
  return output

Algorithm 2 Multiplication step of the quantized feature map

Input: An input value, multiplier and shifting value
Output: MultiplyByQuantizedMultiplier($accumul.$, $multipl._q$, $shiftval.$)
function MULTIPLYBYQUANTIZEDMULTIPLIER($accumulator$, $multiplier_q$, $shiftvalue$)
  $totalshift = 31 - shiftvalue$
  $round = 1 << (totalshift - 1)$
  $result = accumulator * multiplier_q + round$
  $result = results >> totalshift$
  return $result$

III. Results

This section presents the detection results of the NNs. The experiments are repeated 5 times with a different initialization of the network heads and data augmentation for each NN. Table I reports the mean results along with the standard deviation between brackets. The results are based on the output of the segmentation head, where the neoplasia score (classification) is defined as the maximum pixel value in the segmentation mask. A detection is therefore regarded positive when this value exceeds a threshold of 0.5. Our quantized network executes at more than 35 frames/second.

IV. Discussion and Conclusion

This work presents a novel lightweight quantized 8-bit architecture that enables real-time execution on resource-constrained or embedded computing devices for endoscopic surveillance of Barrett's esophagus neoplasia. This architecture constitutes a refinement of the model proposed by Boers *et al.* and achieves similar performance with a 23% reduction in model size. Moreover, the proposed model demonstrates also comparable detection performances as a full-precision U-Net architecture, but with a dramatic 92% reduction in model size. In addition, the proposed model achieves a real-time video frame rate of more than 35 frames/second when executed on a 2-Watt Coral Edge TPU, which is particularly noteworthy for power-constrained solutions in the medical field.

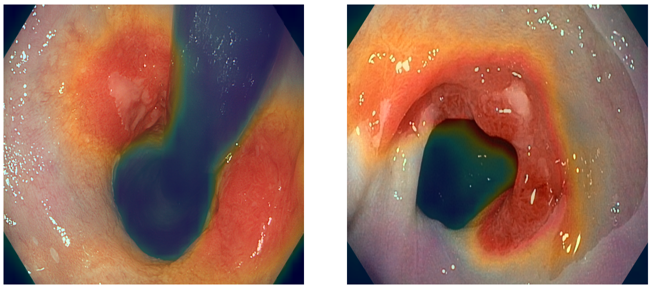

(a) (b)

Fig. 1: Examples of the obtained heat maps from the segmentation head of the EfficientNet-lite0+DeeplabV3 architecture used for Barrett's neoplasia detection.

The proposed decoder yields a DICE score of 72.55%, which demonstrates that the proposed model has similar expressive capabilities as a U-net model for the detection of Barrett's neoplasia. Hence, the 32×32 segmentation map provides sufficient resolution to capture the shape of the neoplastic region, enabling clinicians to identify and address potential neoplastic areas in the esophagus (refer to Figure 1). The implementation of this low-resolution segmentation head is beneficial in the sense that it reduces the number of operations, while maintaining a detailed segmentation of the tumor, thus highlighting the neoplastic area.

Furthermore, although the presented model is already relatively small, it can still be further reduced in size by utilizing model pruning. This technique involves the removal of model filters that do not significantly contribute to the prediction results of the network, while maintaining the original performance level. Future research could explore the impact of this technique on the proposed architecture, potentially leading to further reductions in model size and computational complexity. Moreover, it would be advantageous to investigate the impact of various quantization strategies on the performance of the model, as this could provide further optimization opportunities and facilitate the design of even more efficient architectures.

Finally, in order to thoroughly evaluate the proposed system, it would be beneficial to test the architecture on a larger and more diverse dataset, which could offer insight into the model's generalization and potential limitations. It is worth noting that the proposed framework can be extended to other medical imaging modalities and utilized for other disease detection tasks. This versatility can enhance the impact and applicability of the proposed model, potentially providing clinicians with powerful tools for diagnosis and treatment planning in a variety of medical contexts.

In conclusion, the presented work introduces a novel, lightweight architecture for the detection of Barrett's neoplasia, which relies exclusively on integer-based operations and significantly reduces memory usage, rendering it suitable for direct embedded employment using resource-constrained medical hardware with low power consumption. We have demonstrated that the proposed techniques achieve similar levels of performance compared to those achieved by standard floating-point neural networks. Moreover, the lightweight design enhances energy efficiency, allowing for real-time execution on a 2-Watt Coral Edge TPU, which is particularly advantageous in the clinical context. This obtained low-power consumption of the lightweight Barrett's esophagus neoplasia detection and segmentation system enables the direct integration into standard endoscopic equipment.

REFERENCES

[1] T. G. Boers, C. H. Kusters, K. N. Fockens, J. B. Jukema, M. Jong, J. de Groof, J. J. Bergman, F. van der Sommen, and P. H. de With, "Barrett's lesion detection using a minimal integer-based neural network for embedded systems integration," in *Proceedings SPIE 12645, Medical Imaging 2023: Computer-Aided Diagnosis*. SPIE, 2023.

[2] A. J. de Groof, M. R. Struyvenberg, J. van der Putten, F. van der Sommen, K. N. Fockens, W. L. Curvers, S. Zinger, R. E. Pouw, E. Coron, F. Baldaque-Silva *et al.*, "Deep-learning system detects neoplasia in patients with barrett's esophagus with higher accuracy than endoscopists in a multistep training and validation study with benchmarking," *Gastroenterology*, vol. 158, no. 4, pp. 915–929, 2020.

[3] K. He, X. Zhang, S. Ren, and J. Sun, "Deep residual learning for image recognition," in *Proceedings of the IEEE conference on computer vision and pattern recognition*, 2016, pp. 770–778.

[4] A. G. Howard, M. Zhu, B. Chen, D. Kalenichenko, W. Wang, T. Weyand, M. Andreetto, and H. Adam, "Mobilenets: Efficient convolutional neural networks for mobile vision applications," *arXiv :1704.04861*, 2017.

[5] J. Hu, L. Shen, and G. Sun, "Squeeze-and-excitation networks," in *IEEE CVPR Proceedings*, 2018, pp. 7132–7141.

[6] B. Jacob, S. Kligys, B. Chen, M. Zhu, M. Tang, A. Howard, H. Adam, and D. Kalenichenko, "Quantization and training of neural networks for efficient integer-arithmetic-only inference," in *Proceedings of the IEEE conference on computer vision and pattern recognition*, 2018, pp. 2704–2713.

[7] A. Krizhevsky and G. Hinton, "Convolutional deep belief networks on cifar-10," *Unpublished manuscript*, 2010.

[8] R. Liu, "Higher accuracy on vision models with efficientnet-lite," *TensorFlow Blog*, 2020.

[9] M. Sandler, A. Howard, M. Zhu, A. Zhmoginov, and L.-C. Chen, "Mobilenetv2: Inverted residuals and linear bottlenecks," in *Proceedings of the IEEE conference on CVPR*, 2018, pp. 4510–4520.

[10] M. Tan, B. Chen, R. Pang, V. Vasudevan, M. Sandler, A. Howard, and Q. V. Le, "Mnasnet: Platform-aware neural architecture search for mobile," in *Proceedings of the IEEE/CVF CVPR*, 2019, pp. 2820–2828.

[11] M. Tan and Q. Le, "Efficientnet: Rethinking model scaling for convolutional neural networks," in *International conference on machine learning*. PMLR, 2019, pp. 6105–6114.

[12] H. Wu, P. Judd, X. Zhang, M. Isaev, and P. Micikevicius, "Integer quantization for deep learning inference: Principles and empirical evaluation," *arXiv preprint arXiv:2004.09602*, 2020.

Linear Discriminant Analysis with unlabelled data

1st Nicolas Heintz
Dept. of Electrical Engineering, STADIUS
Dept. of Neurosciences, ExpORL
KU Leuven
Leuven, Belgium
nicolas.heintz@esat.kuleuven.be

2nd Tom Francart
Dept. of Neurosciences, ExpORL
KU Leuven
Leuven, Belgium
tom.francart@kuleuven.be

3rd Alexander Bertrand
Dept. of Electrical Engineering, STADIUS
KU Leuven
Leuven, Belgium
alexander.bertrand@esat.kuleuven.be

***Abstract*—Ever since Linear Discriminant Analysis (LDA) was first introduced by Fisher [1], it has become one of the most popular tools for (linear) classification [2]. LDA finds the linear transformation that maximally separates two classes, in the sense that it minimises the ratio of the variance within a class to the distance between classes. It has a closed-form solution that is elegant, easy to understand and cheap to compute. Furthermore, although it only minimises the classification error for homoscedastic Gaussian distributions, its inherent objective function of maximally separating the classes stays relevant when these assumptions are not met. Because of these advantages, LDA has become a popular model in a vast array of signal processing applications [2]–[6].**

LDA has nevertheless a major drawback: it requires a good estimation of both the class averages and the class covariances of the relevant data. These statistics are usually estimated using labelled training data. However, in many applications such labelled data are not available, or is difficult to obtain. Furthermore, if the data were sampled from a non-stationary process, these statistics would need to be regularly re-estimated, which is often infeasible in practice.

Surprisingly, not all the aforementioned statistics must actually be known to compute the LDA projection. We demonstrate that it is possible to compute the LDA projection based on unlabelled data, if some minimal prior information is available. To be precise, it suffices to know either (1) the class average of a single class, (2) the difference between the class averages up to a scaling or (3) the covariances of both classes up to a scaling. We refer to this framework as minimally informed LDA (MILDA). Furthermore, the MILDA model also has a closed formulation and a comparable cost to LDA, keeping the main advantages of LDA.

Naturally, it is unrealistic to expect that the used ground truth statistic is exactly correct. However, even when estimation errors are taken into account, MILDA closely matches the performance of LDA. In fact, we show that the MILDA model becomes more robust to estimation errors as the two classes become harder to separate or when the classes are less balanced. These scenarios are often the hardest for unsupervised and semi-supervised models, making this an appealing property.

This research is funded by Aspirant Grant 1S31522N (for N. Heintz) from the Research Foundation - Flanders (FWO), the Research Foundation - Flanders (FWO) project No G0A4918N and G081722N, the European Research Council (ERC) under the European Union's Horizon 2020 research and innovation program (grant agreement No 802895 and grant agreement No 637424), and the Flemish Government (AI Research Program). The scientific responsibility is assumed by its authors.
N. Heintz, T. Francart and A. Bertrand are also affiliated with Leuven.AI - KU Leuven institute for AI, Belgium.

References

[1] R. A. Fisher, "The Use of Multiple Measurements in Taxonomic Problems," *Annals of Eugenics*, vol. 7, pp. 179–188, 9 1936.
[2] T. Hastie, R. Tibshirani, and J. Friedman, *The Elements of Statistical Learning*. Springer Series in Statistics, New York, NY: Springer New York, 2009.
[3] C. Bouveyron, G. Celeux, T. B. Murpy, and A. E. Raftery, *Model-Based Clustering and Classification for Data Science*. Cambridge University Press, 2019.
[4] R. Fu, Y. Tian, T. Bao, Z. Meng, and P. Shi, "Improvement Motor Imagery EEG Classification Based on Regularized Linear Discriminant Analysis," *Journal of Medical Systems*, vol. 43, no. 6, 2019.
[5] A. Sharma and K. K. Paliwal, "Linear discriminant analysis for the small sample size problem: an overview," *International Journal of Machine Learning and Cybernetics*, pp. 1–12, 2014.
[6] C. W. Antuvan and L. Masia, "An LDA-Based Approach for Real-Time Simultaneous Classification of Movements Using Surface Electromyography," *IEEE transactions on neural systems and rehabilitation engineering*, vol. 27, no. 3, pp. 552–561, 2019.

Machine learning algorithm to predict cardiac output based on arterial pressure measurements

Alan Hamo*, Shuoyan Zhao*, Niki Ottenhof†, Jan-Wiebe H Korstanje†, Justin Dauwels*
* Department of Microelectronics, Delft University of Technology, Delft, the Netherlands.
† Department of Anaesthesia, Erasmus University Medical Center, Rotterdam, the Netherlands.

Cardiac output (CO) plays a crucial role in determining the delivery of oxygen to tissues and is a key metric in hemodynamic optimization. The gold standard method for measuring cardiac output is through thermodilution using pulmonary artery catheter, but it is an invasive procedure associated with complications during placement and the need for a skilled expert to perform the measurements. An alternative approach is to estimate cardiac output by utilizing arterial blood pressure (ABP) measurements, which is a minimally invasive technique. However, the relationship between ABP and CO is not yet fully understood. Several models and techniques have been proposed to describe the relationship between CO and ABP such as hemodynamics models [1], deep learning [2], and machine learning regression models [3]. Nevertheless, existing literature inadequately addresses the following challenges: the number of cardiac cycles required to achieve optimal performance, and data imbalance in CO measurements. In this study, we aim to utilize regression-based machine learning techniques and feature engineering to estimate CO from ABP. Hemodynamics and waveform features, along with demographic information of the patient, are integrated to enhance the accuracy of the model. We utilized the publicly available VitalDB [4] (Vital Database) waveforms to extract arterial blood pressure (ABP) waveforms, corresponding cardiac output (CO), and patient demographic information. We identified 47 cases (patients) that had complete measurements. Each CO measurement at time T_0, with corresponding ABP at $(T_{0-15s} - T_0)$, was considered a sample. We collected the first 350 samples from each patient, yielding a total of 16450 samples. After down-sampling and filtering the signals, the following features were extracted:

Hemodynamic	**Waveform**	**Demographic**
Heart rate	seasonality	Age
Systolic pressure	trend	Weight
Onset pressure	ACF, PACF	Height
Mean pressure	length	BMI
Liljestrand-Zander model	mean, variance, median, std	
systolic area model	absolute energy, entropy	

After feature extraction, an imbalance in the target distribution was observed, making it hard to model the relation between ABP and CO. To deal with this problem, SINDy (sparse identification of non-linear dynamics) algorithm [5] was used to augment the features in an attempt to capture the non-linear terms relating ABP features and CO. Using the sparsely extracted features, we conducted an experiment to investigate the optimal number of cardiac cycles needed to achieve the best performance. We tested the performance for 2, 3, 4, 5, 6, 7, and 8 cardiac cycles using two regression models, namely, automatic relevance determination regressor and ridge regressor [6]. Our results indicate that 3 cardiac cycles provide the optimal performance in terms of RMSE, MAE, r, r2, bias, and limits of agreements. Using the optimal number of cardiac cycles, we tested seven regression models, including linear regressor, ridge regressor, kernel ridge regressor, support vector machine regressor, random forest regressor, decision tree regressor, and XGBoost regressor. To ensure the reliability of our results, we validated the models using leave-one-patient-out cross-validation. Our findings demonstrate that ridge is the most effective model that fits the data, achieving an RMSE of 1.129, MAE of 0.994, r of 0.798, r2 of 0.630, a bias of -0.01, and limits of agreement of -2.32 and 2.30.

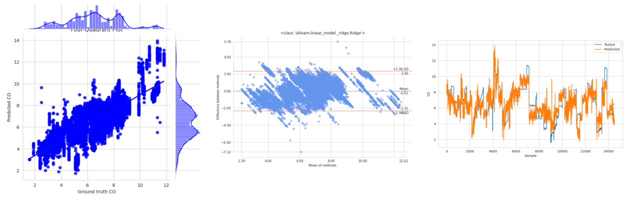

Fig. 1. (left) Four-quadrant, (mid) Bland-Altman (right) Tracking-ability.

For future work, we aim to enhance our study by incorporating additional data and exploring the identification of ABP dynamics and its relation to CO.

References

[1] J. X. Sun, A. T. Reisner, M. Saeed, T. Heldt, and R. G. Mark, "The cardiac output from blood pressure algorithms trial," *Critical care medicine*, vol. 37, no. 1, p. 72, 2009.

[2] H.-L. Yang, C.-W. Jung, S. M. Yang, M.-S. Kim, S. Shim, K. H. Lee, and H.-C. Lee, "Development and validation of an arterial pressure-based cardiac output algorithm using a convolutional neural network: retrospective study based on prospective registry data," *JMIR Medical Informatics*, vol. 9, no. 8, p. e24762, 2021.

[3] L. Ke, A. Elibol, X. Wei, L. Cenyu, W. Wei, and N. Y. Chong, "Machine learning algorithm to predict cardiac output using arterial pressure waveform analysis," in *2022 IEEE International Conference on Bioinformatics and Biomedicine (BIBM)*. IEEE, 2022, pp. 1586–1591.

[4] H.-C. Lee, Y. Park, S. B. Yoon, S. M. Yang, D. Park, and C.-W. Jung, "Vitaldb, a high-fidelity multi-parameter vital signs database in surgical patients," *Scientific Data*, vol. 9, no. 1, p. 279, 2022.

[5] S. L. Brunton, J. L. Proctor, and J. N. Kutz, "Sparse identification of nonlinear dynamics with control (sindyc)," *IFAC-PapersOnLine*, vol. 49, no. 18, pp. 710–715, 2016.

[6] A. E. Hoerl and R. W. Kennard, "Ridge regression: Biased estimation for nonorthogonal problems," *Technometrics*, vol. 12, no. 1, pp. 55–67, 1970.

Automated Calibration of CCTV Cameras

1st Giacomo D'Amicantonio
Technological University of Eindhoven
g.d.amicantonio@tue.nl

2nd Egor Bondarau
Technological University of Eindhoven
e.bondarau@tue.nl

3rd Peter H.N. De With
Technological University of Eindhoven
p.h.n.de.with@tue.nl

I. Introduction

The topic of camera calibration has been of great interest in the Computer Vision community for decades. Extrinsic and intrinsic calibration is required for applications such as sports video broadcasting, object localization and immersive imaging. A multitude of methods and algorithms have been proposed to perform semi-automated calibration in different contexts. Unfortunately, these methods are often impractical in real-world setups such as traffic surveillance cameras, which require frequent and automated re-calibration. We propose a method for automated calibration of traffic cameras that requires only the topview image of an intersection and its semantically segmented map. Our method brings two improvements to the SOTA approaches: a novel loss function called Topological Loss (TL) and a custom implementation of the Spatial Transformer Network (STN) [1].

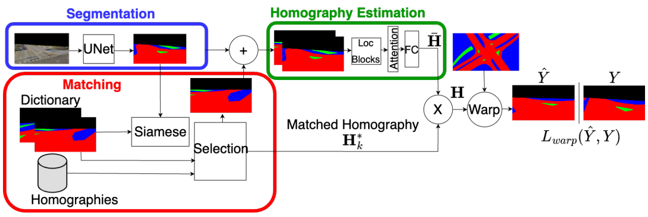

Fig. 1. Architecture of the proposed model. The homography $\hat{\mathbf{H}}$ is estimated by three so-called Localization Blocks (LocBlock) and three fully connected (FC) layers. The two matrices $\hat{\mathbf{H}}$ and $\mathbf{H}_K^*$ are multiplied to produce the final homography $\mathbf{H}$. The model warps the bird's-eye view with $\mathbf{H}$ to generate the image $\hat{Y}$.

II. Method

We generate thousands of homographies by sampling intrinsic parameters, rotation angles and camera translations. We use these homographies to warp both topviews and generate virtual camera views. The camera views are split in training, testing and dictionary splits. The segmentation component of our proposed model, shown in Figure 1, semantically segments the input image and produces a semantic map. The second component of our model, a Siamese network, retrieves the closest match for the semantic map from the dictionary of templates. The two images are concatenated across the channel dimension and passed to the thirs component of our model, the STN. Our implementation of the STN consists of three Localization Blocks, each containing three convolutions connected via skip connect and followed by batch normalization and GELU activation. Finally, a self-attention layer and three fully-connected layers estimate an homography matrix. The homography of the matched image and the estimated one are multiplied to obtain the final homography. The topview is then warped with the resulting homography. The image created by the model and the semantic ground truth used for the segmentation component are compared using a pixel-based loss function. Comparing two semantic images in this way incurs in the pitfall of parts of the images being identical while depicting very different parts of the intersection. To address this problem, our TL splits the two images is patches and computes a score between corresponding patches using a pixel-based loss function such as MSE or Dice Loss as shown in Figure 2. Each patch's score is summed to the scores of its neighbouring patches to enforce the model to generate images consistent with the topology of the intersection.

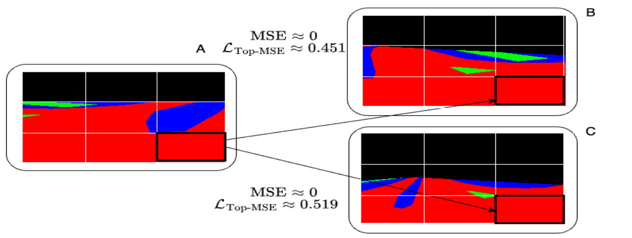

Fig. 2. MSE and $\mathcal{L}_{\text{Top-MSE}}$ scores between two patches. Notice that, using MSE, the patch would be considered almost completely correct while using $\mathcal{L}_{\text{Top-MSE}}$, the error is quite large.

TABLE I
IoU scores.

Method	**Measured IoU**			
	$\mathcal{L}_{\text{Top-MSE}}$	MSE	$\mathcal{L}_{\text{Top-Dice}}$	Dice
Sha et al.	75.93%	75.15%	**76.18%**	74.77%
Ours	85.12%	83.29%	**87.00%**	84.71%

III. Results

We compare the proposed model and loss function with the previous SOTA model proposed by Sha et al. [2], which used a similar approach. The performance improvement brought by TL can be noticed by comparing adjacent columns in Table I. We implemented TL using both Dice Loss and MSE to show that the idea behind it is sound. The STN improvement can be observed by comparing the rows in the table. The combination of TL and the new STN improves upon the competitor's results by up to 11%.

IV. Conclusion

Our proposed model and loss function proved to be very effective to automatically re-calibrate traffic surveillance cameras. Future work should focus on improving the matching component.

References

[1] M. Jaderberg, K. Simonyan, A. Zisserman, and K. Kavukcuoglu, "Spatial transformer networks," NIPS, 2015.

[2] L. Sha, J. Hobbs, P. Felsen, X. Wei, P. Lucey, and S. Ganguly, "End-to-end camera calibration for broadcast videos," in *CVPR*, 2020.

Efficient Content-Based Image Retrieval from Videos using Compact Deep Learning Network and Local Descriptors

Doruk Barokas Profeta
Delft University of Technology
Delft, Netherlands

Sinian Li
Delft University of Technology
Delft, Netherlands

Justin Dauwels
Delft University of Technology
Department of Microelectronics
Delft, Netherlands
J.H.G.Dauwels@tudelft.nl

Andrea Nanetti
Nanyang Technological University
School of Art, Design and Media
Singapore

***Index Terms*—content-based image retrieval, MobileNetV2, feature fusion, video image retrieval, color histogram, key frame extraction**

I. Introduction

With the advent of streaming and video technologies, there has been a significant shift in the way information is presented, especially in fields such as healthcare [1], education, history, and art. Efficiently accessing, filtering, and navigating digital content is a top priority for scholars who wish to make the most of their time and resources.

Deep learning methods have proved crucial in this search process, helping scholars streamline their search by eliminating irrelevant data and enabling them to focus on the most pertinent information. This integration of deep learning has paved the way for a more effective way of leveraging digital resources, allowing scholars to make the most of the vast amount of data available to them. However, the problem of deep learning methods, which rely on global descriptors, has made it difficult for scholars to efficiently navigate content. The need for a more effective means of indexing, retrieving, and filtering through digital resources has become increasingly important, leading scholars to explore the potential of local descriptors.

Local descriptors are a powerful tool that provides an efficient solution for searching digital content, allowing scholars to concentrate on specific aspects of the data, and their importance in various fields cannot be overstated; however, their reliance on manual feature extraction and the need for large amounts of annotated data are significant limitations [2].

To address these issues, we propose a hybrid feature extraction method, providing scholars with a powerful tool for accessing and utilizing digital materials efficiently. Local features can help to identify distinctive keypoints that are robust to noise and geometric transformations, while global features can help to resolve ambiguities and confirm the consistency of the matching across the entire image. This approach enables scholars to focus on relevant aspects of data, thereby enhancing the search process.

II. Methodology

In this paper, we propose decomposing the task into two stages: detecting keyframes and conducting content-based image retrieval (CBIR), shown in Figure 1.

A. Key Frame Extraction

The first stage of the proposed video retrieval method involves downsampling the input query video using a color histogram-based clustering algorithm [3]. To increase efficiency, SVD dimensionality reduction is applied to the feature matrix. The clustering algorithm uses cosine similarity to cluster the feature space and extract keyframes while maintaining relevant information for future retrieval stages. This method extracts keyframes effectively while retaining pertinent information for later stages of the retrieval process.

B. Content-Based Image Retrieval

In the second stage, CBIR involves Feature Extraction (FE) and Search and Match (SaM). Feature extraction plays a critical role in achieving both efficiency and accuracy. The global features are extracted with the help of a pre-trained, compact CNN backbone. Table 2 shows that out of all the state-of-art pre-trained networks, MobileNetV2 [4] has the highest ratio of video duration time and computation time. This represents a significant improvement in performance, expediting video search by twice as faster for a CBIR system with VGG16 or ResNet50. Employing a shallower network (MobileNetV2) as the backbone saves more time, though it may come at the expense of a marginal reduction in accuracy [5].

To address this issue, hybrid feature extraction can be achieved by fusing both global and local features. The fusion

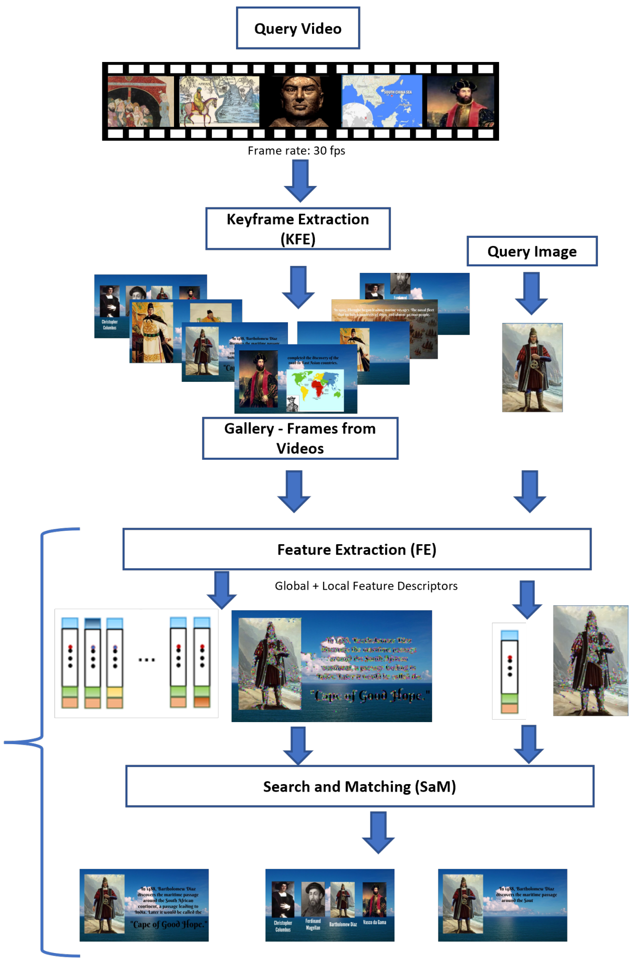

Fig. 1: The pipeline of the Image Retrieval from Video.

structure is a cascade. The first block of the structure consists of feature extraction through local features such as SIFT, SURF, and ORB [6]. Next, the ranking will proceed to eliminate unnecessary gallery frames per query image. The elimination of non-relevant gallery frames is handled by a low threshold value. Afterward, the same process of feature extraction and ranking proceeded on gallery frames after the elimination of non-relevant frames. The second block of the structure is defined as a re-ranking. This stage contains global feature extraction using a compact CNN network. The dataset consists of the extracted frames from the KFE module.

Additionally, approximate nearest-neighbor (ANN) search methods are utilized in the search process to find the top-K closest features to the query feature [7]. The contribution of this paper is to provide image retrieval from a video system with high efficiency and accuracy that could be applied in various types of research to expedite their search process.

III. Experiments and Results

The retrieval accuracy and computational efficiency trade-off is frequently available in retrieval tasks. The specific feature extraction and similarity assessment approaches utilized have a significant impact on the magnitude of this trade-off. High retrieval accuracy necessitates the use of complicated similarity measures and advanced feature extraction algorithms, both of which can be computationally expensive. On the other hand, by using simpler feature extraction techniques and similarity measures, a CBIR system that has been optimized for computational efficiency may have lower retrieval accuracy. As a result, the balance between retrieval accuracy and computational efficiency must be carefully considered while designing and developing CBIR systems, and depending on the needs of the application, appropriate trade-offs may need to be made. In order to validate the system, two main tests are applied: a computation time test for various CNN backbones and classical local feature extraction algorithms and a test to calculate the mean average precision using the Oxford5k dataset [8].

A. Computation Time

Two separate tests are conducted in terms of computation time for algorithms with global features and algorithms with local features. The testing dataset contains historical videos. For local features, SIFT, ORB, SURF, KAZE, AKAZE, and BRISK algorithms are tested. For global features, MobileNetV2, ResNet50, InceptionV3, VGG19, VGG16, EfficientNet, and DenseNet CNN backbones are tested. The metric for this test is the ratio between video duration and computation time. The test results provide the network which is exceptionally efficient in terms of computation time is MobileNetV2 from Figure 2. The achieved average ratio between video duration and computation time is 38.7. For the test on local feature extraction algorithms, ORB outperforms other algorithms with the average ratio between video duration and computation time of 208.8 as shown in Figure 3.

Video Name	MobileNetV2	ResNet50	InceptionV3	VGG19	VGG16	EfficientNet	DenseNet
Battuta_1	48.8	26.5	37.5	15.8	17.9	34.1	24.0
Battuta_2T	49.3	32.0	33.7	29.2	33.2	33.6	22.5
Battuta_3A	65.8	38.2	51.5	23.7	28.7	48.9	32.3
Battuta_4G	45.4	23.4	35.9	15.8	19.0	35.0	21.8
Battuta_5G	45.7	22.8	36.6	14.8	17.7	36.3	22.2
Battuta_6T	32.5	15.4	25.8	9.7	11.8	25.2	15.2
He_1	28.4	17.4	23.7	11.2	13.3	22.8	15.6
He_2Tik	16.8	10.1	13.7	7.1	8.4	10.5	6.9
He_3Tik	21.2	10.7	16.5	7.3	8.8	16.7	9.9
He_4Tik	32.7	20.4	25.6	14.3	17.1	25.5	16.7
Average	38.7	21.7	30.1	14.9	17.6	28.8	18.7

Fig. 2: The ratio of video duration time and computation time for state-of-art pre-trained CNN backbones.

B. Accuracy - mAP

Oxford5k is a set of images (5,062) with 1024x768 resolution comprising 11 different landmark buildings in the Oxford5k database. And there are 55 query images for the ground truth evaluation. This dataset is one of the benchmark open-source databases for retrieval tasks. The ground truth for each query consists of both easy as in Figure 4 and challenging in Figure 5 retrieval tasks to observe the accuracy of the system. The setting of this test consists of a pre-trained

Video Name	Duration (s)	SIFT	SURF	ORB	KAZE	AKAZE	BRISK
Battuta_1	261.0	12.7	8.9	64.7	3.5	20.3	24.5
Battuta_2Tik	52.0	91.1	62.6	460.2	26.5	147.3	183.1
Battuta_3APS	188.0	13.5	8.2	74.8	3.3	19.7	18.7
Battuta_4GEAT	236.0	11.8	7.7	53.6	3.5	20.2	14.2
Battuta_5GTH	446.0	16.3	9.6	71.5	4.2	26.0	25.2
Battuta_6truefig	440.0	12.3	9.0	64.5	3.0	17.8	30.1
He_1	254.0	21.5	15.8	118.5	6.5	36.7	31.1
He_10	560.0	24.9	19.7	128.1	6.0	34.4	60.5
He_11	187.0	37.5	28.7	238.8	9.4	52.0	98.3
He_12	55.0	35.1	32.5	182.1	8.9	49.7	58.8
He_2Tik	59.0	14.8	12.2	76.5	4.7	29.3	45.2
He_3Tik	106.0	26.1	27.8	221.8	8.0	41.7	102.8
He_4Tik	180.0	47.4	36.6	201.1	10.3	74.7	94.4
He_5Tik	59.0	53.9	58.6	366.5	14.6	92.0	173.5
He_6Tik	53.0	88.8	93.5	757.1	22.7	143.6	321.2
He_7GC	105.0	16.4	14.4	137.4	3.6	20.4	107.1
He_8mrgg	215.0	43.0	37.5	154.1	15.5	90.8	53.3
He_9gcme	355.0	23.0	16.7	130.4	6.6	36.3	42.1
Polo_1	323.0	21.1	13.7	97.1	5.8	33.9	24.9
Polo_2Tik	45.0	52.7	41.1	243.2	11.7	82.1	87.0
Polo_3Map	660.0	32.6	31.7	213.5	7.2	42.0	105.0
Polo_4JEB	131.0	95.5	80.1	472.9	24.9	166.7	199.1
Polo_5WGE	1121.0	51.8	40.5	339.0	13.2	76.4	102.3
Polo_6advan	815.0	29.0	17.4	143.9	7.6	45.2	38.0
Average	287.8	36.4	30.2	208.8	9.6	58.3	85.0

Fig. 3: The ratio of video duration time and computation time for classical (local) FE algorithms.

MobileNetV2 network. As a result of the test, mAP is 39.4 and the average accuracy is 0.439. The results show that the mean average precision is not high enough for a reliable retrieval system with only global MobileNetV2 features. To tackle this issue, the cascaded system with local and global descriptors is proposed that can lead to higher accuracy compared to only utilizing global features from a compact network [9].

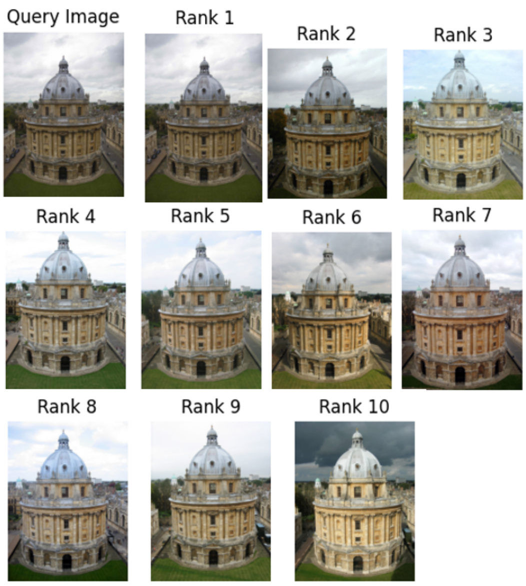

Fig. 4: Easy Task of the Image Retrieval from Oxford5k dataset.

Fig. 5: Challenging Task of the Image Retrieval from Oxford5k dataset.

IV. Conclusion

In this paper, we proposed a method for efficient content-based image retrieval of video resources using a hybrid feature extraction method that combines local descriptors and global features in a cascade structure. We decomposed the task into two stages: keyframe extraction and content-based image retrieval. In the keyframe extraction stage, a clustering algorithm is used to extract keyframes from the input query video, while in the content-based image retrieval stage, a compact deep learning network (MobileNetV2) is used for global feature extraction. For local feature extraction, the ORB algorithm is proposed to be implemented. Our proposed method is a promising step for providing scholars with a powerful tool for accessing and utilizing digital materials efficiently, thereby enhancing the search process.

References

[1] A. Pilevar, "Cbmir: Content-based image retrieval algorithm for medical image databases," *Journal of Medical Signals amp; Sensors*, vol. 1, no. 1, p. 12, 2011.
[2] H. Bay, A. Ess, T. Tuytelaars, and L. Van Gool, "Speeded-up robust features (surf)," *Computer Vision and Image Understanding*, vol. 110, no. 3, p. 346–359, 2008.
[3] T.-W. Chen, Y.-L. Chen, and S.-Y. Chien, "Fast image segmentation based on k-means clustering with histograms in hsv color space," *2008 IEEE 10th Workshop on Multimedia Signal Processing*, 2008.
[4] M. Sandler, A. Howard, M. Zhu, A. Zhmoginov, and L.-C. Chen, "Mobilenetv2: Inverted residuals and linear bottlenecks," *2018 IEEE/CVF Conference on Computer Vision and Pattern Recognition*, 2018.
[5] L. Zheng, Y. Yang, and Q. Tian, "Sift meets cnn: A decade survey of instance retrieval," *IEEE transactions on pattern analysis and machine intelligence*, vol. 40, no. 5, pp. 1224–1244, 2017.
[6] Z. Hu and Y. Jiang, "An improved orb, gravity-orb for target detection on mobile devices," *2016 12th World Congress on Intelligent Control and Automation (WCICA)*, 2016.
[7] Y. H. Yuanyuan Yao and Q. Zhang, "Image-Based Query Search Engine via Deep Learning," Master's thesis, Delft University of Technology, the Netherlands, 2022.
[8] J. Philbin, O. Chum, M. Isard, J. Sivic, and A. Zisserman, "Object retrieval with large vocabularies and fast spatial matching," *2007 IEEE Conference on Computer Vision and Pattern Recognition*, 2007.
[9] Z. Hu and A. G. Bors, "Co-attention enabled content-based image retrieval," *Neural Networks*, 2023.

A Configurable RAN Model to Evaluate and Reduce its Power Consumption and Carbon Footprint

Louis Golard
ICTEAM - UCLouvain
Louvain-la-Neuve, Belgium
louis.golard@uclouvain.be

David Bol
ICTEAM - UCLouvain
Louvain-la-Neuve, Belgium
david.bol@uclouvain.be

Jérôme Louveaux
ICTEAM - UCLouvain
Louvain-la-Neuve, Belgium
jerome.louveaux@uclouvain.be

I. Context and research goal

To contribute to Climate Change mitigation [1], mobile network operators have committed to reduce their carbon footprint, as well as other ICT companies [2]. A large part of it is caused by the electricity consumption of their radio access networks (RANs), in addition to the base station (BS) manufacturing, their maintenance, etc [2]. Moreover, in the last months, electricity prices became very volatile and globally went up, thereby increasing the operating costs of RANs. This is an additional incentive for operators to reduce the electricity consumption of their RANs, while trying to maintain an acceptable quality of service (QoS) for their subscribers.

In [3], we proposed a model to evaluate the RAN power consumption at a country-wide level for six deployment areas and variable traffic loads. We also proposed power models for few types of 4G and 5G BSs with respect to the hourly average data traffic. In this work, we propose a method for evaluating the QoS and the power consumption of the RAN over shorter time intervals. We also consider configurable BSs with various features and component specifications. It applies to all levels of time-frequency loads and to a variable number of users.

II. Model description

The model covers several generic deployment areas, e.g. rural, suburban, urban, etc. Therefore, it does not need to be specific to a given BS layout and we hence consider a regular hexagonal layout of 3-sector BSs with a central BS of interest surrounded by interfering neighboring BSs arranged in several concentric rings. The time discretization of the model is based on transmission time intervals (TTIs) of 1 ms. In this work, only downlink data traffic is included as it is currently the main driver for the deployment of more capacity with new BSs and it induces most of the power consumption.

For evaluating the QoS and the power consumption of a given network configuration (i.e., in a given deployment area, with a particular inter-site distance, carrier frequency, bandwidth, multi-antenna configuration, maximum transmitted power, etc.), we generate random and independent bandwidth loads for each BS cell of the regular network and each TTI within the studied time period. The probability of having one or more active users in a cell depends on the user density in the studied area and the network usage rate per user. This allows to vary the network load from an idle network to a congested one with respect to the time-frequency resources. We then compute the QoS and the power consumption of each realization for each network load and we finally compute average metrics for the BS of interest throughout the studied time period. In a given network configuration, the QoS of a cell depends on the number of active users it serves and the number of neighboring BSs that interfere with it. The BS power consumption depends on the number of its sectors that are active and on their respective bandwidth load. Generally speaking, the BS power model is non-linear (e.g. the BS can enter sleep mode when none of its sectors is active).

To speed up computations, we reduce the total number of possible network states by considering only two states for each BS cell: (i) the idle state when no user is active and no data is transmitted, the load is then 0% and only signaling is transmitted (if applicable), and (ii) the fully active state when one or more users are active in the cell and 100% of the bandwidth is occupied by data and signaling. Since there are two possible states for each cell, there are 2^{3n} possible state combinations for a network containing n BSs (and $3n$ cells). Therefore, we evaluate only specific network state combinations out of the entire set of possible combinations and interpolate the network QoS for the intermediate combinations. This technique produces consistent results.

III. Future work

The next step is to validate the proposed theoretical model with on-site BS measurements and to fine-tune the model parameters with realistic values. We will also include the carbon footprint evaluation by considering the production of the BSs in addition to the emissions due to their electricity consumption during the use phase. In the end, our model will serve to optimize future RAN deployments in order to reduce their total power consumption and carbon footprint.

References

[1] IPCC, "Summary for policymakers. In: Climate Change 2022, Mitigation of Climate Change, AR6, WGIII," *Cambridge University Press*, 2022.
[2] ITU-T, "GHG emissions trajectories for the ICT sector compatible with the UNFCCC Paris Agreement," *L.1470 Recommendation*, 2020.
[3] L. Golard, J. Louveaux, and D. Bol, "Evaluation and projection of 4G and 5G RAN energy footprints: The case of Belgium for 2020–2025," *Annals of Telecommunications*, 2022.

This work is funded by Proximus NV/SA.

Drive-Line Extraction from Aerial Images

Julien A. Vijverberg*, Bart J. Beers*, Egor Bondarev†, Peter H. N. de With†
*Cyclomedia Technology B.V., The Netherlands {*jvijverberg, bbeers*}@*cyclomedia.com*
†Eindhoven University of Technology, The Netherlands {*e.bondarev,p.h.n.de.with*}@*tue.com*

I. Introduction

Intersection-topology descriptions can help to improve traffic flow, safety and CO_2 emissions, in addition to being a valuable tool for autonomous vehicle navigation. However, they currently require significant manual effort for creating useful descriptions. This paper describes ongoing work on automated algorithms to extract the vehicle drive-lines in the entry and exit lanes of intersections, using the annually captured Cyclomedia imagery and point clouds.

Our previous work [1] derived the drive lines from the paint striping and road edges, but this resulted into several rule-based post-processing steps and did not account for merging and splitting lanes. This paper presents experiments on direct extraction of drive lines from aerial images. We outline the processing pipeline and compare with alternative algorithms for drive-line extraction.

II. Method

The system comprises three steps: (1) segmentation, (2) line extraction, (3) line clustering.

a) Segmentation: For line segmentation, a U-Net is used to generate a binary mask with the drive lines as foreground and the rest as background information. In the training data, we mark the conflict area of each intersection and many secondary roads as "to-be-ignored".

b) Line Extraction: For line extraction, we experiment with and compare three alternative methods. The first one is the well-known probabilistic Hough transform. The second method, LCNN [2], is designed as an end-to-end network to predict lines of wire frames. However, LCNN training on aerial color images did not yield useful results. Hence, following the work by Liu *et al.* [3], we instead use the binary segmentation mask as input. The third method for comparison is NEFI [4], which was designed to extract graphs from images like road networks. All three methods result in drive-line proposals.

c) Line Clustering: Line clustering further merges the line proposals using a hierarchical approach, as previously presented for clustering paint striping and edge-of-road [1].

III. Experimental Results

The dataset consists of 67 urban and 70 rural highway scenes in the Netherlands. From this set, 29 urban and 18 highway scenes are used for testing. Each image has 2048×2048 pixels and a resolution of approximately 10 cm per pixel. To evaluate the results, the segmentation mask is generated from the line clustering results and compared with the ground-truth segmentation mask. Table I illustrates the results for line extraction. Evidently, recall scores are lower than in generic object-segmentation problems, since drive lines and their boundaries are not strictly defined.

Fig. 1: Example results of the pipeline with LCNN.

	Highway		Intersections	
	Recall	Precision	Recall	Precision
Hough	0.48	0.56	0.11	0.52
NEFI	0.48	0.38	0.24	0.23
LCNN	0.61	0.44	0.31	0.34

TABLE I: Recall and precision for the final, rendered masks.

IV. Discussion and Conclusions

This paper confirms that ill-defined drive lines can be learned by a segmentation network. Hough line extraction is not suited for extracting drive lines for intersections on these image scales, but this might be improved by running at a smaller scale. Finally, the results show that LCNN is a promising algorithm for drive-line extraction, increasing the recall from 0.11 and 0.24 to 0.31. We expect to move forward towards end-to-end training and if insufficient, resort to graph-based modeling using traffic-junction classification.

References

[1] J. A. Vijverberg, B. J. Beers, and P. H. N. de With, "Towards automatic inference of layouts of traffic intersections for smart cities," in *GEOProcessing*, 2022.

[2] Y. Zhou, H. Qi, and Y. Ma, "End-to-end wireframe parsing," in *ICCV 2019*, 2019.

[3] X. Liu, E. Bondarev, and P. H. N. de With, "DL-based floorplan generation from noisy point clouds," in *Electronic Imaging - 3D Imaging and Applications*, 2023.

[4] M. Dirnberger, T. Kehl, and A. Neumann, "NEFI: Network extraction from images," *Sc. Reports*, vol. 5, 2015.

Range and Phase Offset Estimation of Multiple Transponder-equipped Aviation Vehicles

Mostafa Mohammadkarimi, *Member, IEEE*, Geert Leus, *Fellow, IEEE*, and Raj Thilak Rajan, *Senior, Member, IEEE*

***Abstract*—A new method for joint range and phase offset estimation of multiple transponder-equipped aviation vehicles, including manned aerial vehicles (MAVs) and unmanned aerial vehicles (UAVs) is proposed in this paper. The proposed method employs the overlapping secondary surveillance radar signals for ranging and phase offset estimation prior to decoding of the overlapping signals; hence, it can ameliorate aviation air safety when packet decoding is infeasible due to packet collision. The overlapping signals can be Mode A, C, S, and ADS-B. Moreover, the proposed estimator enables coherent detection of a single or collided multiple secondary surveillance radar signals with a lower packet error rate (PER) compared to non-coherent detection. This results in significant performance improvement in active multiple target tracking and cooperative sense and avoid systems.**

To derive the joint estimator, first, by minimizing the Kullback–Leibler Divergence (KLD) as a measure of difference between probability densities, we analytically show that the complex received baseband of the overlapping secondary surveillance radar signals coming from aviation vehicles can be approximated by an independent and identically distributed (i.i.d.) Gaussian Mixture (GM) random variable. Then, we employ the Expectation–Maximization (EM) algorithm to estimate the modes of the Gaussian mixture followed by a reordering estimation technique through combinatorial optimization to estimate range and phase offset of the aviation vehicles.

The effectiveness of the proposed estimator is supported by simulation results for different number of aviation vehicles for Mode A, C, S, and ADS-B overlapping signals. We show that the proposed estimator can accurately estimate the range of multiple transponder-equipped aviation vehicles in the presence of different overlapping secondary surveillance radar signals. Moreover, our proposed joint estimator outperforms the state of the art methods [2] and [3] since our approach employs the whole observation samples including the overlapping snapshot; however, the methods in [2] and [3] rely on the non-overlapping snapshot for packet recovery. Hence, as the delay between the reception of two packets decreases, their performance degrades.

***Index Terms*—Ranging, phase offset, Mode S expectation–maximization (EM), Gaussian mixture (GM), multiple antenna, sense and avoid (SAA).**

The authors are with the Faculty of Electrical Engineering, Mathematics and Computer Science, Delft University of Technology, 2628 CD Delft, The Netherlands (e-mail: m.mohammadkarimi@tudelft.nl, G.J.T.Leus@tudelft.nl, R.T.Rajan@tudelft.nl).

This work is partially funded by the European Leadership Joint Undertaking (ECSEL JU), under grant agreement No 876019, and the ADACORSA project - "Airborne Data Collection on Resilient System Architectures." (https://adacorsa.eu/).

The joint ranging and phase offset estimation for only ADS-B signals was investigated in [1] and it is under submission. This paper extends the previous work to the general case of secondary surveillance radar signals, such as Mode A, C, and S.

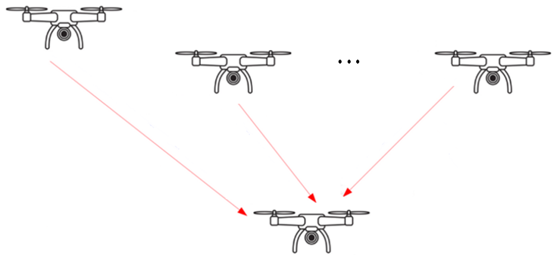

Fig. 1: Packet collision of secondary surveillance radar signals.

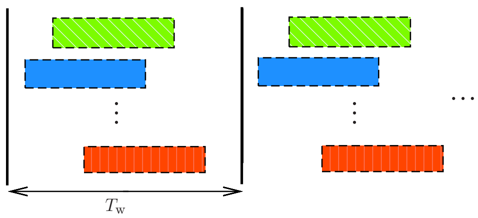

Fig. 2: The reception of the Mode A, C, B, and ADS-B signals of the aviation vehicles at the receiver. Different colors are used to show the Mode A, C, B, and ADS-B signals of the aviation vehicles. The range and phase offset are estimated from the overlapping packets.

References

[1] M. Mohammadkarimi, G. Leus, and R. T. Rajan, "Joint ranging and phase offset estimation for multiple drones using ADS-B signatures," *arXiv preprint arXiv:2207.05370*, 2022.

[2] K. Li, J. Kang, H. Ren, and Q. Wu, "A reliable separation algorithm of ADS-B signal based on time domain," *IEEE Access*, vol. 9, pp. 88 019–88 026, 2021.

[3] W. Wang, R. Wu, and J. Liang, "ADS-B signal separation based on blind adaptive beamforming," *IEEE Trans. Veh. Technol.*, vol. 68, no. 7, pp. 6547–6556, 2019.

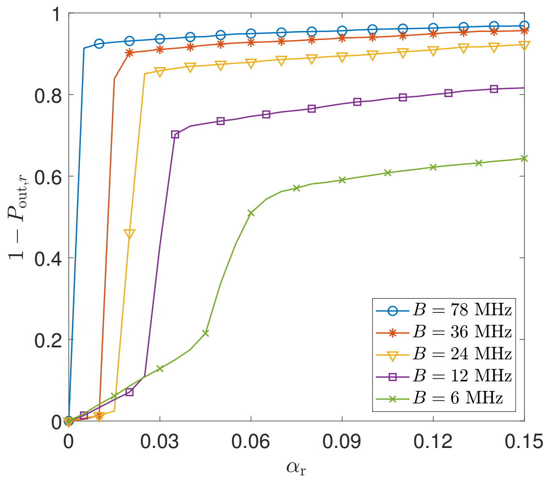

(a) Range estimation for $K = 3$ aviation vehicles

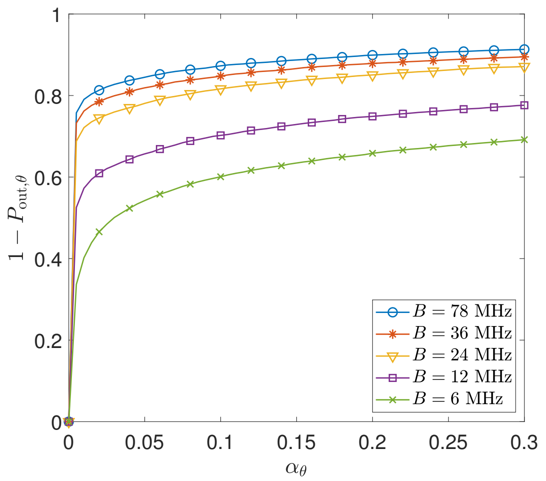

(b) Phase Offset (PO) estimation for $K = 3$ aviation vehicles

Fig. 3: The performance of the proposed joint EM-based estimator for three aviation vehicles with transmit power $P_1 = P_2 = P_3 = 51$ dBm, and range $r_1, r_2, r_3 \in \mathcal{U}_{\mathrm{c}}[1, 10]$ Km. The number of receive antennas is $N_{\mathrm{r}} = 5$, and α_r and α_r denote the percentage error for range and phase, respectively. We also define $P_{\mathrm{out},r} \triangleq \frac{1}{K}\sum_{k=1}^{K} \mathbb{P}\big\{\frac{|\hat{r}_k - r_k|}{r_k} > \alpha_r\big\}$ and $P_{\mathrm{out},\theta} \triangleq \frac{1}{KN_{\mathrm{r}}}\sum_{\ell=1}^{N_{\mathrm{r}}}\sum_{k=1}^{K} \mathbb{P}\big\{\frac{|\hat{\theta}_{\ell,k} - \theta_{\ell,k}|}{\theta_{\ell,k}} > \alpha_\theta\big\}$ for $K = 3$. The receiver filter bandwidth is denoted by B.

Papers not appearing in the proceedings

The following papers wished not to appear in the proceedings (usually for copyright reasons):

New EM-Based Radar Propagation Model
François De Saint Moulin, Christophe Craeye, Luc Vandendorpe, Claude Oestges (Université catholique de Louvain)

Enhancing Signal Classification on Embedded Devices with Spectrum Painting
Bingyang Li (University of Chinese Academy of Sciences), Qing Wang (Delft University of Technology)

Performance Comparison of the Fractional Fourier Transform and Matched Filtering for Delay-Doppler Estimation with a Wideband LFM Preamble
Ids Van der Werf, Richard C. Hendriks (Delft University of Technology), Richard Heusdens (Delft University of Technology and Netherlands Defence Academy)

Acoustic transfer function estimation exploiting spectral correlations
Giovanni Bologni, Richard Heusdens, Richard C. Hendriks (Delft University of Technology)

Sensor Selection using the Two-Target Cramer-Rao Bound for Angle of Arrival Estimation
Costas A. Kokke (Delft University of Technology), Mario Coutiño, Laura Anitori (Netherlands Organisation for Applied Scientific Research), Richard Heusdens (Netherlands Defence Academy), Geert Leus (Delft University of Technology)